

# **Dose Response of Selected Radiation Detectors in a Magnetic Field**

by

Michael Watson Reynolds

A thesis submitted in partial fulfillment of the requirements for the degree  
of

Doctor of Philosophy

in

Medical Physics

Department of Oncology

University of Alberta

© Michael Watson Reynolds, 2015

# Abstract

With the advent and development of hybrid Linac-MR technology, we will be able to track and treat lesions in real time. This will permit the narrowing of radiotherapy margins and escalation of dose, augmenting the therapeutic outcome of radiotherapy. The addition of a magnetic field to the treatment volume introduces difficulties in the measurement of the output radiation of the accelerator. This work investigates the dose response of various ionisation chambers and solid state detectors within a magnetic field in various relative orientations of photon beam, magnetic field, and detector axis. The orientations of interest can be divided as per the directions of the magnetic field and detector axis, with the radiation direction static; the magnetic field direction is set either transverse or longitudinal to the incident radiation, and the detector axis can independently be parallel or perpendicular to the incident radiation. The well benchmarked Monte Carlo code PENELOPE is used to model the dose deposition in the active volumes of the various detectors in air and in a water tank as a function of magnetic field strength in the orientations of interest. When physically possible, the dose response of the detectors in the relevant orientations is measured experimentally with the aid of small transverse and longitudinal electromagnets. The dose response of the detectors is defined as the ratio of dose deposited with magnetic field, to that without magnetic field. Dose

response of all detectors as a function of magnetic field strength was found to have a strong dependence on the relative orientations of incident 6 MV radiation, magnetic field, and detector axis. Specifically, a chamber specific correction factor is required when detectors are used within a transverse magnetic field; this correction factor will also be orientation specific. Longitudinal field orientations, in contrast, seem to require no correction up to near 1.0T, thereafter a small orientation independent correction is needed. Water tank simulations show that radiation penumbras cannot in general be measured accurately in transverse fields; however, longitudinal magnetic fields do not cause issues in penumbra measurement. For the purposes of dose determination, longitudinal magnetic fields are preferred.

# Preface

This thesis is original work by Michael Reynolds. The part of this thesis detailing the Monte Carlo simulation and transverse magnetic field measurement of PR06C and NE2571 ionisation chamber response has been previously published as M. Reynolds, B. Fallone, and S. Rathee, "Dose response of selected ion chambers in applied homogeneous transverse and longitudinal magnetic fields," *Med. Phys.* **40**(4), 042102 (2013). Additionally, PTW60003 and IBA PFD detector response simulations and transverse magnetic field measurements have been previously published as M. Reynolds, B.G. Fallone, and S. Rathee, "Dose response of selected solid state detectors in applied homogeneous transverse and longitudinal magnetic fields," *Med. Phys.* **41**(9), 092103 (2014). Regarding both publications, I was responsible for data collection and analysis, as well as the composition of the manuscript. B. Fallone and S. Rathee were supervisory authors and were involved in the formulation of the research concept and manuscript review.

# Acknowledgements

This thesis represents a significant amount of work which demanded abundant time and attention, sometimes detracting from other facets of life. I would henceforth like to acknowledge and thank those persons and institutions who made this work possible; these persons and institutions are varied and plentiful, with each offering support in their own way. These support contributions are cumulative in effect, and it would therefore be erroneous to elevate any one above the rest.

Firstly, I will acknowledge the support of my supervisor Dr. Satyapal Rathee, and co-supervisor Dr. Gino Fallone. Throughout my scholarly endeavours I have received guidance and recommendations when needed, and been left to work independently towards an ultimate goal when my work was progressing unhindered. Drs. Rathee and Fallone have also endured countless presentations and seminars on my work, critiquing the format and delivery of the results towards perfection. Furthermore, I owe thanks to Dr. Rathee for his innumerable edits and revisions of multiple manuscripts submitted for publication, as well as the initial edits and revisions for this thesis itself; looking back at old works it is clear that the lexicon and style of writing I employ has improved much over the years, resultant directly from these revisions. Dr. Marc Mackenzie, while part of my committee you consistently managed to find the limits of my knowledge, and challenged me to expand them. I have learned much as a direct result of research into topics you've inquired about.

To the graduate students currently working towards a degree, and to those who have completed their work, it's been a pleasure working with you. It was exceedingly advantageous to be surrounded by so many intelligent people; I've undoubtedly saved myself a considerable amount of time by simply heeding the advice offered to me. Ben and Danielle, you both made

short work of helping me get started with PENELOPE, whose user manual is as robust as it is daunting. I wish you both luck in your future endeavours. Devin and Dave, thank you for enduring classes, and more importantly, the dreaded labs alongside me. Your work ethic, practicality, and intelligence helped us all progress through the lab work without any major problems. Amr, your run times keep improving; next time we meet it is likely that you will outpace me, congratulations. It was always easier to get focused on the task at hand after a lunchtime run, thank you for keeping me company. Andrei, if it weren't for your experience and expertise with the GMW magnet, my experiments would have been many times more tedious and time consuming. Furthermore, your inquiries into the workings of Monte Carlo radiation transport for your own research have allowed me to better understand it for my purposes. I would also like to acknowledge the ubiquitous stimulating conversations with friends from each of the labs: Eugene, Brennan, Jean-David, Dan Michael, and all the rest. These brief digressions provided a relaxed atmosphere conducive to both good spirits and productivity.

There are undoubtedly those outside of the Cross Cancer Institute deserving of many thanks. I would first like to thank Crystal, whose unremitting encouragement and support came in many forms, both tangible and intangible. I've been exceedingly lucky to have you by my side over these years, and foresee nothing different in all the years to come. The exact instruments and methods of your support of far too numerous to list; without being overly verbose, it suffices to say I greatly appreciate all you have done, and look forward to returning the favour.

There are also many friends worthy of praise for their guidance and efforts towards the elimination of stress. To name a few: Scott and Andrea Stockdale, Brennan and Amy Scherdtel, Scott Knowles and Allison Husband. Thank you for all the games nights, sports and exercise days, and general good times over the years, they were a necessitated distraction and

will be fondly remembered for some time to come. I would also like to give special thanks to Amy Scherdtel for her help with the writing of this dissertation; when writing for so long that words no longer looked to form coherent thoughts, she was invaluable in helping sort through the chaos.

We now arrive at those constant in life, family. I have received overwhelming support from those closest to me, and would like to thank them for all they have done over these past number of years. Donna Watson, whose financial and personal support has made it immeasurably easier to progress throughout both undergraduate and graduate work. I would also like to acknowledge the substantial support from my parents Les Reynolds and Kelli Reynolds; who would always encouraging my progression, and were interested in the work I was doing. My brother, Mathew Reynolds, thank you for the support; now you can read all about Monte Carlo and see exactly why it works. To everyone else further out on the family tree – and those honorary family – your support is also greatly appreciated. The myriad of you all provided unwavering support and encouragement; it is no small feat to progress through higher education and attain a doctoral degree, and you helped make that possible.

Finally, I would like to extend my thanks to the Bushido Karate Association (BKA). I embarked upon my karate journey before graduate school, and it has ever since been an unceasing source of encouragement, as well as an instrument through which to vent frustrations and clear my thoughts. The erosion of the accumulated mental exhaustion experienced whilst training is astounding, and played no small part in helping maintain focus leading towards the successful completion of my Ph.D. Specifically within the BKA, James Freeman, Craig Pettie, Scott Knowles, and Elliott Knowles have been instrumental in my training, culminating in the receipt of my Shodan ranking. Moreover, it would be remiss to fail to mention all those whom with I train, it simply wouldn't be the same without your presence on the dojo floor; you motivate me to perform better and strive for constant

improvement. I look forward in anticipation of many more years of rewarding training and teaching.

In closing, this project has been long and arduous, and the support unending. Thank you to all those who helped see me through, if not for you I imagine a much different outcome would have prevailed.

# Table of Contents

Chapter 1: Introduction .....	1
1.1 What is Cancer? .....	1
1.2 Cancer Today .....	2
1.3 Radiation Therapy Today .....	4
1.4 Linac-MR .....	11
1.5 Motivation and Framework .....	15
1.6 References .....	19
Chapter 2: Theory .....	25
2.1 Electromagnetic Fields .....	25
2.2 Lorentz Force .....	30
2.3 Hall Effect .....	31
2.4 Radiation in Matter .....	33
2.4.1 Photoelectric Effect .....	34
2.4.2 Compton Effect .....	36
2.4.3 Pair Production .....	38
2.4.4 Kerma and Dose .....	40
2.5 Statistics and Random Sampling .....	44
2.6 Monte Carlo Techniques for Radiation Transport .....	49
2.7 Adding Electromagnetism to Monte Carlo .....	56
2.8 Ionisation Chambers .....	58
2.9 TG-51 .....	61
2.10 Solid State Detectors .....	62
2.11 References .....	65
Chapter 3: Implementation .....	68
3.1 Orientations of the Photon Beam, B Field, and Detector .....	68

3.2	Modelling Detectors in PENELOPE .....	70
3.2.1	PENELOPE Code .....	71
3.2.2	Simulation Setup .....	73
3.2.3	Detector Geometries .....	74
3.2.4	Beam Scanning Simulations .....	80
3.3	Measurement Setup .....	84
3.3.1	Transverse Magnetic Field Measurements .....	85
3.3.2	Longitudinal Magnetic Field Measurements .....	89
3.3.3	OSL Measurements .....	90
3.4	References .....	93
Chapter 4: Results and Discussion .....		95
4.1	Ionisation Chambers .....	95
4.1.1	$k_Q$ , Field Size, $P_{ion}$ , and $P_{pol}$ Measurements .....	95
4.1.2	NE2571 .....	97
4.1.3	PR06C .....	101
4.1.4	A12 .....	104
4.2	Solid State Detectors .....	105
4.2.1	PTW60003 Diamond Detector .....	105
4.2.2	IBA PFD Diode Detector .....	111
4.3	Beam Scanning Simulations .....	118
4.3.1	Solid State Detectors .....	118
4.3.2	CC13 Detector .....	123
4.4	OSL Measurements .....	125
4.5	References .....	127
Chapter 5: Conclusion .....		129
5.1	Overview .....	129
5.2	Ionisation Chambers .....	130
5.3	Solid State Detectors .....	131

5.4	Water Tank Simulations .....	132
5.5	OSL Detectors .....	134
5.6	Future Work.....	134
5.7	References .....	136
	Bibliography.....	137

# List of Tables

Table 3.1 Geometrical setup and PENELOPE simulation parameters or each detector investigated.....	74
Table 4.1 Chamber $k_Q$ values without the magnetic field are compared with the previously published results. Errors quoted are 1 standard deviation.	97
Table 4.2 Ratio of readings with the magnetic field indicated to no magnetic field as a function of field size. All measured values are $\pm 0.02\%$ .....	97
Table 4.3 $P_{pol}$ and $P_{ion}$ values as a function of magnetic field. Calculation formalism used as per column reference. All values are $\pm 0.02\%$ .....	97

# List of Figures

Figure 1.1 Illustration of the ICRU volumes defined in the treatment planning process. The gross tumour volume (GTV), clinical target volume (CTV), planning target volume (PTV), and organ at risk (OAR) are shown. It should be noted that the PTV is composed of the internal margin (IM) and setup margin (SM) together..... 6

Figure 1.2 Transverse configuration of the rotating bi-planar (RBP) Linac-MR system developed at the CCI. The Linear accelerator is positioned laterally at the open side of the bi-planar magnet assembly. Pole plates are shown in blue, and radiation beam in yellow. .... 13

Figure 1.3 Longitudinal configuration of the rotating bi-planar (RBP) Linac-MR system developed at the CCI. The linear accelerator is positioned above a pole plate, and will irradiate through a hole in the pole plate. Pole plates are shown in blue, and radiation beam in yellow. .... 14

Figure 2.1 Schematic of the Hall Effect. The direction of current flow  $I$  is shown in blue, the magnetic field  $B$  is shown in red, electric and magnetic forces on electrons are shown in light green and orange respectively, and the charge buildup is represented by the dark green dashed lines. The voltmeter used to measure the electric potential is placed as shown by the “V” in the schematic. .... 31

Figure 2.2 Domains of interaction dominance for photoelectric ( $\tau$ ), Compton ( $\sigma$ ), and pair production ( $\kappa$ ) as a function of photon energy and atomic number ( $Z$ ) of the medium. .... 33

Figure 2.3 Illustration of the photoelectric effect. A photon of energy  $h\nu$  (shown in green) is incident on an iron atom (blue), transferring its energy

to an electron (red) causing the atom to ionize. The photoelectron (orange) escapes with kinetic energy  $T_e=h\nu-E_b$ ..... 34

Figure 2.4 Photoelectric cross section of iron as a function of incident photon energy in electron volts (eV). Sharp discontinuous jumps are seen when photons have enough energy to ionize additional shells of the atom. Cross section data extracted from the PENELOPE code system<sup>9</sup>..... 35

Figure 2.5 Illustration of the Compton effect. A photon with incident energy  $h\nu$  scatters off of a free electron. The photon scatters at angle  $\phi$  with energy  $h\nu'$ , and the electron scatters at angle  $\theta$  with energy  $h\nu-h\nu'$ ..... 36

Figure 2.6 Compton cross section of iron as a function of incident photon energy in electron volts (eV). Cross section data extracted from the PENELOPE code system<sup>9</sup>..... 38

Figure 2.7 Illustration of pair production. A photon in the presence of the Coulomb field of an atom splits into a positron-electron pair. .... 39

Figure 2.8 Pair production cross section of iron as a function of incident photon energy in electron volts (eV). Cross section data extracted from the PENELOPE code system<sup>9</sup>..... 40

Figure 2.9 Total, photoelectric, Compton, and pair production cross sections of iron as a function of incident photon energy in electron volts (eV). Cross section data extracted from the PENELOPE code system<sup>9</sup>..... 41

Figure 2.10 Illustration of charged particle equilibrium (CPE). Incident photons (green) interact with the medium (blue) and transfer kinetic energy to electrons (red). CPE does not exist at point A since fewer electrons enter that region than leave. CPE exists at point B because the electrons entering and leaving the region are equal. .... 42

Figure 2.11 Total, radiative, and collisional stopping power of electrons in iron. Data extracted from the PENELOPE code system <sup>9</sup> .....	44
Figure 2.12 Inverse transform sampling of $x$ , using a random number $R$ and the cumulative distribution (green) of a probability density function (red) of $x$ .....	48
Figure 2.13 50 cm trajectory of a 10 MeV electron in a Z directed 1.25T magnetic field as simulated by the PENELOPE code system in vacuum <sup>9</sup> . All axes values are displayed in cm. Initial electron direction was along the $y$ axis. ....	55
Figure 2.14 Electrons are excited from the valence band (blue) to the conduction band (white), where they are collected by an electric field. ...	63
Figure 2.15 Electrons are excited from the valence band (blue) to the conduction band (white), before falling into the traps between the bands. These electrons can be excited at a later time, creating photons when they transition from the conduction band back to the valence band. ....	64
Figure 3.1 Various geometrical orientations for radiation detector's long axis (central cylinder) magnetic field (arrow) and radiation beam (transparent rectangular prism) as used in Monte Carlo simulation and experimental measurements.....	70
Figure 3.2 Schematic of the NE2571 ionisation chamber. Purple is the air cavity itself, green the Al electrode, blue the graphite wall, and orange the water buildup. ....	75
Figure 3.3 Schematic of the PR06C ionisation chamber. The central orange region is the air cavity, the purple wall, electrode, and stem are the C-552 conducting plastic, blue is the PMMA buildup cap, and black is vacuum. ....	76

Figure 3.4 Schematic of the A12 ionisation chamber. The central purple region is the air cavity, the orange wall, electrode, and stem are C-552 conducting plastic, and the blue is water. .... 77

Figure 3.5 PTW 60003 diamond detector (A and C) and IBA PFD diode detector (B and D) simulated geometries without changes (A and B) and with changes to materials (C and D). Material legend is in the top left, background material is not shown, and is PMMA in all cases. .... 80

Figure 3.6 Illustration of the water tank simulation positions at 10 cm depth for the CC13 chamber. Orange represents the water tank, yellow the 10cm x 10 cm periphery of the radiation field at 10 cm depth, and blue are the simulation points. .... 82

Figure 3.7 Schematic of the CC13 ionisation chamber. The central orange region is the air cavity, the purple electrode and wall are C-552 conducting plastic, blue is the PEEK stem, and green is water. .... 83

Figure 4.1 (above) NE2571 relative dose deposited as a function of magnetic field in orientations I, II as determined in Monte Carlo simulations, and orientations I and II as determined in the measurements previously published by Meijnsing *et al* (2009)<sup>1</sup>. .... 98

Figure 4.2 NE2571 relative dose deposited as a function of magnetic field in orientations III, IV as determined in Monte Carlo simulations, please note the simulation data points nearly lie on top of each other. .... 99

Figure 4.3 PR06C simulated relative dose deposited as a function of magnetic field in orientations I-IV. .... 102

Figure 4.4 Measured and simulated relative dose response of the PR06C ion chamber as a function of transverse magnetic field strength ..... 102

Figure 4.5 Measured and simulated relative dose response of the PR06C ion chamber as a function of longitudinal magnetic field strength. .... 103

Figure 4.6 A12 simulations of relative dose deposited as a function of magnetic field in orientations I-IV.....	105
Figure 4.7 Monte Carlo generated dose response of the PTW60003 diamond detector as a function of magnetic field strength, error bars are $\pm 1$ standard deviation .....	106
Figure 4.8 Monte Carlo generated dose response of the PTW60003 diamond detector as a function of magnetic field strength, error bars are $\pm 1$ standard deviation .....	106
Figure 4.9 Monte Carlo generated dose response of the PTW60003 diamond detector compared to measurements as a function of magnetic field strength, error bars are $\pm 1$ standard deviation .....	107
Figure 4.10 Comparison of the PTW 60003 diamond detector original build (figure 3.5A) to the modified build (figure 3.5C, labelled "modified"), average standard deviation of simulation points for the "modified" build is 0.70%.....	107
Figure 4.11 Measured and simulated relative dose response of the PTW60003 diamond detector as a function of longitudinal magnetic field strength.....	111
Figure 4.12 Monte Carlo generated dose response of the IBA PFD diode detector as a function of magnetic field strength, error bars are $\pm 1$ standard deviation .....	112
Figure 4.13 Monte Carlo generated dose response of the IBA PFD diode detector as a function of magnetic field strength, error bars are $\pm 1$ standard deviation .....	112
Figure 4.14 Monte Carlo generated dose response of the IBA PFD diode detector compared to measurements as a function of magnetic field strength, error bars are $\pm 1$ standard deviation.....	113

Figure 4.15 Comparison of the IBA PFD diode detector original build (figure 3.5B) to the modified build (figure 3.5D, labelled "modified"), average standard deviation of simulation points for the "modified" build is 0.98% 113

Figure 4.16 Measured and simulated relative dose response of the IBA PFD diode detector as a function of longitudinal magnetic field strength..... 117

Figure 4.17 PTW60003 diamond detector simulations in air and a water tank, presented as the ratio of dose with to dose without magnetic field (0.5T). Water tank simulations are done in dose at depth (labeled DD, corresponding to orientations I and III depending on magnetic field direction) and profile scanning (labeled Profile, corresponding to orientation II-2 and IV depending on magnetic field direction) geometries, at Dmax, 5cm depth on the CAX, and 5cm depth at beam left (LE) and right (RE) edges (beams eye view). Ratio of dose to water, i.e. in the absence of detector, at all these points in the phantom are also presented..... 118

Figure 4.18 IBA PFD diode detector simulations in air and a water tank, presented as the ratio of dose with to dose without magnetic field (0.5T). Water tank simulations are done in dose at depth (labeled DD, corresponding to orientations I and III depending on magnetic field direction) and profile scanning (labeled Profile, corresponding to orientation II-2 and IV depending on magnetic field direction) geometries, at Dmax, 5cm depth on the CAX, and 5cm depth at beam left (LE) and right (RE) edges (beams eye view). Ratio of dose to water, i.e. in the absence of detector, at all these points in the phantom are also presented..... 119

Figure 4.19 CC13 simulations in a water tank presented as the ratio of dose with to dose without magnetic field (0.5T). Water tank simulations are done at various depths in the phantom, and at the beam peripheries at 10cm depth. The ratio of dose to water, i.e. in the absence of the detector, at the periphery in the direction of electron travel also presented..... 124

Figure 4.20 Relative dose response of Nanodot OSLs in transverse (without and with backscatter bolus) and longitudinal magnetic fields as a function of magnetic field strength..... 126

# List of Acronyms

ABS	Acrylonitrile Butadiene Styrene
ART	Adaptive Radiation Treatment
ART <sup>2</sup>	Advanced Real Time Adaptive Radiotherapy
CAX	Central AXis
CPE	Charged Particle Equilibrium
CTV	Clinical Target Volume
CT	Computed Tomography
CBCT	Cone Beam Computed Tomography
CSDA	Continuously Slowing Down Approximation
CCI	Cross Cancer Institute
DCS	Differential Cross Section
DRR	Digitally Reconstructed Radiograph
DNA	DeoxyriboNucleic Acid
DD	Dose at Depth
EM	ElectroMagnetic / ElectroMagnetism
ERE	Electron Return Effect
eV	Electron Volts
EPID	Electronic Portal Imaging Device
XBRT	External Beam RadioTherapy
GTV	Gross Tumour Volume
IGRT	Image Guided RadioTherapy
IMRT	Intensity Modulated Radiation Therapy
IM	Internal Margin
ICRU	International Commission on Radiation Units and Measurements
kV	KiloVoltage
LE	Left Edge

MRI	Magnetic Resonance Imaging
MV	MegaVoltage
MU	Monitor Unit
MLC	Multi Leaf Collimator
NTCP	Normal Tissue Complication Probability
NEA	Nuclear Energy Agency
OBI	Onboard Imaging System
OSL	Optically Stimulated Luminescence
OAR	Organ At Risk
OECD	Organisation for Economic Co-operation and Development
PENELOPE	PENetration and Energy Loss Of Positrons and Electrons
PTV	Planning Target Volume
PMMA	Poly(Methyl MethAcrylate)
PEEK	PolyEther Ether Ketone
PDF	Probability Density Function
RE	Right Edge
RBP	Rotating Bi Planar
SM	Setup Margin
SAD	Source to Axis Distance
SSD	Source to Surface Distance
TCP	Tumour Control Probability

# Chapter 1: Introduction

## 1.1 What is Cancer?

Cancer is a broad term for a plethora of diseases characterized by the uncontrolled proliferation of cells in the body. These cells multiply and create tumours that may metastasize, creating secondary sites of cancer. These malignancies eventually hinder organ function, and can cause a multitude of symptoms including fatigue, fever, pain, weight loss, and eventually death<sup>1, 2</sup>. The exact symptoms and cause of death will vary depending on the type and location of the cancer. There are two main mechanisms, or defects, by which cell division may become unregulated and a tumour may develop; there can be either an over-expression of cell division pathways, or an under-expression of cell repair and regulation (known as tumour suppression) pathways<sup>2-4</sup>. Either of these types of defects in a cell may trigger excessive cell division. A cell with one defect may cause a small benign tumour to form; over time, if more defects accrue, the tumour may grow into a malignancy, commonly known as cancer.

These defects are generally associated with genes, which are segments of DNA which code for proteins to be used for any number of life functions in a cell<sup>3, 4</sup>. Genes whose presence are responsible for the development of cancer are known as oncogenes, and their normal precursors are known as proto-oncogenes. The proto-oncogenes may be transformed into oncogenes via a number of different methods. Point mutations in one or more of the base pairs constituting the code for a particular protein, or DNA rearrangement where the proto-oncogene has base pairs either exchanged or rearranged with the genes surrounding it in the DNA strand, are two of the major mechanisms which may cause the transformations. The oncogene can cause an overexpression in cell division by creating a

hyperactive version of a protein responsible for cell growth. This hyperactive protein causes cell growth without the presence of growth factor signals, as a result the body loses the ability to regulate growth in these cells. Alternatively, many copies of the proto-oncogene may be present, causing an otherwise normal protein to be overexpressed, leading to unwanted excessive cell division. This process of increasing the number of copies of a specific gene is known as gene amplification. It is also possible for tumour suppression pathways to become damaged due to the presence of an oncogene. One such example is the p53 gene and its associated protein, whose mutation is present in near 50% of all cancers<sup>3, 4</sup>. The undamaged p53 protein activates when DNA damage is detected. The active protein halts cell division to facilitate DNA repair, and in the event that DNA repair is not possible, the protein will initiate a form of cell death known as apoptosis to prevent the proliferation of DNA errors. The damaged p53 protein is entirely non-functional, and leaves the cell restricted in its DNA repair mechanisms. Therefore, the p53 gene is responsible for the suppression of defects in DNA that could lead to malignancies; for this reason it is aptly called the “guardian of the genome”<sup>3, 4</sup>. However, a mutation in p53 can cause a cascade of mutations and DNA damage which promotes cancerous tissues.

## **1.2 Cancer Today**

Cancer is an exceptionally ubiquitous disease in Canada as well as worldwide. Not only is it incredibly pervasive in terms of the incidence rate and the mortality rate, it requires immense resources both fiscally and physically to treat. Unsurprisingly, cancer is the leading cause of death, and fourth costliest disease for Canadians, annually accounting for 30% of total mortality rates, and \$17.4 billion in treatment costs. 75500 Canadians are expected to have died of cancer in 2013, and one in four Canadians are expected to die from the disease in their lifetime<sup>5</sup>. An estimated 187600

Canadians will be diagnosed with a new cancer in 2013, and ultimately 41% of Canadian women, and 46% of Canadian men will develop cancer in their lifetimes<sup>1, 5</sup>. These cancers can differ greatly depending on their location of origin, and the specific line of cells involved<sup>2-4</sup>. Although there are many varieties of cancer, half of all new cancers in Canada will be one of lung, breast, colorectal, or prostate cancer. These four cancers have drastically different prognoses, with lung cancer being by far the most deadly, causing more deaths than the other three types combined<sup>5</sup>. One method by which the prognosis of cancer can be defined is the 5-year survival rate, which is the probability relative to a healthy individual that the cancer patient will survive at least 5 years. Lung cancer has a 5-year survival rate of 13%, while breast, colorectal, and prostate cancer have 83%, 61%, 95% 5-year survival rates, respectively. Considering all cancers, the Canadian Cancer Society has found that overall, 63% of persons diagnosed with cancer were still alive 5 years after their diagnosis; that is, cancer as a whole has a 63% 5-year survival rate in Canada<sup>5</sup>. It is evident from these numbers that lung cancer, or other particularly deadly cancers (such as pancreatic cancer, with a 5 year survival rate of 8%) are prominent causes of cancer deaths. If these cancers with a particularly poor prognosis were more treatable, we would likely see a marked increase in overall cancer survivability.

Notwithstanding, since 1989, an estimated 100000 cancer deaths, most of which would have been due to lung cancer, have been avoided<sup>5</sup>. Increasing public awareness concerning cancer and various carcinogens, in combination with a higher quality of cancer treatments, are credited with the estimated decrease in cancer deaths. On a population scale, some success has occurred due to public health interventions around cancer focusing on reducing alcohol and tobacco consumption, prolonged exposure to sunlight, and exposure to environmental carcinogens. In addition to these prevention efforts decreasing the estimated incidence of cancer, the 5-year survival for those who develop a cancer has increased for many cancers individually, and has increased by 7% overall since 1992-1994<sup>5</sup>. Although many people

who survive cancer go on to live healthy and productive lives, many physical and emotional challenges can persist after treatment<sup>5</sup>.

### **1.3 Radiation Therapy Today**

Radiation therapy, specifically external beam radiation therapy (XBRT), is one of the most common treatments for cancers<sup>1</sup>. This kind of therapy directs x-rays, gamma rays, or charged particles (most commonly electrons) of varying energies from outside of the body at the diseased tissues within the body in an effort to deposit a high enough dose of radiation to destroy cellular function and kill the cancerous cells<sup>1, 6-8</sup>. The type of radiation used varies from case to case and is dictated by the nature of cancer and the treatment goals, with superficial lesions being treated differently than deep seated lesions. Linear accelerators, or linacs, are the machines that are typically used to produce electrons and photons of various energies for the purpose of radiation treatment<sup>1, 7</sup>. Photons are the primary type of radiation used to treat carcinomas, and the energies used are ordinarily in the megavoltage (one million volts) range, with 6MV being common; in contrast, the energies used in imaging are typically in the one hundred kilovolt (one hundred thousand volts) range, with 120kV being common<sup>6</sup>. These energies define the peak energy of a photon beam spectrum, the average energy is near 1/3 the peak energy<sup>6, 9</sup>. The ultimate goal of radiation therapy is to deliver the maximum dose to the malignancy to ensure maximum tumour control probability (TCP) is achieved. In irradiating the lesion, it is inevitable that normal tissues will receive some dose due in part to their proximity to targeted (malignant) tissue. This limited dose may in some cases effect normal tissue complications, depending on the dose received, and the nature of the healthy tissue receiving the dose. This irradiation of otherwise healthy tissue may lead to further complications, and in a very small number of people, a second cancer may occur, usually 10-20 years after treatment<sup>1, 5</sup>. It is therefore also essential in radiation therapy that the

dose to the normal tissues adjacent to the lesion be minimized, thus minimizing the normal tissue complication probability (NTCP)<sup>6, 7</sup>. External beam radiation therapy is non-invasive, painless, and typically takes 15-30 minutes to complete, with the bulk of this time being spent performing patient setup procedures. Cases may vary from one to another, but a full treatment regimen generally consists of 3-8 weeks of five treatments, or fractions, per week. Radiation therapy may be paired with other treatment options, such as traditional surgery (as opposed to radiosurgery), and chemotherapy<sup>1</sup>.

The International Commission on Radiation Units and Measurements, or ICRU, introduced a set of volumes used in radiotherapy in 1993 and 1999<sup>10, 11</sup>. These volumes define the regions for which a therapeutic dose must be received to maximize TCP, and the regions for which there is a high probability of normal tissue complications under excessive irradiation. These volumes also account for uncertainties in tumour position as whole, including delineation, imaging, and setup uncertainties. These volumes are defined as the Gross Tumour Volume (GTV), Clinical Target Volume (CTV), Planning Target Volume (PTV), and Organs at Risk (OARs). These regions are depicted in figure 1.1.

The GTV represents the gross volume of the tumour, and is the innermost region depicted. This region contains the tumour proper, and is the region visible on the diagnostic image for which the radiation oncologist defines tumour bounds (contour). The CTV is a margin that represents the extents of microscopic disease expected to surround the tumour proper, but which is not visible. The CTV is less absolute in its precision because the extents of microscopic disease are harder to determine; as a result, the CTV invariably contains some amount of healthy tissue. The PTV represents the area the radiation treatment plans to irradiate. This volume adds geometrical margins around the GTV+CTV structure to account for the so-called internal margins (IM) and setup margins (SM).

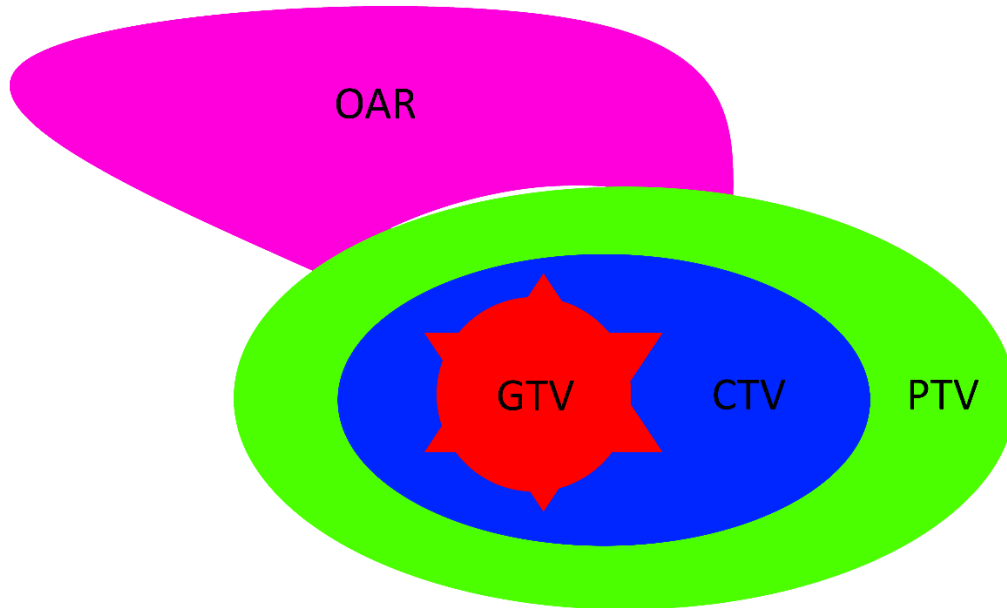


Figure 1.1 Illustration of the ICRU volumes defined in the treatment planning process. The gross tumour volume (GTV), clinical target volume (CTV), planning target volume (PTV), and organ at risk (OAR) are shown. It should be noted that the PTV is composed of the internal margin (IM) and setup margin (SM) together.

The IM is a margin added to account for inter-fraction and intra-fraction variations in tumour shape and position due to biological processes, such as bladder and rectum filling, respiration, involuntary muscle contractions (e.g., peristalsis), weight gain or loss, and cell water retention. The SM is a margin added to account for small errors in patient setup from day to day. With tumour location defined to mm accuracy, setup variations of a few mm become increasingly significant, and must be minimized. The PTV may be asymmetric around the GTV+CTV, as would be the case in the presence of preferred movement directions. However, the PTV always encompasses the entirety of the GTV+CTV substructure. OARs represent healthy organs that may be sensitive to the radiation treatment and dose within the structure must be minimized. An example of an OAR would be the rectum in the case of prostate cancer treated with external beam radiotherapy. The prostate must have a sufficient dose for a therapeutic outcome, but NTCP must be minimized for the adjacent rectum. The presence of OARs may necessitate a decrease in radiation dose to the tumour in an effort to mitigate damage

to the OAR. It is also clear from Figure 1.1 that there may be a considerable volume of healthy tissue receiving significant radiation dose due to uncertainties in disease extent, and other inter-fraction and intra-fraction variations.

The advent of Computed Tomography, or CT scans, in the 1970s has allowed for the 3D imaging of tumours and surrounding structures in the body. Prior to the start of the treatment regimen, every patient is subject to a planning CT, or CT simulation. This scan of the region of interest will be used to delineate the GTV, CTV, PTV, and any OARs that may be in the path of radiation meant for the PTV. Once the volumes are defined, an individualized multiple beam radiation treatment plan will be generated using the electron density numbers provided by the CT scan to determine how the radiation will interact with the surrounding matter<sup>7, 12</sup>. These innovations have allowed for the development of more accurate and specific three-dimensional treatment plans. An initial advancement arising from the possibility of a three-dimensional plan with multiple beams was 3D conformal radiation therapy<sup>7</sup>, where multiple beams would be shaped so as to conform to the spatial dimensions of the lesion being treated. More recently, intensity modulated radiation therapy (IMRT) has become commonplace. IMRT not only shapes the individual treatment beams, but alters the two-dimensional spatial intensity of each beam so as to better conform to the tumour as a whole<sup>7, 13</sup>. The improved accuracy of these methods of radiation delivery have diminished not only the volume of normal tissues irradiated unnecessarily, but the dose received by the normal tissues that are irradiated, lowering the overall NTCP<sup>7, 12</sup>. The improved spatial accuracy and reduced NTCP of IMRT could be exploited so as to escalate the dose delivered to the tumour, which would likely increase the TCP. Further advancements in optimizing radiation treatments have come in the form of tomotherapy, gating, and adaptive radiation treatment (ART). Tomotherapy is a treatment helical in nature, similar to CT, but with intensity modulated high energy radiation<sup>14</sup>. Gating refers to the practice of holding

radiation until the tumour is in a known, or expected position, such as at the full exhale portion of breathing motion<sup>15, 16</sup>. Adaptive radiotherapy changes the treatment to respond to the tumour, and may involve periodically generating new treatment plans as the lesion being treated shrinks in response to the radiation<sup>17</sup>.

These advancements have greatly improved spatial accuracy of radiation dose, necessitating imaging guidance to facilitate the correct localization of the region to be treated<sup>18-20</sup>. Image guided radiotherapy (IGRT) has as a result become commonplace, and has allowed for the reduction of setup margins in the PTV as positioning of the patient becomes more accurate<sup>21</sup>. In image guided radiotherapy, the patient is imaged prior to the start of a radiotherapy fraction. Then, the image generated is compared to the associated image from the initial CT simulation scan, and undergoes what is known as image registration. Easily visible structures, such as bony anatomy, are matched between the two images. The patient is then translated in any necessary direction to facilitate the matching, replicating patient setup at the beginning of every fraction. While this method helps ensure consistent patient setup and reduces planning margins<sup>21</sup>, it does not take into account variances in relative tumour morphology and position changes inter-fraction or intra-fraction. It is also likely that as the course of radiation therapy progresses, the tumour will shrink as it responds to the radiation, invalidating the accuracy of the initial scan used as the benchmark for setup. This is the motivation for an adaptive radiotherapy regimen, in which the patient would be imaged at intervals throughout the treatment regimen so as to adapt the treatment plan and refresh the benchmark image used in IGRT.

There are a number of methods by which we could employ IGRT and acquire a pre-treatment image to increase inter-fractional confidences<sup>18, 19</sup>. One such method is by the use of an electronic portal imaging device, or EPID, which is characteristically integrated opposite the treatment head of

a linear accelerator. The EPID is a planar device that will generate a two - dimensional projection radiograph of a patient with the transit megavoltage treatment beam, and can be used fluoroscopically<sup>22, 23</sup>. This image will be compared to the CT data set by means of a digitally reconstructed radiograph (DRR) derived from the CT dataset. This DRR mimics the standard two-dimensional projection radiograph you would obtain via use of the EPID. Because the EPID uses the treatment beam to image, it can be used either as an on-line dosimeter for monitoring the dose received by the patient, or for quality assurance of IMRT treatment plans prior to patient delivery<sup>24, 25</sup>. Moreover, it is also possible to rotate the EPID system around the patient in an effort to generate a megavoltage cone beam computed tomography (MV-CBCT) dataset which would provide more robust three - dimensional volumetric information<sup>26, 27</sup>. However, the EPID is not without deficiencies: the image is generated with a megavoltage beam, which suffers from inferior contrast when compared to kilovoltage imaging systems (such as standard CT). Correspondingly, the EPID uses the transit treatment beam to image during treatment; as a result the quality of the images during treatments can suffer since the beam will be optimized for radiotherapy, rather than imaging. One final deficiency in EPID imaging is that it is in most cases two-dimensional, which overlays three-dimensional structures on a two-dimensional surface. To circumvent this, a MV-CBCT could be performed using the EPID, however, this megavoltage dataset would still suffer from poor contrast, and continue to dose the patient in excess of their treatment plan.

A common alternative image guidance method to the EPID is to use an onboard cone beam computed tomography device, typically mounted on an axis perpendicular to the direction of the treatment beam<sup>28, 29</sup>. This CBCT is a kilovoltage system, and as such would offer greater contrast and detail in the acquired dataset. The cone beam system would be rotated around the patient prior to treatment, collecting two-dimensional images, which will be reconstructed to form full three-dimensional volumetric representation of the

patient anatomy. Either the three-dimensional dataset, or two-dimensional images (or a select subset of them) could be used for image guidance, though the use of a two-dimensional image would not be as robust in image registration as a three-dimensional volumetric representation. Despite yielding improved images when compared to the EPID, the onboard imaging system (OBI) is not capable of dosimetric verification as is the EPID. As was the case with the EPID, ionizing radiation is still being used to generate an image. This radiation is not included in patient plans, and is indiscriminate in interactions with diseased and healthy tissues.

The EPID and CBCT systems have major disadvantages in that they cannot track patient anatomy or defined volumes, such as the PTV, in real time. In an effort to circumvent the shortcomings of the EPID and CBCT systems, a method of electromagnetic tracking has been developed<sup>30, 31</sup>. Radiofrequency beacons are first implanted into the patient at known locations, which are confirmed via a CT scan or a number of projection radiographs. The beacons will initially be placed around a volume of interest, such as the PTV, in an effort to localize its centroid. A source array is positioned near the patient during treatment, which will measure the radiofrequency electromagnetic radiation emitted by the beacons to localize their three-dimensional spatial locations. The centroid of the volume can thus be determined, and tracked in real time, improving patient setup, and allowing for the possibility of a semi-adaptive treatment. The spatial error in tracking the centroid of the beacons has been demonstrated to be small, but nonetheless must be included in margins for patient setup<sup>32</sup>. While the beacons in this tracking method are well localized, it cannot be assumed that they do not move with respect to their initial placements throughout a treatment regimen. The centroid defined by the beacons may shift with respect to the centroid originally defined (the PTV, for instance), and this error must also be taken into account. Furthermore, the beacons are not capable of the definition of a two-dimensional or three-dimensional contour to account for morphological changes over time. Finally, the insertion of the

beacons requires surgery, which can be generally uncomfortable, and carries risks of infection<sup>33</sup>.

## 1.4 Linac-MR

The current modalities of image guidance for radiotherapy have several shortcomings that should be addressed. Most of the aforementioned IGRT methods image the patient before initializing the treatment to minimize setup errors. As a result, these methods are not capable of real time tumour tracking, and will therefore not account for intra-fractional tumour motions, such as respiration, discussed previously. Additionally, these pre-treatment images will be compared to a planning CT which will not account for inter-fractional tumour variations. Consequently, a large margin accounting for these errors still needs to be included in the PTV. This margin will not accurately represent the spatial imaging capabilities of these various modalities due to the uncertainty in tumour position. If we were able to image the patient during treatment in real time, we would be able to track the full three-dimensional structure of the tumour, and guide our radiation accordingly. Advanced real time adaptive radiotherapy, (ART<sup>2</sup>), would circumvent the problems enduring in current IGRT, and necessitate a smaller PTV margin, allowing for the escalation of dose and a better therapeutic outcome. There are a number of groups globally pursuing the integration of a magnetic resonance imager (MR imager) with an external beam treatment for just this purpose<sup>34-39</sup>.

Magnetic resonance imaging (MRI) is utilized in these systems for a multitude of reasons. MRI offers superior soft tissue contrast greatly improves the delineation of tumours and surrounding tissues<sup>7</sup>. This improved allocation of the GTV and OARs can help to shrink the PTV, and define the bounds of tumours we may have otherwise not been able to accurately locate, overall improving the therapeutic outcome for patients.

MRI is non-ionizing, therefore that the patient will not receive a superfluous dose for the purposes of real time tumour tracking. This is a great advantage over the EPID and OBI IGRT methods currently employed. Finally, the MR imager is capable of promptly obtaining three-dimensional images without the need for rotation. This benefits a radiotherapy treatment in that the treatment head of the linac can rotate freely to deliver radiation without interfering with the imaging capabilities of the MRI. The Linac-MR is capable of imaging the tumour in real time during treatment without dosing the patient unnecessarily. The images obtained will, with the aid of a multi leaf collimator (MLC), allow for the tracking of the tumour with the radiation beam. Subsequently, we may shrink the required margins for intra-fraction tumour motion and increase the dose delivered to the tumour, thereby increasing TCP and decreasing NTCP<sup>6</sup>.

The ViewRay group<sup>34, 35</sup> uses a split solenoid MRI device coupled with three Cobalt 60 (<sup>60</sup>Co) sources. The split solenoid magnet design requires the radiation to be delivered in a transverse magnetic field orientation. A transverse field configuration is defined as the case in which the radiation sources are perpendicular to the static magnetic field used by the MRI. The use of live sources also has its shortcomings. The sources will periodically need to be changed, and the treatments will get progressively longer as the sources decay. It also adds another avenue for human error in accounting for the activity of the individual sources. Furthermore, the movement of the source from treatment to shielded positions takes valuable time, from a tumour tracking perspective. The UMC Utrecht<sup>38, 39</sup> overcomes the problems arising from the use of a live source by using an Elekta linac in conjunction with a Phillips 1.5T MRI machine. Again, the magnet is of a solenoidal design, and the linac is positioned in a transverse magnetic field configuration. This design offers superior radiation characteristics to the ViewRay design, but this radiation must pass through the cryostat (cooling system) of the MRI device, which will introduce new dosimetric challenges. Our group at the Cross Cancer Institute (CCI) in Edmonton, Canada,

couples a low-field bi-planar magnet with a 6MV accelerator. It should be noted that low field strength magnetic fields of 0.2T have been found to be sufficient for tumour tracking<sup>40</sup>. The bi-planar magnet and linac assembly will rotate around the patient as a whole, and will be capable of both transverse and longitudinal magnetic field orientations. Specifically, the rotating bi-planar (RBP) design can have the linear accelerator positioned such that the radiation is perpendicular to the magnetic field (transverse, see Figure 1.2), or parallel to the magnetic field (longitudinal, see Figure 1.3).

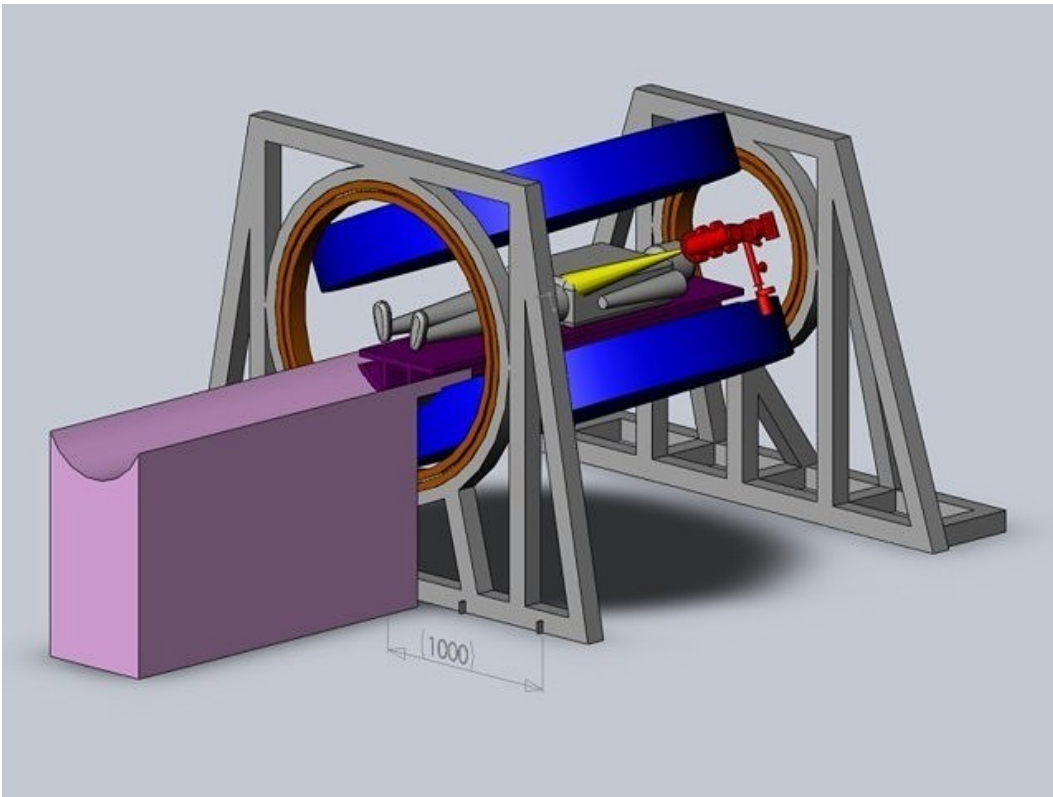


Figure 1.2 Transverse configuration of the rotating bi-planar (RBP) Linac-MR system developed at the CCI. The Linear accelerator is positioned laterally at the open side of the bi-planar magnet assembly. Pole plates are shown in blue, and radiation beam in yellow.

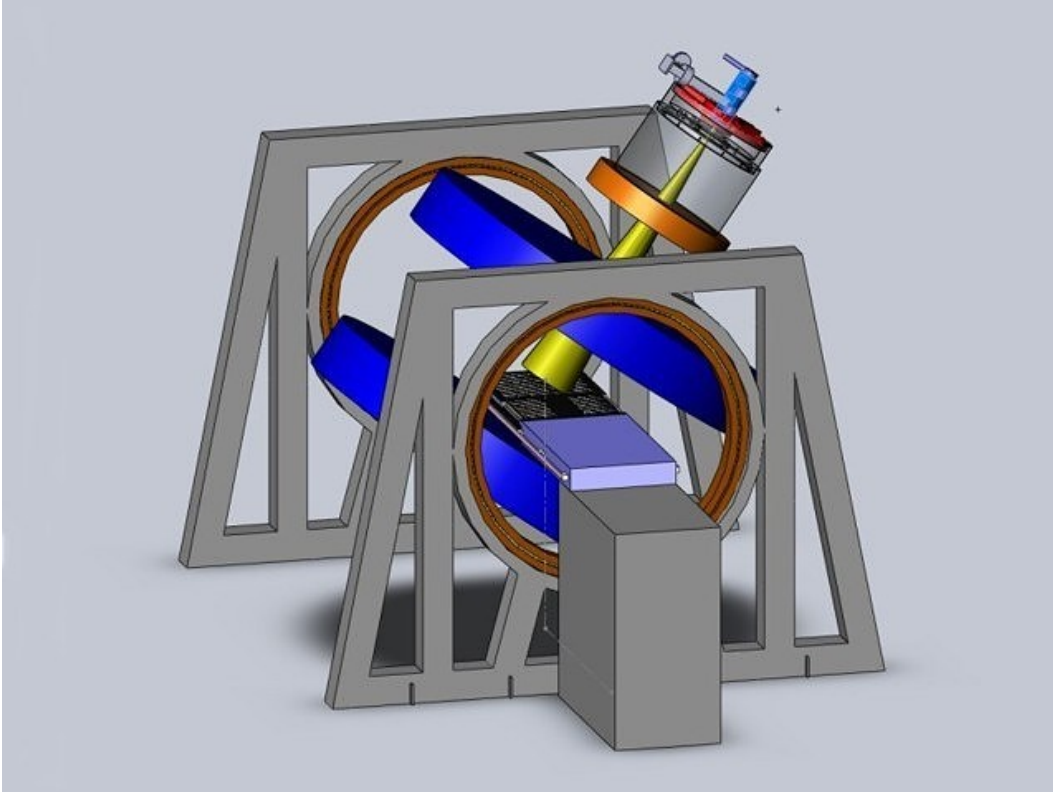


Figure 1.3 Longitudinal configuration of the rotating bi-planar (RBP) Linac-MR system developed at the CCI. The linear accelerator is positioned above a pole plate, and will irradiate through a hole in the pole plate. Pole plates are shown in blue, and radiation beam in yellow.

In the transverse magnetic field case (figure 1.2), the linac would be positioned on an open end of the bi-planar magnet assembly, and irradiate between the two magnet poles. Such a prototype exists at the CCI, the first images obtained by an MRI with concurrent linac irradiation were obtained using this prototype<sup>37</sup>. Alternatively, in the longitudinal case the 6MV linac could be positioned above one of the poles of the bi-planar magnet, and would irradiate the target volume through a hole in the pole plate as can be seen in figure 1.3. Such a prototype (figure 1.3) also exists at the CCI, and is capable of imaging both humans and phantoms.

## 1.5 Motivation and Framework

Both transverse and longitudinal RBP configurations have been studied in order to quantify their inherent dosimetry characteristics<sup>41, 42</sup>. Transverse magnetic field Linac-MR devices have been found to suffer from perturbations in dose distributions, particularly at higher magnetic field strengths<sup>41, 43-48</sup>. Although it may be possible to adapt treatment plans to account for some of these dose effects<sup>49</sup>, some will persist. Transverse field dose effects include the alteration of percent depth doses, and lateral shifts of the dose penumbra, including the creation of hot (overdosed) and cold (underdosed) spots on either side of the beam<sup>41</sup>. Within homogeneous media, where electronic equilibrium exists, the dose deposition is unaltered by a transverse magnetic field. However, the so called electron return effect (ERE) alters the dose deposition at tissue interfaces (such as the tissue/lung interface), whereby electrons entering a relatively sparse media will curve upstream and re-enter the denser media, creating hot and cold spots in inhomogeneous media<sup>45</sup>. Longitudinal magnetic fields do not suffer from the ERE concerns, or lateral shift of the dose penumbra seen in transverse fields; in fact, longitudinal fields restrict the lateral spread of secondary electrons, and may be used to confine radiotherapy dose<sup>50, 51</sup>. Correspondingly, it has been shown that longitudinal fields can increase dose to the PTV, potentially shielding surrounding healthy tissues from errant dose<sup>41</sup>. This effect is more pronounced at higher field strengths and in lower density media, such as lung tissue. These dose effects are resultant from the Lorentz force acting on the secondary electrons, those which will ultimately deposit dose in the medium. A more vigorous treatment of the Lorentz force will be examined in chapter 2.

Radiation detectors are a vital part of clinical practice, and are involved in everything from beam commissioning and output verification to patient quality assurance<sup>6, 8, 52-54</sup>. Commissioning a linear accelerator is the process by which the therapy beam is characterized and calibrated; it is a

lengthy process involving many lateral and depth dose profiles using various field sizes. Output verification is a periodic check that the accelerator is consistently outputting the expected dose of radiation. Patient quality assurance differs from output verification in that it delivers the exact IMRT fields to be used in treatment of the patient; this allows for analysis of the patient plan itself. The radiation detectors used vary in their design, and in the materials employed in their construction. However, the vast majority of detectors are assembled not only with a number of different materials, but in various dimensionalities as well. They are nearly exclusively inhomogeneous in nature, necessarily suffering from dose variations due to ERE and other effects when in the presence of a magnetic field. The ubiquitous use of ion chambers and various solid state detectors in radiation therapy is unlikely to change with the advent of the Linac-MR, and as such their response to the magnetic field associated with the Linac-MR must be investigated.

To date, there have been various studies, looking at the use and response of specific subsets of detectors in Linac-MR environments<sup>55-60</sup>. This thesis will continue that work, and evaluate the dose response of various ion chambers and solid state detectors for use in a magnetic field environment. Dose response will be defined herein as the ratio of the detector's signal (or dose deposited within the detector) in the presence of a magnetic field to that in the absence of a magnetic field. This magnetic field dose response will be charted as a function of field strength and relative orientation of magnetic field, radiation beam, and detector axis. The overall goal of this work is the modification of the nationally accepted dosimetry calibration protocol (TG-51)<sup>54, 61</sup> for use in Linac-MR environments. This modification is expected to manifest as a correction factor for a specified detector in a certain orientation at a known magnetic field strength, and will be the inverse of the determined dose response pertaining to a particular setup (a correction factor of 0.935 corresponds to a dose response of 1.07). The Monte Carlo code PENELOPE<sup>62-64</sup> will be employed to model the various

detectors and magnetic fields, and to simulate the dose deposited within the various detectors at specified field strengths and orientations. When possible, small electromagnets will be utilized to measure the dose response and validate the simulation results. Further, water tank Monte Carlo studies - studies of detectors immersed within a volume of water - will investigate the use of detectors in scanning an incident photon beam under various magnetic field orientations.

Chapter 1 has been a brief overview of cancer, and an introduction into modern radiotherapy. We have explored some of the possible causes and associated mechanics of cancer growth in humans, and investigated the impact cancer has on Canadians. Modern radiotherapy, a common treatment of many cancers, was then discussed so as to give the reader a basic understanding of current clinical practices and limitations. Further, the Linac-MR was introduced as a path for the advancement of radiotherapy as a whole. Issues regarding dose deposition and measurement were introduced, and the need to accurately determine dose within the magnetic field environment of the Linac-MR was rationalised. A proposal to continue previous work in magnetic field dose response was then presented.

Chapter 2 attempts to give the reader the basic tools required to both understand the methods employed in this study, as well as analyze the resultant data. A short review of electromagnetic fields, and the forces they exert on charged particles will be explored. The fundamentals of radiation interactions of photons and electrons in matter will also be presented. To facilitate the understanding of Monte Carlo techniques, selected statistics concepts and results will be examined. The simulation of radiation in electromagnetic fields through the use of the Monte Carlo code PENELOPE will then be considered, using concepts within chapter 2 up to this point. Finally, the mechanisms of radiation detection for the types of detectors to be investigated (ionisation chambers, diamond detectors, diode detectors, and luminescence detectors) will be discussed. A short synopsis of the

present accelerator output calibration protocol, TG-51, will also be presented.

Chapter 3 will explore the various orientations of magnetic field, radiation beam, and detector to be studied. The parameters of the PENELOPE code system governing the simulation of these detectors will then be laid forth, and will be followed by the simulation geometries to be assessed. The simulation geometries of interest vary depending on detector type, and are either in air, or within a water tank. Following these geometries, a detailed account of the individual detector models will be presented. Subsequent to the simulation implementation, details of the measurement setups will be provided. The procedure for the measurement of dose response with the 4 available detectors (PR06C, PTW60003, IBA PFD, Landauer Nanodot) in both transverse and longitudinal magnetic fields will be detailed.

Chapter 4 will present the simulation and measured data for all orientations discussed in chapter 3 on a detector by detector basis. Measured and simulated values will be compared, and the accuracy of the simulations can in part be inferred by their agreement with measurement values. Ionisation chamber results will be compared amongst one another, as will the solid state detector results. The apparent mechanisms governing the response of the respective detectors will also be introduced. Water tank results will be evaluated on a detector by detector basis; this evaluation will assess both the possible use of the detector to scan a radiation beam in a magnetic field, and the accuracy of the in-air response.

Chapter 5 will provide a brief overview of the contents of this work; this will be followed by a succinct review of the findings of the simulation and measurements outlined in chapter 4. All of the individual detector types will then have their use within the magnetic field environment of the Linac-MR evaluated in various circumstances.

## 1.6 References

- 1 Canadian Cancer Society, *Cancer Information*, www.cancer.ca (2014).
- 2 R.A. Weinberg, *The Biology of Cancer*, 2 Edition (Garland Science, New York, NY, 2013).
- 3 W.M. Becker, L.J. Kleinsmith, and J. Hardin, *The World of the Cell*, 5 Edition (Benjamin Cummings, San Francisco, CA, 2003).
- 4 N.A. Campbell and J.B. Reece, *Biology*, 6 Edition (Benjamin Cummings, San Francisco, CA, 2002).
- 5 Canadian Cancer Society and Stats Canada, *Canadian Cancer Statistics 2013* (Toronto, ON, 2013).
- 6 H.E. Johns and J.R. Cunningham, *The Physics of Radiology* (Charles C Thomas, Springfield, Illinois, 1983).
- 7 J. Van Dyk, *The Modern Technology of Radiation Oncology* (Medical Physics Publishing, Wisconsin, 2005).
- 8 F. Attix, *Introduction to Radiological Physics and Radiation Dosimetry* (WILEY-VCH, Weinheim, 2004).
- 9 D. Sheikh-Bagheri and D.W.O. Rogers, "Monte Carlo calculation of nine megavoltage photon beam spectra using the BEAM code," *Med. Phys.* **29**(3), 391–402 (2002).
- 10 ICRU, *ICRU Report 50: Prescribing, Recording, and Reporting Photon Beam Therapy* (1993).
- 11 ICRU, *ICRU Report 62: Prescribing, Recording and Reporting Photon Beam Therapy (Supplement to ICRU Report 50)* (1999).
- 12 J. Bernier, E.J. Hall, and A. Giaccia, "Radiation oncology: a century of achievements.," *Nat. Rev. Cancer* **4**(9), 737–47 (2004).
- 13 C.X. Yu, C.J. Amies, and M. Svatos, "Planning and delivery of intensity-modulated radiation therapy," *Med. Phys.* **35**(12), 5233 (2008).
- 14 T.R. Mackie, "History of tomotherapy," *Phys. Med. Biol.* **51**(13), R427–53 (2006).

- 15 K.M. Langen and D.T. Jones, "Organ motion and its management.," *Int. J. Radiat. Oncol. Biol. Phys.* **50**(1), 265–78 (2001).
- 16 P. Giraud and R. Garcia, "Respiratory gating for radiotherapy: main technical aspects and clinical benefits," *Bull. Cancer* **97**(7), 847–56 (2010).
- 17 X.A. Li, *Adaptive radiation therapy* (CRC Press, Boca Raton, Fla, 2011).
- 18 D. Verellen, M. De Ridder, N. Linthout, K. Tournel, G. Soete, and G. Storme, "Innovations in image-guided radiotherapy.," *Nat. Rev. Cancer* **7**(12), 949–60 (2007).
- 19 L.A. Dawson and D.A. Jaffray, "Advances in image-guided radiation therapy," *J. Clin. Oncol.* **25**(8), 938–946 (2007).
- 20 D.A. Jaffray, "Image-guided radiotherapy: from current concept to future perspectives," *Nat. Rev. Clin. Oncol.* **9**(12), 688–699 (2012).
- 21 J. Stroom and B. Heijmen, "Geometrical uncertainties, radiotherapy planning margins, and the ICRU-62 report," *Radiother. Oncol.* **64**, 75–83 (2002).
- 22 H. Meertens, M. Van Herk, J. Bijhold, and H. Bartelink, "First clinical experience with a newly developed electronic portal imaging device," *Phys. Med. Biol.* **18**(November 1989), 1173–1181 (1990).
- 23 J. Leong, "Use of digital fluoroscopy as an on-line verification device in radiation therapy.," *Phys. Med. Biol.* **31**(9), 985–92 (1986).
- 24 V.N. Hansen, "The application of transit dosimetry to precision radiotherapy," *Med. Phys.* **23**(5), 713 (1996).
- 25 K.L. Pasma, B.J.M. Heijmen, M. Kroonwijk, and a. G. Visser, "Portal dose image (PDI) prediction for dosimetric treatment verification in radiotherapy. I. An algorithm for open beams," *Med. Phys.* **25**(6), 830 (1998).
- 26 J. Pouliot, A. Bani-Hashemi, M. Svatos, F. Ghelmansarai, M. Mitschke, M. Aubin, P. Xia, O. Morin, K. Bucci, M. Roach, P. Hernandez, Z. Zheng, D. Hristov, and L. Verhey, "Low-dose megavoltage cone-beam CT for radiation therapy," *Int. J. Radiat. Oncol. Biol. Phys.* **61**(2), 552–560 (2005).

- 27 O. Morin, A. Gillis, J. Chen, M. Aubin, M.K. Bucci, M. Roach, and J. Pouliot, "Megavoltage cone-beam CT: system description and clinical applications," *Med. Dosim.* **31**(1), 51–61 (2006).
- 28 D.A. Jaffray, J.H. Siewerdsen, J.W. Wong, and A.A. Martinez, "Flat-panel cone-beam computed tomography for image-guided radiation therapy," **53**(5), 1337–1349 (2002).
- 29 D.A. Jaffray, D.G. Drake, M. Moreau, A.A. Martinez, and J.W. Wong, "A radiographic and tomographic imaging system integrated into a medical linear accelerator for localization of bone and soft-tissue targets," **45**(3), 773–789 (1999).
- 30 L. Santanam, K. Malinowski, J. Hubenschmidt, S. Dimmer, M.L. Mayse, J. Bradley, A. Chaudhari, K. Lechleiter, S.K.M. Goddu, J. Esthappan, S. Mutic, D. a Low, and P. Parikh, "Fiducial-based translational localization accuracy of electromagnetic tracking system and on-board kilovoltage imaging system.," *Int. J. Radiat. Oncol. Biol. Phys.* **70**(3), 892–9 (2008).
- 31 J.M. Balter, J.N. Wright, L.J. Newell, B. Friemel, S. Dimmer, Y. Cheng, J. Wong, E. Vertatschitsch, and T.P. Mate, "Accuracy of a wireless localization system for radiotherapy.," *Int. J. Radiat. Oncol. Biol. Phys.* **61**(3), 933–7 (2005).
- 32 D.W. Litzenberg, I. Gallagher, K.J. Masi, C. Lee, J.I. Prisciandaro, D. a Hamstra, T. Ritter, and K.L. Lam, "A measurement technique to determine the calibration accuracy of an electromagnetic tracking system to radiation isocenter.," *Med. Phys.* **40**(8), 081711 (2013).
- 33 C.S. Price and L.A. Savitz, *Improving Measurement of Surgical Site Infection Risk Stratification / Outcome Detection. Final Report* (Rockville, MD, 2012).
- 34 J.F. Dempsey, D. Benoit, J.R. Fitzsimmons, A. Haghigat, J.G. Li, D.A. Low, S. Mutic, J.R. Palta, H.E. Romeijn, and G.E. Sjoden, "A device for real time 3D image-guided IMRT," *Int. J. Radiat. Oncol. Biol. Phys.* **63**, S202–S202 (2005).
- 35 J. Dempsey, B. Dionne, J. Fitzsimmons, A. Haghigat, J. Li, D. Low, S. Mutic, J. Palta, H. Romeijn, and G. Sjoden, "A real-time MRI guided external beam radiotherapy delivery system," *Med. Phys.* **33**(6), 2254 (2006).

- 36 B.G. Fallone, M. Carlone, B. Murray, S. Rathee, T. Stanescu, S. Steciw, K. Wachowicz, and C. Kirkby, "Development of a Linac-MRI system for real-time ART," *Med. Phys.* **34**, 2547–2547 (2007).
- 37 B.G. Fallone, B. Murray, S. Rathee, T. Stanescu, S. Steciw, S. Vidakovic, E. Blosser, and D. Tymofichuk, "First MR images obtained during megavoltage photon irradiation from a prototype integrated linac-MR system," *Med. Phys.* **36**(6), 2084–2088 (2009).
- 38 B.W. Raaymakers, J.J.W. Lagendijk, J. Overweg, J.G.M. Kok, a J.E. Raaijmakers, E.M. Kerkhof, R.W. van der Put, I. Meijnsing, S.P.M. Crijns, F. Benedosso, M. van Vulpen, C.H.W. de Graaff, J. Allen, and K.J. Brown, "Integrating a 1.5 T MRI scanner with a 6 MV accelerator: proof of concept.," *Phys. Med. Biol.* **54**(12), N229–37 (2009).
- 39 J.J.W. Lagendijk, B.W. Raaymakers, A.J.E. Raaijmakers, J. Overweg, K.J. Brown, E.M. Kerkhof, R.W. van der Put, B. Hårdemark, M. van Vulpen, and U.A. van der Heide, "MRI/linac integration," *Radiother. Oncol.* **86**(1), 25–29 (2008).
- 40 J. Yun, E. Yip, K. Wachowicz, S. Rathee, M. Mackenzie, D. Robinson, and B.G. Fallone, "Evaluation of a lung tumor autocontouring algorithm for intrafractional tumor tracking using low-field MRI: a phantom study.," *Med. Phys.* **39**(3), 1481–94 (2012).
- 41 C. Kirkby, T. Stanescu, S. Rathee, M. Carlone, B. Murray, and B.G. Fallone, "Patient dosimetry for hybrid MRI-radiotherapy systems," *Med. Phys.* **35**(3), 1019–1027 (2008).
- 42 C. Kirkby, B. Murray, S. Rathee, and B.G. Fallone, "Lung dosimetry in a linac-MRI radiotherapy unit with a longitudinal magnetic field," *Med. Phys.* **37**(9), 4722–4732 (2010).
- 43 A.J.E. Raaijmakers, B.W. Raaymakers, and J.J.W. Lagendijk, "Magnetic-field-induced dose effects in MR-guided radiotherapy systems: dependence on the magnetic field strength.," *Phys. Med. Biol.* **53**(4), 909–23 (2008).
- 44 A.J.E. Raaijmakers, B.W. Raaymakers, and J.J.W. Lagendijk, "Experimental verification of magnetic field dose effects for the MRI-accelerator.," *Phys. Med. Biol.* **52**(14), 4283–91 (2007).
- 45 A.J.E. Raaijmakers, B.W. Raaymakers, and J.J.W. Lagendijk, "Integrating a MRI scanner with a 6 MV radiotherapy accelerator:

- dose increase at tissue-air interfaces in a lateral magnetic field due to returning electrons.," *Phys. Med. Biol.* **50**(7), 1363–76 (2005).
- 46 B.W. Raaymakers, A.J.E. Raaijmakers, a N.T.J. Kotte, D. Jette, and J.J.W. Lagendijk, "Integrating a MRI scanner with a 6 MV radiotherapy accelerator: dose deposition in a transverse magnetic field," *Phys. Med. Biol.* **49**(17), 4109–4118 (2004).
- 47 A.J.E. Raaijmakers, MR-guided radiotherapy : magnetic field dose effects (Ph.D. Thesis, Utrecht University, 2008).
- 48 A.J.E. Raaijmakers, B.W. Raaymakers, S. van der Meer, and J.J.W. Lagendijk, "Integrating a MRI scanner with a 6 MV radiotherapy accelerator: impact of the surface orientation on the entrance and exit dose due to the transverse magnetic field.," *Phys. Med. Biol.* **52**(4), 929–39 (2007).
- 49 A.J.E. Raaijmakers, B. Hårdemark, B.W. Raaymakers, C.P.J. Raaijmakers, and J.J.W. Lagendijk, "Dose optimization for the MRI-accelerator: IMRT in the presence of a magnetic field.," *Phys. Med. Biol.* **52**(23), 7045–54 (2007).
- 50 A. Bielajew, "The effect of strong longitudinal magnetic fields on dose deposition from electron and photon beams," *Med. Phys.* **20**(4), 1171–1179 (1993).
- 51 Y. Chen, A.F. Bielajew, D.W. Litzenberg, J.M. Moran, and F.D. Becchetti, "Magnetic confinement of electron and photon radiotherapy dose: A Monte Carlo simulation with a nonuniform longitudinal magnetic field," *Med. Phys.* **32**(12), 3810 (2005).
- 52 S.N. Rustgi and D.M.D. Frye, "Dosimetric characterization of radiosurgical beams with a diamond detector," *Med. Phys.* **22**(12), 2117–2121 (1995).
- 53 M. Bucciolini, F. Banci Buonamici, S. Mazzocchi, C. De Angelis, S. Onori, and G. a. P. Cirrone, "Diamond detector versus silicon diode and ion chamber in photon beams of different energy and field size," *Med. Phys.* **30**(8), 2149–2154 (2003).
- 54 P.R. Almond, P.J. Biggs, B.M. Coursey, W.F. Hanson, M.S. Huq, R. Nath, and D.W. Rogers, "AAPM's TG-51 protocol for clinical reference dosimetry of high-energy photon and electron beams.," *Med. Phys.* **26**(9), 1847–70 (1999).

- 55 M. Reynolds, B. Fallone, and S. Rathee, "Dose response of selected ion chambers in applied homogeneous transverse and longitudinal magnetic fields," *Med. Phys.* **40**(4), 042102 (2013).
- 56 M. Reynolds, B.G. Fallone, and S. Rathee, "Dose response of selected solid state detectors in applied homogeneous transverse and longitudinal magnetic fields," *Med. Phys.* **41**(9), 092103 (2014).
- 57 I. Meijnsing, B.W. Raaymakers, A.J.E. Raaijmakers, J.G.M. Kok, L. Hogeweg, B. Liu, and J.J.W. Lagendijk, "Dosimetry for the MRI accelerator: the impact of a magnetic field on the response of a Farmer NE2571 ionization chamber.," *Phys. Med. Biol.* **54**(10), 2993–3002 (2009).
- 58 K. Smit, B. Asselen, J.G.M. Kok, J.J.W. Lagendijk, and B. Raaymakers, "Reference Dosimetry for An MRI-Linac The Magnetic Field," *Med. Phys.* **39**(6), 4010–4011 (2012).
- 59 B. Raaymakers, K. Smit, G.H. Bol, M.R. Van den Bosch, S.P.M. Crijns, J.G.M. Kok, and J.J.W. Lagendijk, "Dosimetry in Strong Magnetic Fields; Issues and Opportunities," *Radiother. Oncol.* **103**, S170 (2012).
- 60 S. Goddu, O. Pechenaya Green, and S. Mutic, "TG-51 Calibration of First Commercial MRI-Guided IMRT System in the Presence of 0.35 Tesla Magnetic Field," *Med. Phys.* **39**, 3968 (2012).
- 61 M. McEwen, L. DeWerd, G. Ibbott, D. Followill, D.W.O. Rogers, S. Seltzer, and J. Seuntjens, "Addendum to the AAPM's TG-51 protocol for clinical reference dosimetry of high-energy photon beams.," *Med. Phys.* **41**(4), 041501 (2014).
- 62 J. Baro, J. Sempau, J.M. Fernández-Varea, and F. Salvat, "PENELOPE: an algorithm for Monte Carlo simulation of the penetration and energy loss of electrons and positrons in matter," *Nucl. Instruments Methods Phys. Res.* (100), 31–46 (1995).
- 63 J. Sempau, J.M. Fernández-Varea, E. Acosta, and F. Salvat, "Experimental benchmarks of the Monte Carlo code penelope," *Nucl. Instruments Methods Phys. Res. Sect. B Beam Interact. with Mater. Atoms* **207**(2), 107–123 (2003).
- 64 F. Salvat, J.M. Fernandez-Varea, and J. Sempau, *PENELOPE: A code system for Monte Carlo simulation of electron and photon transport* (2006).

# Chapter 2: Theory

## 2.1 Electromagnetic Fields

Electromagnetic fields govern the forces acting on electrically charged particles. One can imagine that these charged particles will be abundant in a given medium undergoing irradiation. Section 2.4 will examine radiation interactions in matter, and the generation of charged particles in greater detail. In the interim it is sufficient to note that electrons are generated in vivo under photon irradiation, and it is these electrons which deposit energy (radiation dose) in the medium<sup>1,2</sup>. The Linac-MR device pictured in figures 1.2 and 1.3 will introduce a significant magnetic field within the volume irradiated by photons<sup>3</sup>. As such, it is necessary to understand the interactions of the charged electrons depositing dose and the static magnetic field of the MR imager. The Maxwell equations governing electricity and magnetism will be explored in this section to facilitate this understanding.

The following discourse on electromagnetism draws from the standard physics texts of Griffiths and Jackson on electrodynamics<sup>4, 5</sup>. Unless otherwise specified, the reader can assume that the equations and associated discussion in the following section can be found in either of these texts. For more rigorous analysis and derivation the reader is directed to these texts.

Electric charge is an inherent property of hadrons and leptons (such as protons and electrons), and can be positive or negative in nature. These positive and negative charges produce electric fields that define the force which acts upon other electric charges in their vicinity. The electric field of a point charge in space is defined as:

$$\mathbf{E} = \frac{1}{4\pi\epsilon_0} \frac{q}{r^2} \hat{\mathbf{r}} \quad (2-1)$$

where  $\mathbf{E}$  is the electric field of interest, expressed in newtons per coulomb (N/C),  $q$  is the electric charge in coulombs (C) of the point charge which produces the field,  $r$  is the magnitude of the radial distance in meters (m) in space from the point charge, and  $\hat{\mathbf{r}}$  its unit vector (expressing direction).  $\epsilon_0$  is the permittivity of free space expressed in  $C^2/Nm^2$ , and characterizes the ability of the medium (i.e. free space) to permit or conduct an electric field. This field can be generalized for any charge distribution  $dq$  by integrating over the charge distribution of interest.

$$\mathbf{E} = \frac{1}{4\pi\epsilon_0} \int \frac{dq}{r^2} \hat{\mathbf{r}} \quad (2-2)$$

This expression simply states that the total electric field at some point is the linear superposition of the individual electric fields generated by the distribution of charges  $dq$  acting on that point. Equation 2-2 can be further generalized by introducing the notion of electric flux, which characterizes the magnitude of the electric field passing through a surface element  $dA$ .

$$\varphi_E = \int \mathbf{E} \cdot d\mathbf{A} \quad (2-3)$$

where  $\varphi_E$  is the electric flux through the surface defined by  $\int dA$ . Considering the electric flux through a closed sphere of radius  $r$ , equations 2-2 and 2-3 can be combined to define what is known as Gauss's law as follows:

$$\oint \mathbf{E} \cdot d\mathbf{A} = \int \frac{1}{4\pi\epsilon_0} \frac{dq}{r^2} \hat{\mathbf{r}} \cdot d\mathbf{A} = \frac{1}{\epsilon_0} \int dq = \frac{Q_{encl}}{\epsilon_0} \quad (2-4)$$

Gauss's law is one of four equations defined by James Clerk Maxwell, known as the Maxwell equations, which govern electricity and magnetism.

This law quite simply states that the electric field flux over some closed surface is defined by the total charge contained in the volume enclosed by the surface. Applying the divergence theorem (equation 2-5) to Gauss's law in integral form (equation 2-4) yields the differential form, defined in equation 2-6 where  $\rho$  is the volume electric charge density. The divergence theorem states that the surface integral of a vector field  $\mathbf{F}$  over a closed surface  $S$  can be written as the integral of the divergence of the vector field over the volume  $V$  enclosed by  $S$ .

$$\oint_S \mathbf{F} \cdot d\mathbf{A} = \int_V (\nabla \cdot \mathbf{F}) dV \quad (2-5)$$

$$\nabla \cdot \mathbf{E} = \frac{\rho}{\epsilon_0} \quad (2-6)$$

Just as the electric field defines the force acting on a charge in space, the magnetic field defines the force experienced by a moving charge, or current. Magnetic fields differ from electric fields in that they require the movement of charges to be formed, and act only on moving charges or currents. The magnetic field produced by a steady current is given by the Biot-Savart law:

$$\mathbf{B} = \frac{\mu_0}{4\pi} \int \frac{\mathbf{I} \times \hat{\mathbf{r}}}{r^2} dl = \frac{\mu_0 I}{4\pi} \int \frac{d\mathbf{l} \times \hat{\mathbf{r}}}{r^2} \quad (2-7)$$

where  $\mathbf{B}$  is the magnetic field of interest expressed in tesla (T),  $I$  is the current in amps (A),  $r$  is the magnitude of radial distance from the current element " $I d\mathbf{l}$ " in meters (m), and  $\hat{\mathbf{r}}$  its unit vector denoting the radial direction. The quantity  $\mu_0$  is the permeability of free space expressed in  $N/A^2$ , which like  $\epsilon_0$  for the electric field, defines the ability of the medium to permit or carry a magnetic field. In this formulation of the magnetic field we integrate along the path taken by the constant current  $I$ , i.e.  $d\mathbf{l}$ . It should be noted that the Biot-Savart law is expressed in terms of the vector cross

product of the current flow and radial unit vector, yielding a field that is perpendicular to both the current flow and radial direction. As was the case with the electric field equation 2-1, we can generalize by introducing a volume current density ( $\mathbf{J}$ ) as follows:

$$\mathbf{B} = \frac{\mu_0}{4\pi} \int \frac{\mathbf{J} \times \hat{\mathbf{r}}}{r^2} d\tau \quad (2-8)$$

where we integrate over the volume  $d\tau$  containing the steady current density  $\mathbf{J}$ . Equation 2-8 is similar to 2-2 in that it states that the magnetic field at a point is the linear superposition of the magnetic fields produced by a collection of constant currents. Let us now investigate the divergence and curl of the magnetic field defined by the Biot-Savart law to obtain relations similar to Gauss's law in differential form (equation 2-6). Taking the divergence of the generalized Biot-Savart law we get:

$$\nabla \cdot \mathbf{B} = \frac{\mu_0}{4\pi} \int \nabla \cdot \frac{\mathbf{J} \times \hat{\mathbf{r}}}{r^2} d\tau = 0 \quad (2-9)$$

By using vector product rules for  $\nabla \cdot (\mathbf{J} \times \frac{\hat{\mathbf{r}}}{r^2})$  and noting that  $(\nabla \times \mathbf{J}) = \nabla \times (\frac{\hat{\mathbf{r}}}{r^2}) = 0$  we arrive at our result, another Maxwell equation. Physically we can draw parallels between equations 2-6 and 2-9. Evidently there is no magnetic charge analogue to electric charge, that is, there are no magnetic monopoles. Taking the curl of the generalized Biot-Savart law we get:

$$\nabla \times \mathbf{B} = \frac{\mu_0}{4\pi} \int \nabla \times \left( \frac{\mathbf{J} \times \hat{\mathbf{r}}}{r^2} \right) d\tau = \mu_0 \mathbf{J} \quad (2-10)$$

Again using vector product rules for  $\nabla \times (\mathbf{J} \times \frac{\hat{\mathbf{r}}}{r^2})$  and noting that  $\mathbf{J}$  derivatives go to zero, and  $\nabla \cdot \frac{\hat{\mathbf{r}}}{r^2} = 4\pi\delta^3(r)$  where  $\delta^3(r)$  is the three dimensional delta function we arrive at our result. This is known as Ampere's law in differential form, and is another of the Maxwell equations governing electricity and magnetism. To convert the differential form of Ampere's law seen in

equation 2-10 to the integral form seen in equation 2-12, we integrate equation 2-10 over a surface defined by  $\int d\mathbf{A}$  and apply Stoke's theorem (equation 2-11). Stoke's theorem states that the integral of the curl of a vector field  $\mathbf{F}$  over some surface  $S$  can be written as the line integral of the vector field over the line bounding the surface  $S$ .

$$\int_S (\nabla \times \mathbf{F}) \cdot d\mathbf{S} = \oint \mathbf{F} \cdot d\mathbf{l} \quad (2-11)$$

$$\int (\nabla \times \mathbf{B}) \cdot d\mathbf{A} = \oint \mathbf{B} \cdot d\mathbf{l} = \int \mu_0 \mathbf{J} \cdot d\mathbf{A} = \mu_0 I_{encl} \quad (2-12)$$

The integral form of Ampere's law is useful in that it states the magnetic field around a loop of current is defined completely by the diameter of the loop and the total current enclosed in the loop,  $I_{encl}$ .

The final additions to the Maxwell equations deviate from the electrostatics and magneto-statics presented to this point. These additions concern time-varying electric and magnetic fields,  $\frac{\partial \mathbf{E}}{\partial t}$  and  $\frac{\partial \mathbf{B}}{\partial t}$ . Vigorous derivation of the remaining equation, and amendment of an existing equation will be omitted, but can be found in both relevant texts<sup>4, 5</sup>. The following are the complete set of Maxwell's equations governing electromagnetism in differential form:

$$\nabla \cdot \mathbf{E} = \frac{\rho}{\epsilon_0} \quad (2-13)$$

$$\nabla \times \mathbf{E} = -\frac{\partial \mathbf{B}}{\partial t} \quad (2-14)$$

$$\nabla \cdot \mathbf{B} = 0 \quad (2-15)$$

$$\nabla \times \mathbf{B} = \mu_0 \mathbf{J} + \mu_0 \epsilon_0 \frac{\partial \mathbf{E}}{\partial t} \quad (2-16)$$

The final equation (2-14), known as Faraday's law, and the time derivative amendment to Ampere's law (2-16) are the only further additions to Maxwell's equations. These addendums show that time varying electric fields can generate magnetic fields, and vice versa. While this is a central axiom in electromagnetic theory, work presented in this thesis will hinge on results of static magnetic fields interacting with moving charges, and time varying fields will not be further relevant.

## 2.2 Lorentz Force

The previous section attempted to elucidate electric and magnetic fields, and brought together a collection of equations governing these fields known as the Maxwell equations. These fields are abstract concepts in that they are not tangible, nor are they forces, but they can define the force which acts on an electric charge. This is analogous to a gravitational field, in that the field will define the forces on energy and mass, but the field itself is not tangible, nor a force itself. Ultimately, the forces acting on charges and their resulting directional deviations will be of interest, not the strength of the electromagnetic field. We must therefore move past the fields themselves, and investigate the forces these fields apply to charged particles. The electric force (equation 2-17) and magnetic force (2-18) are functions of the associated field strength, magnitude of electric charge  $Q$  being acted upon, and, in the case of the magnetic field, the velocity  $v$  of the charge<sup>4, 5</sup>.

$$\mathbf{F} = E\mathbf{Q} \quad (2-17)$$

$$\mathbf{F} = Q(\mathbf{v} \times \mathbf{B}) \quad (2-18)$$

The electric and magnetic forces both act linearly with the charge  $Q$ , but in different directions, and under different circumstances. The electric force acts directly along the electric field line, where the magnetic force acts perpendicular to the velocity of the charge and the magnetic field line. Furthermore, as a result of the cross product of velocity and magnetic field, the magnetic force acts only upon moving charges, where the electric field acts on all charges regardless of velocity. The linear combination of these forces describes the total force on a charge  $Q$  by the electromagnetic fields present, this force is known as the Lorentz force, and is defined as follows<sup>4, 5</sup>:

$$\mathbf{F} = Q(\mathbf{E} + \mathbf{v} \times \mathbf{B}) \quad (2-19)$$

### 2.3 Hall Effect

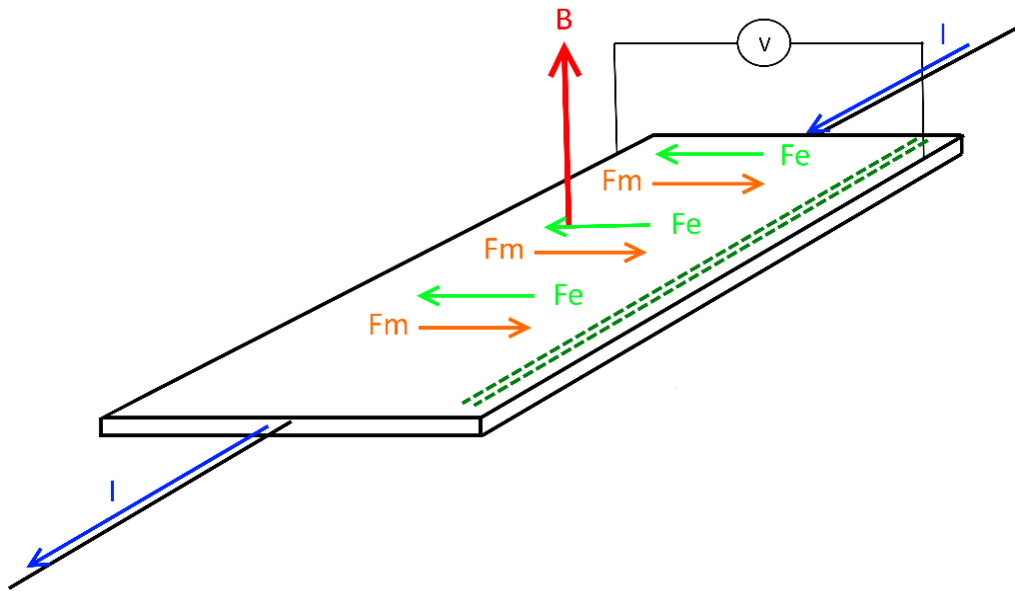


Figure 2.1 Schematic of the Hall Effect. The direction of current flow  $I$  is shown in blue, the magnetic field  $B$  is shown in red, electric and magnetic forces on electrons are shown in light green and orange respectively, and the charge buildup is represented by the dark green dashed lines. The voltmeter used to measure the electric potential is placed as shown by the "V" in the schematic.

Measurements of the energy deposited by x-ray photons made with a multitude of radiation detectors within magnetic fields of various strengths are to be investigated in this work. To facilitate the measurement techniques, and to understand the influence of static magnetic fields on the energy deposition by moving electric charges, the magnetic field at a point of measurement must be accurately known in order to define the magnetic field dose response. The measurement of the magnetic field will be conducted with the use of a Hall probe, which exploits the Hall Effect<sup>6, 7</sup> in quantifying the magnetic field strength. The Hall Effect is outlined in figure 2.1, where a current  $I$  flows through a thin conducting plate in the presence of an orthogonal magnetic field  $B$ . The magnetic force ( $F_m$ ) on the electrons composing the current directs them to one of the plate peripheries, where they build up a static charge represented by the dashed dark green lines in figure 2.1<sup>6</sup>. This static charge buildup at the periphery causes the formation of an electric field which generates an electric force on the electrons ( $F_e$ ) opposing the magnetic force. When the magnetic and electric forces experienced by the electrons are equal the charge buildup ceases and current flows as if there were no magnetic fields, this is known as the steady state of the system. The charge buildup can be measured by a voltmeter as shown in figure 2.1, where the charge buildup is proportional to the magnetic field strength orthogonal to the plate<sup>7</sup>. Three dimensional hall probes can be made by combining three of the one-dimensional plates in figure 2.1 into a mutually orthogonal position. The voltage across each of the plates can be related to a magnetic field strength in each of the three orthogonal directions. These individual fields can be added in quadrature to obtain the total magnitude field from the individual components.

## 2.4 Radiation in Matter

In order to study the dose response of various detectors in magnetic fields, the Monte Carlo Code PENELOPE<sup>8, 9</sup> will be employed to model the deposition of energy by the incident photons within a magnetic field. To facilitate the study of the Monte Carlo process, the mechanisms by which the photon radiation will interact within the medium must first be explored. There are three primary processes by which photons will interact within a given medium and transfer energy to the constituent electrons: photoelectric effect, Compton effect, and pair production<sup>1, 2</sup>. The interaction cross sections, together with the density of the medium, characterise the probability per unit length that a particular particle interaction will take place. The cross sections for the photoelectric effect, Compton effect, and pair production are represented in figure 2.2 by  $\tau$ ,  $\sigma$ , and  $\kappa$  respectively, and vary in magnitude with both the photon energy and the atomic number ( $Z$ ) of the medium.

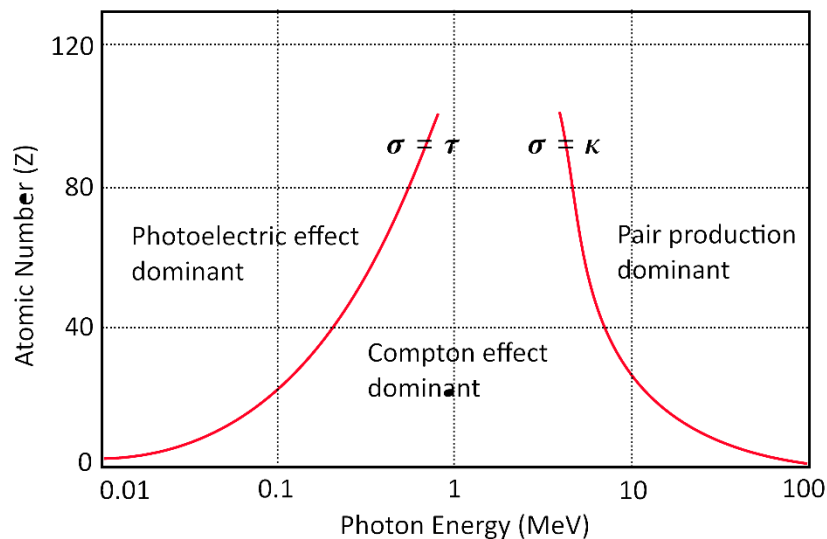


Figure 2.2 Domains of interaction dominance for photoelectric ( $\tau$ ), Compton ( $\sigma$ ), and pair production ( $\kappa$ ) as a function of photon energy and atomic number ( $Z$ ) of the medium.

The dependencies of the interaction cross sections on these quantities differ for each interaction process, and as such there are regions of photon energy and atomic number of the medium where each effect dominates, as shown

in figure 2.2<sup>1, 2</sup>. Each of these three primary photon interactions will be detailed in greater depth in subsections 2.4.1-2.4.3, and the resultant energy deposition, or dose, and charged particle behaviour will be detailed in subsection 2.4.4.

## 2.4.1 Photoelectric Effect

The photoelectric effect (figure 2.3) defines an interaction between a photon and a bound electron in which the photon transfers the entirety of its energy to the electron; as seen in figure 2.2 it is dominant for low photon energies and high atomic number media. In a photoelectric interaction, a photon of energy  $h\nu$  where  $h$  is Planck's constant and  $\nu$  the frequency of the photon - incident on an atomically bound electron with binding energy  $E_b$ , may transfer the entirety of its energy to the electron; this ionizes the atom and creates a free photoelectron of kinetic energy  $T_e = h\nu - E_b$ <sup>1, 2, 10</sup>. A photon requires an energy of at least  $E_b$  for the photoelectric effect to transpire, as it must overcome this binding energy to ionize the atom.

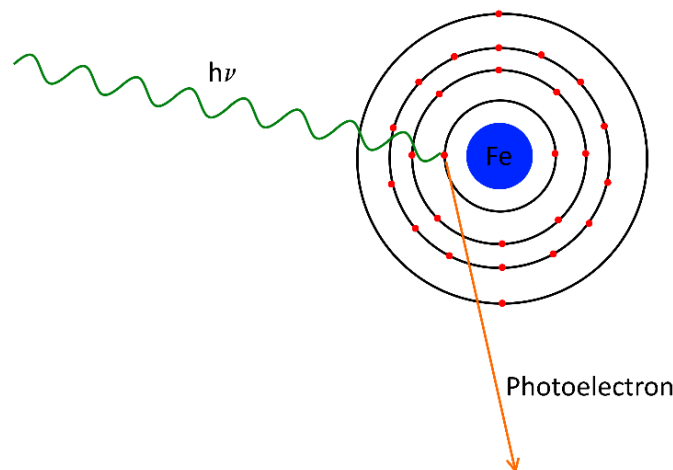


Figure 2.3 Illustration of the photoelectric effect. A photon of energy  $h\nu$  (shown in green) is incident on an iron atom (blue), transferring its energy to an electron (red) causing the atom to ionize. The photoelectron (orange) escapes with kinetic energy  $T_e = h\nu - E_b$ .

Atoms can consist of many electrons in orbitals, or shells, of differing binding energies<sup>10</sup> as can be seen for iron in figure 2.3. The incident photon may interact with any of these electrons provided it has the energy required to overcome the energy binding the electron to the atom. It is possible for low energy photons to have enough energy to ionize the outer shells of a particular atom, but not the inner shells. This leads to sharp discontinuities in the photoelectric cross section, seen in figure 2.4 for iron, at energies where additional electrons become available for photoelectric interactions<sup>1, 2, 10</sup>. The general form of the atomic interaction cross section for the photoelectric effect has the following proportionality to photon energy and atomic number of the medium<sup>1</sup>:

$$\tau \propto \frac{Z^4}{(h\nu)^3} \quad (2-20)$$

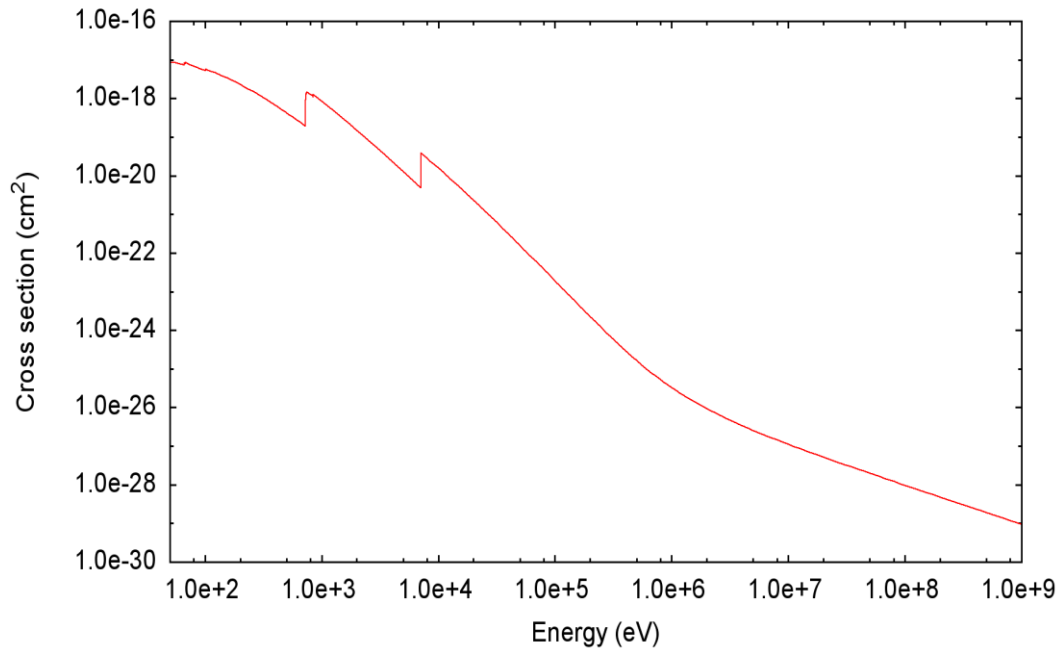


Figure 2.4 Photoelectric cross section of iron as a function of incident photon energy in electron volts (eV). Sharp discontinuous jumps are seen when photons have enough energy to ionize additional shells of the atom. Cross section data extracted from the PENELOPE code system<sup>9</sup>.

The ionization of an atom via the photoelectric effect leaves a vacancy in a shell, which can be filled by an electron in a higher energy shell. When an electron transitions from a higher energy shell to the vacancy in the lower energy shell, the excess energy is radiated away through x-rays<sup>1, 10</sup>. The energies of these so called “characteristic x-rays” will take discrete values defined by the energy difference between the initial and final shell of the electron transition. A contending method by which atoms release this excess energy is through the emission of Auger electrons, whereby the energy from an electron transition is imparted to a valence shell electron, ejecting it<sup>1, 2</sup>.

## 2.4.2 Compton Effect

A photon may scatter off an electron, transferring a portion of its energy in the process. This scattering is known as the Compton effect, and is depicted in figure 2.5.

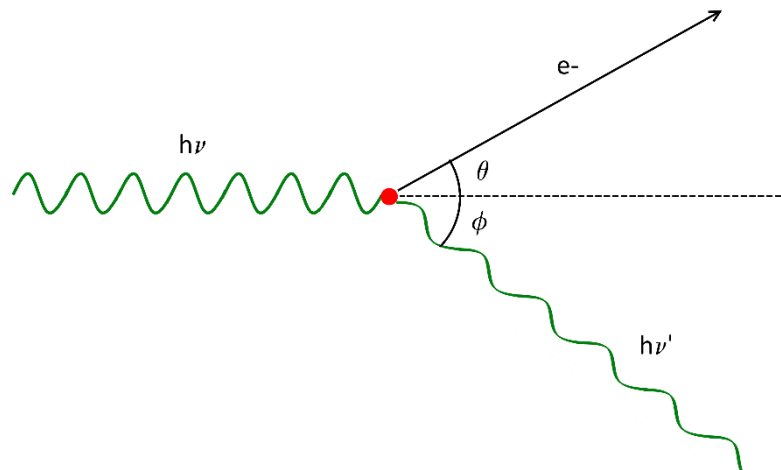


Figure 2.5 Illustration of the Compton effect. A photon with incident energy  $h\nu$  scatters off of a free electron. The photon scatters at angle  $\phi$  with energy  $h\nu'$ , and the electron scatters at angle  $\theta$  with energy  $h\nu - h\nu'$ .

The Compton effect differs from the photoelectric effect in that the photon retains some energy, as opposed to transferring the entirety of its energy to the electron<sup>1, 2</sup>. As seen in figure 2.2, this effect is dominant for the majority of radiotherapy situations<sup>1, 2, 11</sup>, and for the majority of materials under the 6 MV photon irradiation of the Linac-MR. In a Compton scattering interaction, a photon of incident energy  $h\nu$  interacts inelastically with an electron, partitioning the initial energy between the scattered photon and electron<sup>10</sup>. Invoking the conservation laws of energy (2-21) and momentum (2-22a and 2-22b) assuming a free electron, one can obtain the relations 2-23 a,b,c governing the interaction through simple algebra<sup>1</sup>:

$$h\nu + m_0c^2 = h\nu' + \sqrt{(m_0c^2 + p_e^2c^2)} \quad (2-21)$$

$$p_1 = p_2 + p_e \quad (2-22a)$$

$$p_e^2 = p_1^2 + p_2^2 - 2p_1p_2\cos(\theta) \quad (2-22b)$$

$$h\nu' = \frac{h\nu}{1 + \left(\frac{h\nu}{m_0c^2}\right)(1 - \cos\phi)} \quad (2-23a)$$

$$T_e = h\nu - h\nu' \quad (2-23b)$$

$$\cot\theta = \left(1 + \frac{h\nu}{m_0c^2}\right) \tan\left(\frac{\phi}{2}\right) \quad (2-23c)$$

Where  $h$  is plank's constant,  $\nu$  is the initial and  $\nu'$  the final photon frequency.  $T_e$  is the final electron kinetic energy,  $m_0$  is the electron rest mass,  $c$  the speed of light,  $\theta$  and  $\phi$  are the electron and photon scattering angles respectively, and  $p_1$  and  $p_2$  are the momenta of the photon before and after the collision ( $h\nu=p_1c$ ). It is evident that not only can a photon undergoing Compton scattering transfers a range of energies to the electron, but the energy transferred will define the scattering angles of the photon and the electron leaving the interaction site. However, these equations do not tell us

the probability of the Compton effect occurring, only the relationship between energy transferred and scattering angles.

The Klein-Nishina cross section, derived from quantum electrodynamics, defines the probability of the Compton effect occurring with a bound atomic electron<sup>1, 2</sup>, and is a function of scattering angle and initial photon energy. Presented in figure 2.6 is the total cross section for iron, integrated over all possible energy transfers, and thus over all scattering angles, defining the probability of a Compton effect occurring for a given photon energy irrespective of the kinematics of the interaction. The general form of the atomic interaction cross section for the Compton effect has the following proportionality to photon energy and atomic number of the medium<sup>1</sup>:

$$\sigma \propto \frac{Z}{h\nu} \quad (2-24)$$

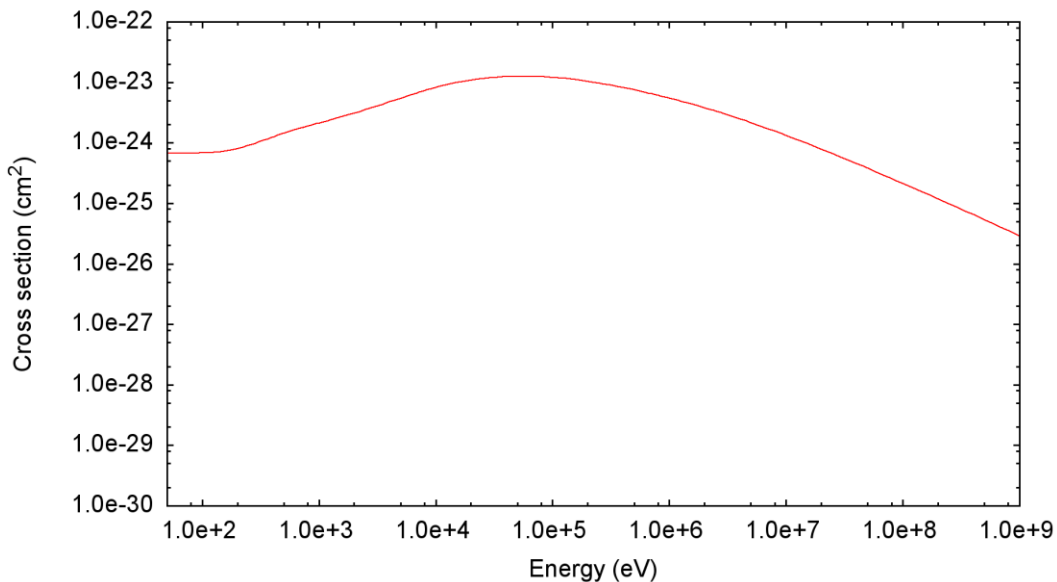


Figure 2.6 Compton cross section of iron as a function of incident photon energy in electron volts (eV). Cross section data extracted from the PENELOPE code system<sup>9</sup>.

### 2.4.3 Pair Production

The final primary interaction of interest for photons in a medium is pair production. This final interaction is dominant for high energy photons and in

high atomic number materials, as seen in figure 2.2. Pair production involves the creation of an electron, and its antimatter counterpart, the positron; which is analogous to a positively charged electron<sup>1, 2, 10</sup>. As seen in figure 2.7, a photon of incident energy  $h\nu$  interacts with the coulomb field of an atom – iron in the figure – and splits into an electron and positron pair, which leave at angles  $\xi$  and  $\zeta$ . In order to adhere to the conservation of energy in the creation of the rest masses of the positron and electron, a

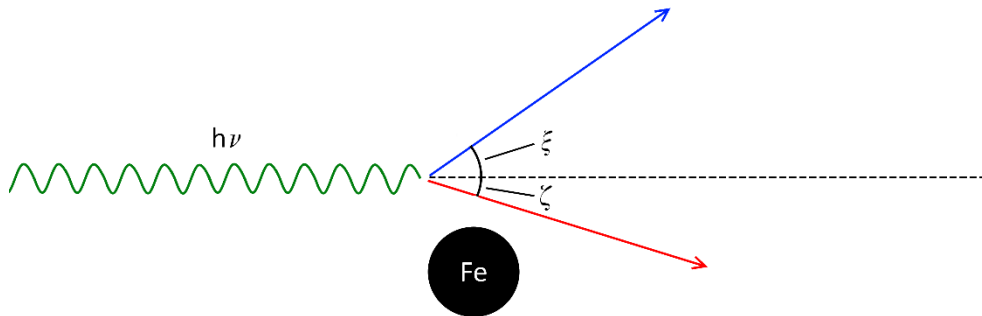


Figure 2.7 Illustration of pair production. A photon in the presence of the Coulomb field of an atom splits into a positron-electron pair.

photon is required to have a minimum energy of  $2m_0c^2$ , or 1.022 MeV. The positron and electron each leave with a range of possible energies which depend on the energy given to the other particle, but are not necessarily equal. Momentum is conserved by accounting for the vanishingly small kinetic energy given to the atom<sup>1, 2</sup>.

The pair production atomic cross section has the following dependence on the energy of the photon and atomic number of the medium<sup>1</sup>:

$$\kappa \propto Z \ln(h\nu) \quad (2-25)$$

There is a significant dependence on  $z$ , and a weak dependence on the energy which,  $h\nu$ , of the photon. The total cross section of the pair production interaction, that is the cross section integrated over all scattering angles and energies of the positron and electron, is presented in figure 2.8, and represents the probability of a pair production event occurring for a

given photon energy. Of importance is the sharp cutoff in the cross section at the threshold of interaction at 1.022 MeV.

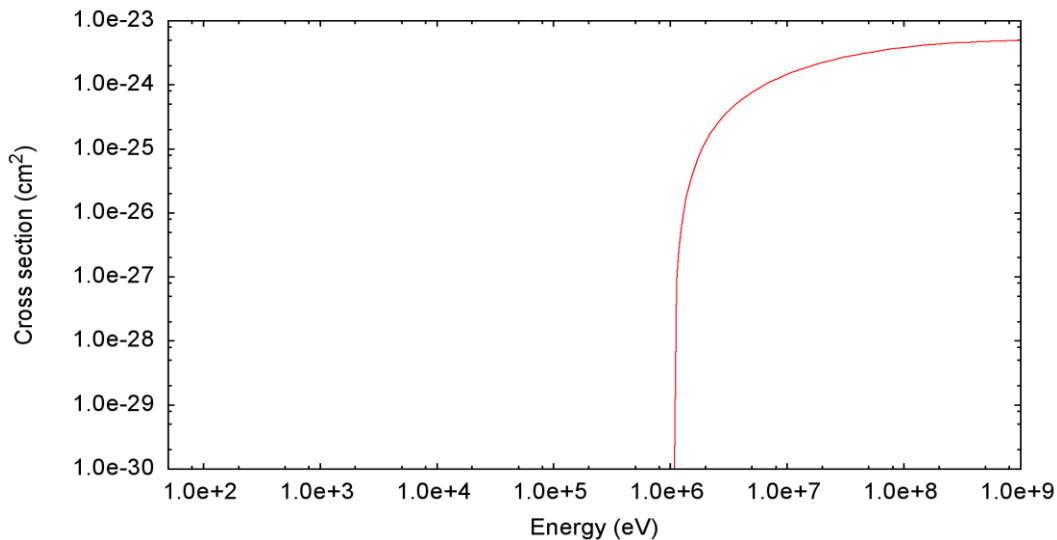


Figure 2.8 Pair production cross section of iron as a function of incident photon energy in electron volts (eV). Cross section data extracted from the PENELOPE code system<sup>9</sup>.

## 2.4.4 Kerma and Dose

The individual contributions to the total photon interaction cross section as a function of photon energy are shown for iron in figure 2.9. The regions where each interaction is dominant can be clearly observed, as the total interaction cross section is nearly in line with the dominant interaction cross section when not at transitional energies. The total kinetic energy released to the medium by the incident photon interactions is known as Kerma (Kinetic Energy Released per unit Mass)<sup>1, 2</sup>. The kerma,  $K$ , can be broken into two parts, the collisional,  $K_c$ , and the radiative kerma,  $K_r$ ; specifically, these are the kinetic energy per unit mass released that will ultimately be transferred to the medium downstream via collisions of charge particles, and the kinetic energy per unit mass that will be radiated away by charged particle interactions that create photons.

$$K = K_r + K_c \quad (2-26)$$

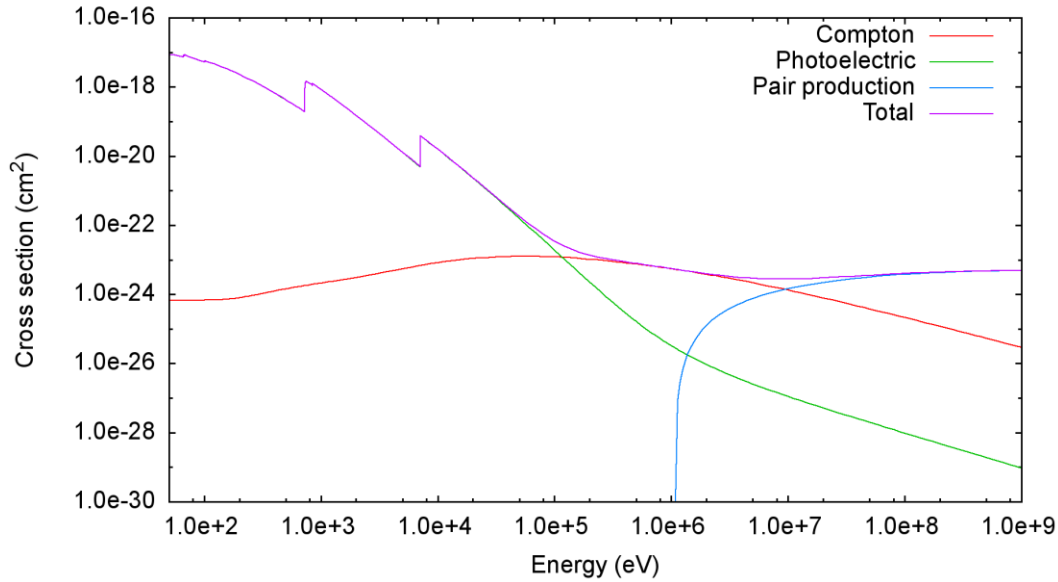


Figure 2.9 Total, photoelectric, Compton, and pair production cross sections of iron as a function of incident photon energy in electron volts (eV). Cross section data extracted from the PENELOPE code system<sup>9</sup>.

The energy deposited by the electrons set in motion by photons interactions per unit mass is known as the dose<sup>1,2</sup>. The dose,  $D$ , deposited in a medium is related to the collisional kerma, but is only equated to the collisional kerma in certain conditions.

Charged particle equilibrium (CPE) is said to exist at a point when the number of charged particles of each type and energy that enter a region equal the number leaving the region<sup>1,2</sup>, and this is the case for point B in figure 2.10. CPE does not exist when there is a disequilibrium in charged particle flow, such as in the charged particle buildup region (point A in figure 2.10). When CPE exists the collisional energy transferred to the medium by the incident photons ( $K_c$ ) at that point is the same as the energy deposited at that point from the upstream charged particles, and the dose deposited is equal to the collisional kerma<sup>1,2</sup>.

$$CPE \quad (2-27)$$

$$D = K_c$$

It should be noted that when CPE exists in a medium, the incident photon beam has necessarily been attenuated, and the  $K_c$  at this point will hence

be smaller in magnitude than it was upstream. The mechanisms of charged particle energy deposition (dose) are detailed below.

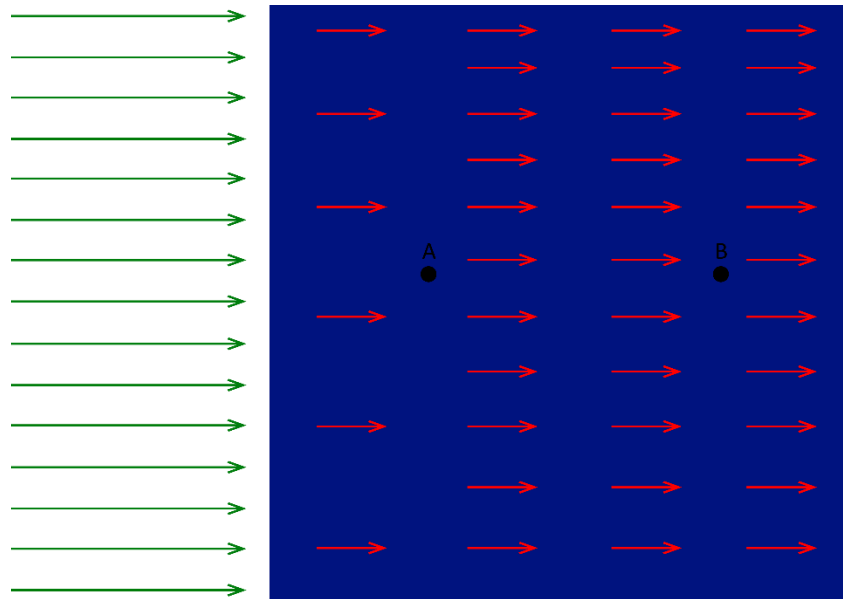


Figure 2.10 Illustration of charged particle equilibrium (CPE). Incident photons (green) interact with the medium (blue) and transfer kinetic energy to electrons (red). CPE does not exist at point A since fewer electrons enter that region than leave. CPE exists at point B because the electrons entering and leaving the region are equal.

As seen in the previous sections, when the incident photons undergo one of the three primary interactions within the medium, they create free, energetic electrons (and positrons) that propagate onwards from the interaction site. The positron created in the pair production interaction will eventually interact with an electron in the medium, and will annihilate one another, releasing two photons, which may themselves interact with the medium creating additional free electrons<sup>1, 2, 10</sup>. These electrons and positrons proceed to transfer energy via hard and soft (collisional), and radiative interactions with the atoms in the medium, and are in essence responsible for depositing the energy imparted to them by the photons; thus these charged particles are the dose carriers<sup>1, 2</sup>. Soft and hard interactions will deposit energy from the particles set in motion by the photons – known as secondary electrons – to atoms in the medium, leading to further ionization and the generation of further free electrons. The so called “soft” interactions interact with the atom as a whole, and transfer kinetic energy in

the eV range<sup>1, 2</sup>. These soft interactions are numerous, and over time will transfer a significant amount of energy to the medium. “Hard” charged particle interactions involve the interaction of a secondary particle with an individual atomic electron, and result in the transfer of significant kinetic energy. The ejected electron is known as a  $\delta$ -ray, which will dissipate its kinetic energy along a separate path<sup>1, 2</sup>. It is possible for secondary electrons to scatter elastically with atomic nuclei, drastically altering their direction, and yielding the “tortuous paths”<sup>1</sup> taken in the medium. Scattering with an atomic nucleus can also be inelastic, and results in the creation of a photon which radiates energy away (a radiative interaction). This radiation is known as bremsstrahlung, or braking radiation, so called because the electron loses energy and slows down in the creation of this radiation. Bremsstrahlung may ultimately leave the medium, thus carrying energy with it<sup>1</sup>.

The ability of the medium to retard charged particles through the receipt of their energy via all of these interactions is known as the stopping power. Shown in figure 2.11 as a function of energy for electrons in iron is the mass stopping power, which is simply the stopping power per unit length divided by the density of the material. This stopping power can be divided into the collisional (soft and hard interactions) and the radiative stopping power according to the interaction type involved in the energy loss. Stopping power defines the charged particle energy loss per unit distance travelled, and is a complicated function of particle’s energy, mass, and charge, as well as the medium’s atomic number, mean ionization energy, and density<sup>1, 2</sup>.

It has been previously shown that longitudinal magnetic fields – fields directed along the primary radiation direction – work to limit the lateral spread of electrons within a medium, and hence confine dose and sharpen the penumbra of the radiation field<sup>12-14</sup>. In the presence of lateral electronic equilibrium, transverse magnetic fields – those fields directed perpendicular to the primary radiation direction – show no dose alterations; however, when

equilibrium does not exist, such as at interfaces or the edges of the beam, dose deposition is shifted laterally, and the electron return effect comes into play as discussed in section 1.5<sup>15–18</sup>.

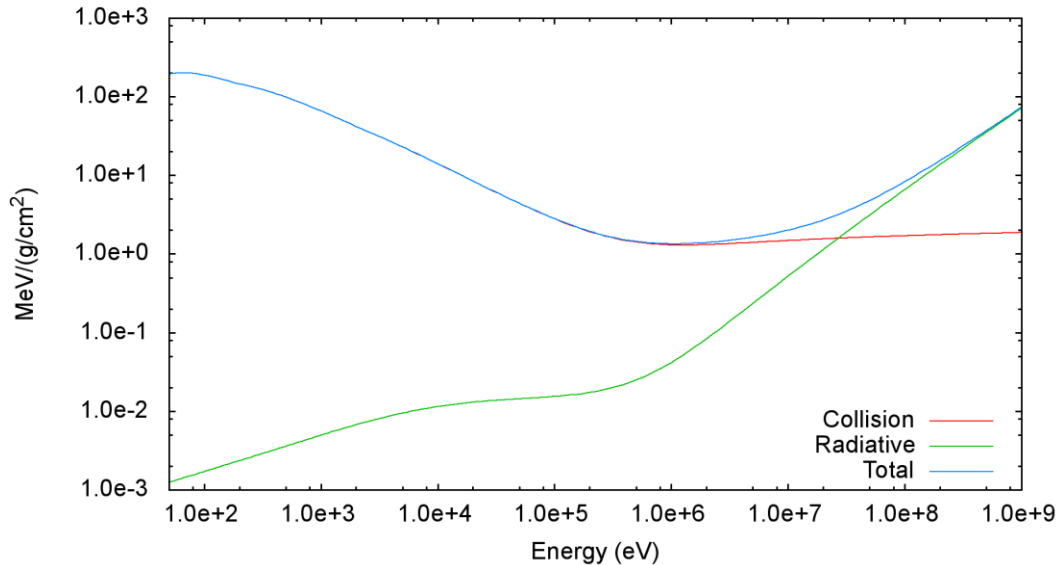


Figure 2.11 Total, radiative, and collisional stopping power of electrons in iron. Data extracted from the PENELOPE code system<sup>9</sup>.

## 2.5 Statistics and Random Sampling

To facilitate the understanding of the Monte Carlo process employed in this research, it is beneficial to first survey concepts in probability and random sampling, where random sampling simply refers to selecting random samples that obey a particular function or distribution. This section will introduce the concepts of probability density functions, cumulative distributions and their sampling, as well as expectation values of continuous distributions. These concepts will be directly applicable to the PENELOPE code system, and the Monte Carlo method in general<sup>8, 9</sup>.

The probability density function,  $p(x)$ , describes the chance that  $x$  will be found between  $x$  and  $x+dx$ <sup>9, 19</sup>. The integral of  $p(x)$  over all space is 1, meaning that  $x$  necessarily takes some value with non-zero probability

within  $p(x)$ , ( $p(x)$  is complete). It should be noted that  $p(x) \geq 0 \forall x$ , that is, the probability is always positive (or null); negative probabilities do not exist and have no meaning. Further, we can use the probability density function, or PDF, to define the  $n$ th order moment of  $p(x)$ <sup>9, 19</sup>:

$$\langle x^n \rangle \stackrel{\text{def}}{=} \int x^n p(x) dx \quad (2-28)$$

$\langle x^0 \rangle$  is the integral of the density function over all space, and is defined to be unity as before.  $\langle x^1 \rangle$ , when it exists, defines the expectation value of  $x$ , that is, the most likely value of  $x$  within the distribution  $p(x)$ . If the first and second order moments of the probability distribution function exist, we can define the variance of  $x$  as the second order moment about the mean, seen in equation 2-29<sup>9, 19</sup>.

$$\text{var}(x) \stackrel{\text{def}}{=} \langle (x - \langle x \rangle)^2 \rangle = \int (x - \langle x \rangle)^2 p(x) dx = \langle x^2 \rangle - \langle x \rangle^2 \quad (2-29)$$

The square root of the variance is known as the standard deviation of  $x$ ,  $\sigma = \sqrt{\text{var}(x)}$ , and gives a measure of the dispersion of  $x$  within the associated PDF<sup>9, 19</sup>. A larger standard deviation would signify a broad distribution with a wide range of values that are nearly equally likely, while a small standard deviation represented a more peaked distribution, where there are a few very likely values within the PDF. Higher order moments will not be discussed in detail, but can be used to further define properties of the probability distribution. For example, the third order moment about the mean can be used to define the skewness of the distribution, and the fourth order moment can be used to define what is known as the kurtosis, or peakedness of the distribution<sup>19</sup>.

The cumulative distribution function is used regularly in Monte Carlo, and is defined simply as the integral of the PDF of  $x$ <sup>9, 19</sup>:

$$P(x) \stackrel{\text{def}}{=} \int_{x_{\min}}^x p(x') dx' \quad (2-30)$$

$P(x)$ , the cumulative distribution function, increases continuously from 0 to 1 as  $x$  goes from the minimum to maximum value. This is the distribution function that we will be sampling from for the purposes of simulation.

In Monte Carlo simulations of radiation transport, we without fail encounter probability functions with variables of higher dimensionality<sup>9</sup>. In the case of a two dimensional variable, the joint PDF,  $p(x,y)$ , describes the chance that  $x$  and  $y$  will be found between  $x+dx$  and  $y+dy$ <sup>9, 19</sup>. As was the case for the uni-dimensional case, the probabilities are necessarily non-negative, and the integral of  $p(x,y)$  over all space is unity. Additionally, we can define what are known as the marginal PDFs  $q(x)$  and  $q(y)$ <sup>9, 19</sup>:

$$q(x) \stackrel{\text{def}}{=} \int p(x,y)dy \quad \text{and} \quad q(y) \stackrel{\text{def}}{=} \int p(x,y)dx \quad (2-31)$$

These marginal probability functions are the one dimensional projection of the two dimensional functions onto one of the variables;  $q(x)$  is the probability function associated with  $x$  given any value of  $y$ , and vice versa. The marginal probability density functions can be related to the original two dimensional probability density function through associated density functions known as the conditional PDFs  $p(x|y)$  and  $p(y|x)$ <sup>9, 19</sup>:

$$p(x,y) = q(x)p(y|x) = q(y)p(x|y) \quad \text{where} \quad p(y|x) = \frac{p(x,y)}{q(x)} \quad (2-32)$$

The conditional function  $p(x|y)$  is the probability density function of  $x$  for a fixed value of  $y$ , and its product with the associated marginal PDF yields the original two dimensional PDF. In this way two variable PDFs can be decomposed into a product of univariate PDFs. Likewise, multivariate PDFs can be decomposed in the same fashion yielding a single variable marginal PDF and an  $n-1$  dimensional conditional PDF, which can be further reduced by iteration of the same methods of decomposition<sup>19</sup>.

Monte Carlo calculations involve constant sampling of variables with specified PDFs, generally in the form of differential cross sections<sup>9</sup>. This sampling is accomplished by the generation of random numbers uniformly

distributed on the interval (0,1). However, since these numbers are generated through the use of a deterministic algorithm, they are not truly random<sup>9</sup>. Random number generators commonly used depend on the input of a “seed” parameter which will return a pseudo random number, which will alter the seed value for the generation of a further pseudo random number, and so on. These random number generators have a period, after which a pattern would emerge which could affect the integrity of the simulation relying on the random numbers generated. Fortunately, this period is very large, ranging from  $10^9$  –  $10^{18}$  depending on the generator<sup>9</sup>; this is practically inexhaustible in most present day cases.

The Monte Carlo code to be employed, PENELOPE, uses an inverse transform method of sampling from a PDF<sup>9</sup>. This method of sampling employs the cumulative distribution function  $P(x)$  to associate a random number  $R$ , in the range (0,1), to a variable  $x$  distributed by  $p(x)$ <sup>9, 19</sup>. We first define  $P(x)=R$ :

$$P(x) = R = \int_{x_{min}}^x p(x')dx' \quad (2-33)$$

We now have a random number which defines a point on the cumulative distribution. The point on the cumulative distribution function is necessarily unique due to the single valued nature of the function<sup>9, 19</sup>. Upon the inversion of 2-33, we find that our random variable of interest is:

$$x = P^{-1}(R) \quad (2-34)$$

Equation 2-34 is referred to as the sampling equation for  $x$ . This  $x$  is unique, randomly distributed in  $(x_{min}, x_{max})$  according to the PDF  $p(x)$ , and its randomness, or non-coherence in sampling, is determined by that of  $R$ <sup>9, 19</sup>. Figure 2.12 is a graphical illustration of the inverse transform method using  $R$  and  $P(x)$ , derived from  $p(x)$ , to find a unique  $x$  value. It is straightforward to see graphically that the region of greatest slope on the cumulative distribution function covers the most random numbers,  $R$ , and corresponds

to the region on greatest probability of a particular value of  $x$ , hence  $x$  will be distributed according to  $p(x)$ .

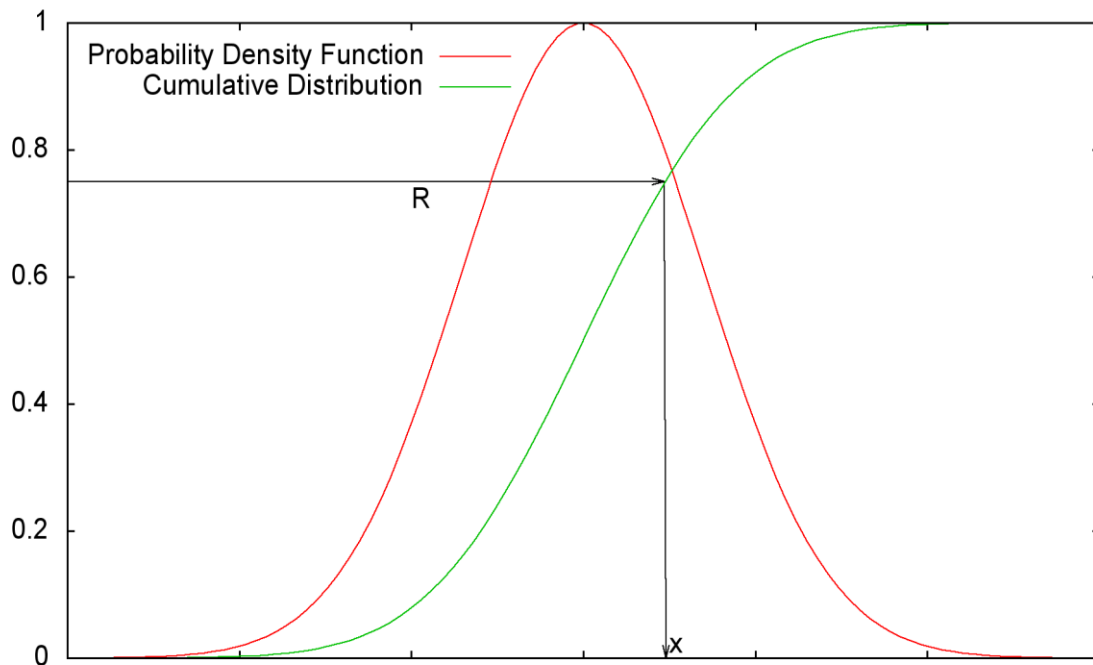


Figure 2.12 Inverse transform sampling of  $x$ , using a random number  $R$  and the cumulative distribution (green) of a probability density function (red) of  $x$ .

The inverse transform method can be used to sample from analytical functions (where its inverse function is also analytic), or from distributions that are too complicated to be sampled analytically<sup>9, 19</sup>. Sampling from distributions, without an analytic inverse function, would involve tabulating the cumulative distribution function,  $P(x)$ , at points  $x_i$  on a grid. The sampling equation can then be solved by inverse interpolation from the table  $(R_i, x_i)$ , where  $R = P(x)$ <sup>19</sup>. Caution must be exercised both when calculating the numerical integration of  $p(x)$  to obtain  $P(x)$ , and interpolating within the table  $(R_i, x_i)$  to ensure that errors introduced this way can be minimized. PENELOPE uses a cubic spline interpolation<sup>9</sup> between densely packed points to help mitigate errors.

As shown before, multivariate PDFs can be expressed as a product of a single variable marginal PDF and associated conditional PDF. Thus, in the case where we must sample from a bivariate PDF  $p(x, y)$ , we can first

sample  $x$  from the marginal distribution  $q(x)$ , and then  $y$  from the associated conditional distribution  $p(y|x)$ , and no new sampling techniques are required<sup>9, 19</sup>.

## 2.6 Monte Carlo Techniques for Radiation Transport

We will now apply the theory defined in the previous sections to the Monte Carlo simulation of radiation transport to be used in this work. Monte Carlo is a method of simulating radiation transport in matter which employs random numbers to sample from distributions governing the possible interactions. This simulated radiation transport will, for a large number of particles, approximate the actual radiation transport observed in the medium. This section will detail the mechanisms used specifically by the Monte Carlo code PENELOPE (Penetration and ENERGY Loss Of Positrons and Electrons) in sufficient detail for the reader to have a working knowledge of the processes involved. Unless otherwise stated, it can be assumed that the discussion below will follow that outlined in the PENELOPE user manual<sup>9</sup>, where an expatiated approach is undertaken.

Radiation transport is a stochastic process governed by the differential cross sections of the relevant interactions. Each possible interaction in the medium (Compton scattering, pair production, bremsstrahlung, etc...) has an associated differential cross section (DCS) varying with energy deposition and recoil angle of the incident particle, which acts as the PDF for the interaction. The integral over all possible deflection angles,  $d\Omega$ , and energy losses,  $dW$  (up to  $E_{max}$ ), yields the cross section for a specific interaction,  $\sigma_A$ , which is representative of the probability for interaction A occurring.

$$\sigma_A = \int_0^{E_{max}} \left( \int \frac{d^2\sigma_A}{d\Omega dW} d\Omega \right) dW \quad (2-35)$$

When a particle can undergo interactions A,B,C... within a medium, the individual interaction cross sections can be combined to yield a total interaction cross section, representing the probability of any interaction occurring. Radiation transport in the medium is completely specified by these individual cross sections for mechanisms A,B,C..., and thus the combined cross section for all interactions. The total interaction cross section is given by the sum of the individual cross sections:

$$\sigma_T = \sigma_A + \sigma_B + \sigma_C + \dots \quad (2-36)$$

We can also note that the cross sections are independent of the azimuthal scattering angle, and we are thus left to consider individual cross sections of the following form:

$$\sigma_{A,B,C\dots} = \int_0^{E_{max}} dW \int_0^\pi 2\pi \sin\theta d\theta \frac{d^2\sigma_{A,B,C\dots}(\theta, W)}{d\Omega dW} \quad (2-37)$$

This form contains only the polar scattering angle and energy deposition, allowing us to apply an azimuthal scattering angle at a later time with a uniform distribution.

$$p(\varphi) = \frac{1}{2\pi} \quad (2-38)$$

The interaction cross sections can be used to define the mean free path,  $\lambda$ , of a particle. The mean free path for interaction A is the average distance a particle will travel in a medium between two interactions of type A; its inverse is the interaction probability per unit length.

$$\lambda_A = \frac{1}{N\sigma_a} = \langle s \rangle = \int_0^\infty sp(s)ds \quad (2-39)$$

Where N in expression 2-39 is the number density of interaction sites for the particle in question, and p(s) is the probability function associated with an interaction occurring after travelling a path of length s. Generalizing for all interactions, we use our total interaction cross section to define our total mean free path for an incident particle; this total mean free path is the average distance a particle will travel before an interaction of any type. The

inverse total mean free path is the sum of the individual inverse mean free paths for different interaction mechanisms, as seen below.

$$\lambda_T^{-1} = N\sigma_T = \lambda_A^{-1} + \lambda_B^{-1} + \lambda_C^{-1} + \dots = N(\sigma_A + \sigma_B + \sigma_C + \dots) \quad (2-40)$$

Using the total mean free path, the PDF of the path length  $s$  between interactions of any type within the medium becomes:

$$p(s) = \lambda_T^{-1} \exp(-s/\lambda_T) \quad (2-41)$$

The total path length PDF (equation 2-41) can be sampled via random numbers to yield a length, or step size, over which the incident particle will travel before an interaction occurs. When the particle does interact with the medium, the type of interaction it undergoes is random, and can be determined by random sampling from the relative probabilities ( $p_a$ ,  $p_b$ ,  $p_c$ , etc...) of each interaction type.

$$p_A = \frac{\sigma_A}{\sigma_T} \quad , \quad p_B = \frac{\sigma_B}{\sigma_T} \quad , \quad p_C = \frac{\sigma_C}{\sigma_T} \quad \dots \quad (2-42)$$

When an interaction is selected via this random sample, we can progress and sample the polar scattering angle and energy loss from the accompanying normalized differential cross section (equation 2-43) using the inverse transform method for 2D variables explored earlier.

$$p_{A,B,C\dots}(\theta, W) = \frac{2\pi \sin\theta}{\sigma_{A,B,C\dots}} \frac{d^2\sigma_{A,B,C\dots}(\theta, W)}{d\Omega dW} \quad (2-43)$$

The azimuthal scattering angle can then be determined via its uniform PDF (expression 2-38).

Subsequent to any particle interaction, there may be secondary particles created, which will be simulated in the same way before returning to the simulation of the initial primary particle. Because particle transport can be modelled as a Markov process (future events are statistically determined by present events, depending only on the event immediately preceding<sup>20</sup>), the simulation of an individual particle can be suspended to simulate additional particles as long as the states of all the particles “paused” are saved. The

Markovian nature of particle transport also allows us to stop the particle simulation at any interface where there is a change of materials; we can then continue the simulation with our new cross sectional data for the new material. In this way complicated geometries, if modelled correctly, can be easily simulated where the boundary conditions would yield great difficulties for analytic solutions.

Using the aforementioned techniques, the simulation flow is as follows: An incident particle begins its flight with an energy  $E$  and direction  $\mathbf{d}$ . The length of free flight,  $s$ , in the first material is determined by the total mean free path,  $\lambda_T$ . Using the inverse sampling method (equation 2-34) with random number  $\xi$ , we can sample the free flight distance travelled before an interaction occurs via the following sampling expression:

$$s = -\lambda_T \ln \xi \quad (2-44)$$

The type of interaction is then determined by the individual interaction probabilities defined previously ( $p_i = \sigma_i / \sigma_T$ ). The polar angle  $\theta$  and energy loss  $W$  are sampled from the PDF  $p_{A,B,C...}(\theta, W)$ , assuming initial energy  $E$ , using inverse sampling methods for 2D distributions. Finally, the azimuthal scattering angle  $\phi$  is sampled using the sampling formula  $\phi = 2\pi\xi$ , with  $\xi$  being a random number. The energy of the particle is shifted to  $E - W$ , and the direction  $\mathbf{d}$  undergoes a rotation through the polar and azimuthal scattering angles. The track continues to be simulated in this way until it leaves the system or a pre-set energy  $E_{abs}$  is reached, at which point it is absorbed and the remaining energy deposited in place. Each secondary particle created is also simulated in this fashion, using the appropriate cross sections for particle type and energy. Throughout this simulation, any quantities of interest, such as the spatial energy deposition, can be scored and tabulated.

At high energies with many photon histories, detailed simulation of radiation transport becomes impractical. The average angular deflection in each

secondary electron collision is small, as is the energy deposited; this means that each history will take longer to terminate, prolonging the initialization of further histories, leading to impractically long simulation times. To expedite the simulation we can consider mixed simulation procedures, in which hard electron collisions with large energy depositions and deflection angles ( $W > W_{min}, \theta > \theta_C$ ) are simulated as above, and soft collisions are modelled by means of a multiple scattering approach<sup>21-23</sup>.

The method used by PENELOPE for mixed simulations is known as the random hinge method. The random hinge method begins by specifying the mean free path between hard elastic events as follows:

$$\frac{1}{\lambda_{el}^h} = N2\pi \int_{W_{min}}^{E_{max}} dW \int_{\theta_C}^{\pi} \frac{d^2\sigma_{el}(\theta, W)}{d\Omega dW} \sin\theta d\theta \quad (2-45)$$

Where  $\lambda_{el}^h$  is the hard elastic mean free path, which is the mean free path considering only those events with energy depositions and deflections greater than some cutoff value ( $W_{min}, \theta_C$ ). The PDF for the step length and the sampling formula for the step length remain the same as before, but use  $\lambda_{el}^h$  as the mean free path.

The particle will move a total distance  $s$  between hard events as defined previously. All the soft interactions (those with  $W < W_{min}, \theta < \theta_C$ ) will be simulated as a single event yielding an average deflection of polar angle  $\chi$  along the track  $s$  at some point  $\tau$ , called the hinge point. The hinge point  $\tau$  is sampled uniformly in the interval  $(0, s)$ , and the polar deflection angle  $\chi$  is sampled from a distribution derived from multiple scattering theory<sup>22, 23</sup>. The soft events' combined energy loss  $\omega$  at the point  $\tau$  is sampled from a PDF that includes only soft inelastic collisions and soft bremsstrahlung interactions. After applying the deflection  $\chi$  and energy loss  $\omega$  at the hinge point, the particle will continue a distance  $s - \tau$  in the new direction. Note that, as before, the azimuthal angle is sampled uniformly. The simulation of the hard events at the terminal end of the path remains largely unchanged from

the detailed simulation above, with the exception of the lower limit of the DCS integrals (expression 2-37) to account for the minimum scattering angle and energy loss.

Before EM fields were added to PENELOPE, it was thoroughly benchmarked, which was a necessity to ensure the accuracy of the simulation, and validate the code system itself<sup>24</sup>. The code (without EM) was used to calculate the fractional backscattered and transmitted electrons (and their energy spectra) resulting from positron, electron, and photon beams of varying energies impinging on a multitude of different materials, and was found to agree closely to expected values<sup>24</sup>. Dose profiles in the depth direction within different materials with incident positrons, electrons, and photons of varying energies were also investigated, and again agreed closely with experimental findings<sup>24</sup>. Bremsstrahlung spectra for electrons of various energies within different materials were also compared, and found to agree to experimental findings<sup>24</sup>. These findings confirm the reliability of the code's interaction and particle tracking algorithms without a magnetic field.

Any electromagnetic fields introduced do not affect the cross sectional transport mechanics of the code system, only the charged particle trajectories. We must therefore ensure that the simulated trajectories agree with the analytically expected trajectories before PENELOPE can be used to model radiation transport in the presence of these fields. Specifically, magnetic fields will be employed in this work, so the accurateness of their implementation must be investigated. Within the PENELOPE code system, it is possible to simulate the flight paths of charged particles in the presence of EM fields in vacuum and score the paths taken in order to compare them to expected values. Figure 2.13 plots the trajectory, as simulated by PENELOPE, of an electron initially directed along the y axis with kinetic energy 10 MeV in the presence of a z-directed 1.25 T magnetic field. The analytically expected trajectory of the electron in this circumstance would

be a circle in the x-y plane with a radius of curvature of 2.67 cm, with no movement in the z direction. The analytic radius of curvature can be determined by  $r = \frac{\gamma m v}{q B}$ , where  $\gamma$  is the Lorentz factor,  $m$  is the particle mass,  $q$  the charge,  $B$  the magnetic field, and  $v$  the velocity component orthogonal to  $B$ . While the radius of curvature matches that expected (2.67 cm for both the analytic and simulated trajectories), we see a small drift in the simulated z position of the particle in figure 2.13, amounting to a non-physical z displacement of  $+3 \times 10^{-15}$  cm over the 100 cm trajectory simulated. This small drift is an artifact of the code system, and is on the order of tens of attometres, thus it is of little consequence practically in the simulation of radiation.

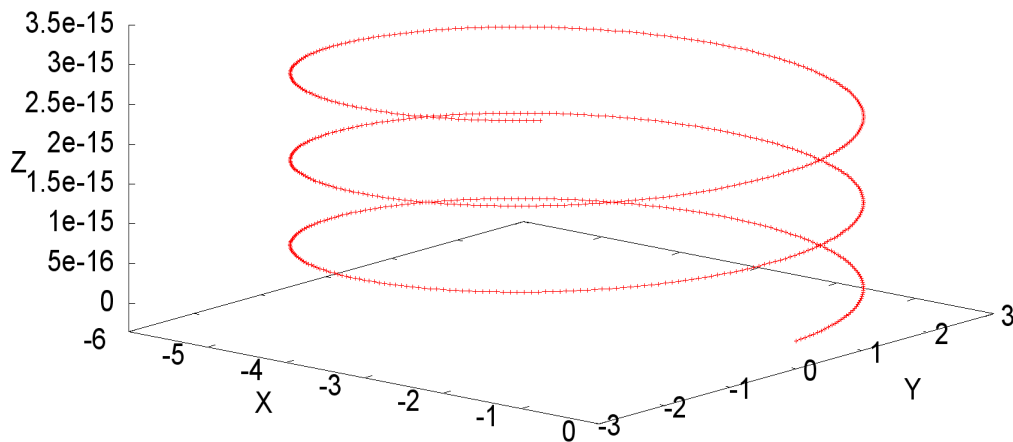


Figure 2.13 50 cm trajectory of a 10 MeV electron in a Z directed 1.25T magnetic field as simulated by the PENELOPE code system in vacuum9. All axes values are displayed in cm. Initial electron direction was along the y axis.

It is also possible to simulate slab style geometries of differing materials, and compare the dose profiles generated by the addition of magnetic fields to the expected values in literature, and other well benchmarked Monte Carlo codes<sup>15, 18, 24</sup>. Slab style geometries are simply slabs of varying thickness materials stacked on one another to create interfaces within the medium. These interfaces in particular are studied because they have been found to alter the dose deposition in the presence of magnetic fields<sup>12, 15, 18</sup>.

The results of these slab style geometries compare well to other Monte Carlo codes, and suggest that particle trajectories are accurately modelled by PENELOPE, as is dose deposition with the addition of EM fields. Not only do these results corroborate the correctness of charged particle transport with the addition of EM fields in PENELOPE, but since the particle interaction mechanics remain unchanged under the addition of EM fields, these results also ensure the correctness of the EM field implementation itself.

## **2.7 Adding Electromagnetism to Monte Carlo**

The interaction cross sections and the mean free path of a particle are independent of electromagnetic fields, and thus need not be modified when a field is introduced<sup>9</sup>. The Lorentz force, however, must be included in the simulation of radiation transport, as it will play a role in charged particle behaviour<sup>4, 5</sup>. This section will focus on the additions to the PENELOPE code system necessary for EM field implementation, namely the three subroutines, and the three step limiting parameters introduced.

In addition to accounting for the altered equations of motion in an electromagnetic field, three step length limiting parameters are introduced to ensure the accuracy of the simulation with the addition of EM fields. The parameters introduced are “uldv”, “ulde”, and “ulem”, which limit the deflection of a particle due to the EM field, the change in energy of a particle due to the EM field, and the change in the field itself between two interactions<sup>9</sup>. This step length limitation ensures that the processes involved are being sampled at a sufficient rate under the addition of EM fields, so as to mitigate errors in particle transport kinematics.

The subroutine “GETEMF”<sup>9</sup> is introduced to the PENELOPE code system in the presence of EM fields, and as its name suggests, it defines the EM field in space. The field this routine queries from can be provided in a

functional form, as a homogeneous distribution, or via a lookup table. The subroutine itself queries the current position of the particle, and returns the vector components of the electric and magnetic fields for use in further subroutines.

The subroutine “TPEMF0”<sup>9</sup> is added in EM field implementation, and takes the field strength output from “GETEMF” the new parameters “uldv”, “ulde”, and “ulem”, and determines the maximum step length of charged particles consistent with the given values. In other words, it takes “uldv”, “ulde”, “ulem”, and the EM field at a point as input values, and returns a maximum step length,  $s_{max}$ , between hard collisions that will maintain the “uldv”, “ulde”, and “ulem” limits, thus mitigating transport errors. Whenever the sampled step length between hard events is larger than  $s_{max}$ , the maximum step length is used instead, i.e.  $s = \text{minimum}\{-\lambda_{el}^h \ln \xi, s_{max}\}$ .

“TPEMF1”<sup>9</sup> is the final subroutine added to PENELOPE in order to facilitate the addition of EM fields to radiation transport. This subroutine is responsible for the generation of the charged particle trajectories through the application of the Lorentz force (equation 2-19). “TPEMF1” uses the current particle position, energy, direction, and EM field returned by “GETEMF” to determine the particle’s individual displacements due to inertia, electric force, and magnetic force over the transport length (i.e.  $s$ ), then combines the displacements linearly and applies them to the particle. Finally, the subroutine will determine the new direction cosines of the particle, and apply any required energy change to the particle at the end of particle transport in a linear fashion.

At this point in the simulation, the EM field effects – specifically, their deflections - have been fully accounted for, and the simulation of the particle will continue per section 2.6 unaffected. The mean free path, with the  $s_{max}$  adjustment due to EM fields, will be determined as previously. The hinge point  $\tau$ , and its associated energy loss and deflection, together with the hard inelastic event type after the full path  $s$  will also be determined as before.

The hard event energy loss and deflection will then be sampled from the relevant interaction DCS, and applied to the particle. To add EM field deflections, one must simply call the “TPEMF1” function before the deflection and energy loss due to any particle interaction in the medium is applied. The “TPEMF1” function will proceed to apply the required EM field deflections and energy changes, and the simulation will then apply the deflection and energy loss due to the radiation interaction.

## 2.8 Ionisation Chambers

Ionisation chambers are the gold standard for absolute dose measurements of clinical linear accelerators<sup>1, 2, 25</sup> by virtue of their calibration at standard laboratories. Not only will these kinds of detectors be studied in depth for their dose response in a magnetic field, but the TG-51 protocol pertaining to their use for dose measurements will be altered to account for the magnetic field of the Linac-MR<sup>25</sup>. It is therefore beneficial to have a basic understanding of ionisation chambers before we delve into their simulation in Monte Carlo.

Ionisation chambers measure the radiation incident on them by collecting the charges produced when the air inside the chamber is ionized, the ionization produced will be related to the dose deposited within the chamber<sup>1,2</sup>. The Bragg-Gray cavity theory defines the dose to a cavity of air within a medium given the following assumptions: the cavity is sufficiently small such that the photon and electron fluences are not changed by the presence of the cavity, and the dose deposited in the cavity is entirely from the charged particles crossing it (no charged particles are created in the cavity)<sup>1, 2</sup>. The dose to a cavity containing a small mass of air,  $D_g$ , is therefore defined as follows<sup>2</sup>:

$$D_g = \frac{Q}{m} \left( \frac{W}{e} \right)_g = \int dE \phi(E) \left( \frac{S(E)}{\rho} \right)_g \quad (2-46)$$

where Q is the charge produced in the cavity, m is the mass of the air in the cavity, (W/e) is the mean energy required to produce a unit of charge in the gas (33.97J/C for air),  $\phi(E)$  is the differential electron fluence as a function of the energy E, and  $(S(E)/\rho)$  is the mass collision stopping power. However, we are interested in the dose to the medium at this point, and due to the assumption that the fluence is not affected by the presence of the chamber, the dose to the medium at this point will be delivered by the same fluence of electrons. We can therefore relate the dose to air to the dose to the medium ( $D_{med}$ ) through the ratio of average energy depositions as defined below<sup>1, 2</sup>:

$$\frac{D_{med}}{D_g} = \frac{\int dE \phi(E) \left( \frac{S(E)}{\rho} \right)_{med}}{\int dE \phi(E) \left( \frac{S(E)}{\rho} \right)_g} = \bar{S}_g^{med}, D_{med} = \frac{Q}{m} \left( \frac{W}{e} \right)_g \bar{S}_g^{med} \quad (2-47)$$

Where  $\bar{S}_g^{med}$  is the ratio of the average stopping power integrals for the medium and gas given an electron fluence  $\phi(E)$ <sup>1, 2</sup>. We have substituted the initial  $D_g$  expression from 2-46 to yield the final  $D_{med}$  expression in 2-47.

This treatment neglects the presence of any wall surrounding the cavity, or assumes that the wall material is the same as the medium, hence neglecting any change in dose due to the presence of the wall. Bragg-Gray cavity theory assumes the fluence of photons remains unchanged in the presence of the cavity, however, the photon energy transferred in the wall may differ from that in the medium. This difference can be accounted for in a similar fashion as above by introducing the ratio of photon mass absorption coefficients of the medium and the wall  $\left( \frac{\mu_{en}}{\rho} \right)_{wall}^{med}$ <sup>1, 2</sup>. Where the photon mass absorption coefficient is simply the photon energy per unit mass traversed absorbed by the medium. This ratio will account for differences in photon energy deposition between the wall and the medium. We can use a modified expression 2-47 to relate the dose deposited in the air to that deposited in

the wall, which in turn is related to the photon energy deposition in the medium through the mass absorption ratio as follows<sup>1, 2</sup>.

$$D_{med} = \frac{Q}{m} \left( \frac{W}{e} \right)_g \left( \frac{\mu_{en}}{\rho} \right)_{wall}^{med} \bar{S}_g^{wall} \quad (2-48)$$

The main shortcoming of the Bragg-Gray theory is that it uses the continuously slowing down approximation (CSDA) fluence of electrons for the stopping power, and neglects the  $\delta$ -ray (electrons liberated in hard collisions by primary electrons slowing down) production, hence underestimating the low energy electron fluence<sup>1</sup>. Spencer and Attix corrected the Bragg-Gray theory to account for the  $\delta$ -rays; to do this the Spencer-Attix theory uses the mass restricted stopping power ( $\bar{L}_\Delta/\rho$ ), with the parameter  $\Delta$  denoting the energy at which the energy from  $\delta$ -rays is assumed to be absorbed locally<sup>1, 26</sup>. The restricted stopping power is related to the stopping power, and represents the total energy deposited by all those interactions releasing energy less than  $\Delta$ . If the energy deposited in a single interaction is more than  $\Delta$  then it is not assumed to be absorbed locally, and the particles carrying this energy must be added to the fluence of electrons  $\phi(E)$ . The parameter  $\Delta$  is associated with the track length of the  $\delta$  particles. The choice of this energy should be that at which the  $\delta$  particles just cross the chamber cavity, as those with larger ranges can be expected to carry their energy out of the chamber cavity<sup>1, 26</sup>. Using these new considerations, the ratio of doses to the medium and a gas is defined as below<sup>1, 26</sup>.

$$\frac{D_{med}}{D_g} = \left( \frac{\bar{L}_\Delta}{\rho} \right)_{wall}^{med} \left( \frac{\mu_{en}}{\rho} \right)_{wall}^{med} \quad (2-49)$$

$$\left(\frac{\overline{L_{\Delta}}}{\rho}\right)_g^{wall} = \frac{\int_{\Delta}^{E_{max}} \Phi(E) \left(\frac{\overline{L_{\Delta}}}{\rho}\right)_{wall} dE + \Phi(\Delta) \left(\frac{S(\Delta)}{\rho}\right)_{wall} \Delta}{\int_{\Delta}^{E_{max}} \Phi(E) \left(\frac{\overline{L_{\Delta}}}{\rho}\right)_g dE + \Phi(\Delta) \left(\frac{S(\Delta)}{\rho}\right)_g \Delta} \quad (2-50)$$

It should be noted that, as per Bragg-Gray theory, the stopping power integral in the above expressions is averaged over electron fluence arising from the CSDA for a monoenergetic source. This integral can be further averaged over the polyenergetic electrons arising from a monoenergetic photon source, and then again over the polyenergetic photon source<sup>1, 2</sup>. Generally, if the complete electron fluence is known at a point, one may simply use this fluence, rather than averaging over multiple spectra.

It is important to know the source of these factors which convert the charge collected in an ionisation chamber to dose, in order to ascertain any expected changes within a magnetic field. It is anticipated that the magnetic field will change these factors very little, affecting only the fluence of electrons within the chamber. All of the aforementioned ionisation chamber factors for conversion of charge collected to dose deposited at that point in the medium are included in a single chamber specific factor within the TG-51 formalism, discussed below<sup>25</sup>.

## 2.9 TG-51

The TG-51 protocol<sup>25</sup> outlines the clinically accepted methodology for the calibration and measurement of radiation beams using an ionization chamber. Although this protocol assumes zero magnetic field, it has been shown that a single chamber specific correction factor based on field strength and relative orientations of the chamber, radiation beam, and magnetic field is needed to account for any magnetic field effects in ionisation chambers<sup>27-29</sup>. The formalism itself is simple, with the dose deposited to a point in water of beam quality Q defined as follows<sup>25</sup>:

$$D_w^Q = M_{corr} k_Q N_{D,w}^{60Co} \quad (2-51)$$

Where  $M_{corr}$  is the corrected electrometer reading,  $k_Q$  is the quality conversion factor, and  $N_{D,w}^{60Co}$  is the chamber specific calibration factor for dose to water in a  $^{60}Co$  beam. Each chamber will be calibrated according to a  $^{60}Co$  beam, the calibration factor  $N_{D,w}^{60Co}$  converts a unit reading in the chamber in question to the dose to water at that point in the  $^{60}Co$  beam<sup>25</sup>. This factor is not affected by a magnetic field, as it is essentially a unit conversion factor.  $k_Q$  is a quality conversion factor, which converts the  $^{60}Co$  beam in which the chamber was calibrated to a beam of arbitrary quality  $Q$ ; this factor depends on the ratios of the restricted mass stopping powers, fluence corrections, and gradient corrections for a beam of quality  $Q$  to a  $^{60}Co$  beam<sup>25</sup>. The restricted mass stopping powers are functions of the electron differential cross sections and the fluence and gradient corrections correct for differences in the magnitude of electron fluence  $\phi(E)$  caused by the introduction of the ionisation chamber itself.  $M_{corr}$  includes various factors required to correct the raw reading of the electrometer, accounting for various effects including the standard temperature and pressure correction, polarity correction, and recombination correction<sup>25</sup>. Any magnetic field corrections can be implemented as a standalone chamber specific factor, or be included within  $M_{corr}$ .

## 2.10 Solid State Detectors

In addition to the ionisation style chambers, three varieties of solid state detectors will be evaluated for their dose response in the magnetic field of the Linac-MR. These detectors are the diamond detector, diode detector, and optically stimulated luminescence (OSL) detector. This section will briefly overview the operation of each of these three detectors.

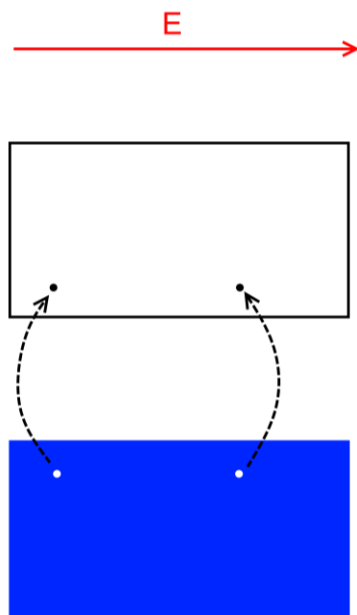


Figure 2.14 Electrons are excited from the valence band (blue) to the conduction band (white), where they are collected by an electric field.

Both diamond and diode exhibit a band gap structure, with forbidden gaps of  $\sim 5.5$  and  $\sim 1.1$  eV respectively<sup>1, 30, 31</sup>. Irradiation of the diamond and diode material excites electrons from the valence band to the conduction band forming electron-hole pairs<sup>30, 31</sup>. In each of these detectors an electric field collects the charges produced; the total charge collected can be related to the total energy (dose) deposited in the detection volume. The electric field in the diamond detector investigated (PTW 60003) is externally applied by 100 V in

potential. The electric field in the diode detector investigated (IBA PFD) is characteristic of the detector. The diode detector contains both p-type and n-type silicon, which have excess electron “holes” (acceptor sites) and electrons respectively<sup>1, 31</sup>. When these types of silicon are joined, they create a p-n junction. The excess electrons from the n-type silicon diffuse across the p-n junction to the acceptor sites in the p-type silicon. This creates a net positive charge in the n-region and net negative charge in the p-region close to the junction, creating an electric field that opposes the diffusion. The diffusive force on the electrons due to the concentration gradient is ultimately balanced by the force due to the newly established electric field, thus forming a static passive electric field at equilibrium<sup>31</sup>. Figure 2.14 illustrates the mechanism of radiation detection in diamond and diode detectors. OSLs have a similar band gap structure to the diamond and diode detectors, however, impurities in the OSL crystal create traps within the band gap where an electron can rest<sup>32</sup>. When OSLs are irradiated,

electrons are liberated and travel from the valence band to the conduction band; the electrons can then proceed to release energy and become trapped in the energy traps within the forbidden region of the OSL crystal, as seen in figure 2.15<sup>32</sup>. When the OSL crystal is exposed to optical photons sufficient in energy to excite the electrons from the traps, the trapped electrons escape, and may re-combine with the holes in the OSL lattice. This recombination emits optical photons which can be measured as the output; this output is proportional to the number of electrons trapped, and hence the total dose received<sup>32</sup>

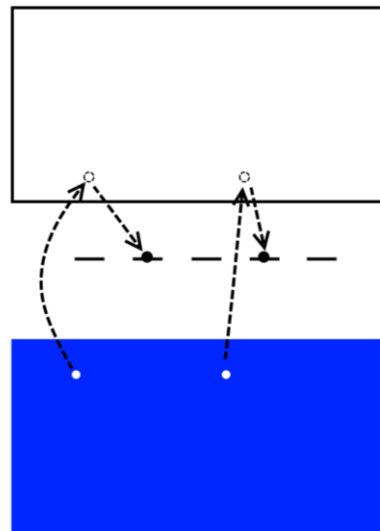


Figure 2.15 Electrons are excited from the valence band (blue) to the conduction band (white), before falling into the traps between the bands. These electrons can be excited at a later time, creating photons when they transition from the conduction band back to the valence band.

## 2.11 References

- 1 F. Attix, *Introduction to Radiological Physics and Radiation Dosimetry* (WILEY-VCH, Weinheim, 2004).
- 2 H.E. Johns and J.R. Cunningham, *The Physics of Radiology* (Charles C Thomas, Springfield, Illinois, 1983).
- 3 B.G. Fallone, M. Carlone, B. Murray, S. Rathee, T. Stanescu, S. Steciw, K. Wachowicz, and C. Kirkby, "Development of a Linac-MRI system for real-time ART," *Med. Phys.* **34**, 2547–2547 (2007).
- 4 D.J. Griffiths, *Introduction to Electrodynamics*, 3 Edition (Prentice Hall, Upper Saddle River, NJ, 1999).
- 5 J.D. Jackson, *Classical Electrodynamics*, 3 Edition (Wiley, New York, NY, 1999).
- 6 E.H. Hall, "On a new action of the magnet on electric currents," *Am. J. Math.* **2**(3), 287–292 (1879).
- 7 C.M. Hurd, *The Hall Effect in Metals and Alloys* (Plenum Press, New York, NY, 1972).
- 8 J. Baro, J. Sempau, J.M. Fernández-Varea, and F. Salvat, "PENELOPE: an algorithm for Monte Carlo simulation of the penetration and energy loss of electrons and positrons in matter," *Nucl. Instruments Methods Phys. Res.* (100), 31–46 (1995).
- 9 F. Salvat, J.M. Fernandez-Varea, and J. Sempau, *PENELOPE: A code system for Monte Carlo simulation of electron and photon transport* (2006).
- 10 P.A. Tipler and R.A. Llewellyn, *Modern Physics*, 4 Edition (W.H. Freeman and Company, New York, NY, 2003).
- 11 J. Bernier, E.J. Hall, and A. Giaccia, "Radiation oncology: a century of achievements.," *Nat. Rev. Cancer* **4**(9), 737–47 (2004).
- 12 C. Kirkby, B. Murray, S. Rathee, and B.G. Fallone, "Lung dosimetry in a linac-MRI radiotherapy unit with a longitudinal magnetic field," *Med. Phys.* **37**(9), 4722–4732 (2010).

- 13 A. Bielajew, "The effect of strong longitudinal magnetic fields on dose deposition from electron and photon beams," *Med. Phys.* **20**(4), 1171–1179 (1993).
- 14 Y. Chen, A.F. Bielajew, D.W. Litzenberg, J.M. Moran, and F.D. Becchetti, "Magnetic confinement of electron and photon radiotherapy dose: A Monte Carlo simulation with a nonuniform longitudinal magnetic field," *Med. Phys.* **32**(12), 3810 (2005).
- 15 A.J.E. Raaijmakers, MR-guided radiotherapy : magnetic field dose effects (Ph.D. Thesis, Utrecht University, 2008).
- 16 A.J.E. Raaijmakers, B.W. Raaymakers, and J.J.W. Lagendijk, "Integrating a MRI scanner with a 6 MV radiotherapy accelerator: dose increase at tissue-air interfaces in a lateral magnetic field due to returning electrons.," *Phys. Med. Biol.* **50**(7), 1363–76 (2005).
- 17 B.W. Raaymakers, A.J.E. Raaijmakers, a N.T.J. Kotte, D. Jette, and J.J.W. Lagendijk, "Integrating a MRI scanner with a 6 MV radiotherapy accelerator: dose deposition in a transverse magnetic field," *Phys. Med. Biol.* **49**(17), 4109–4118 (2004).
- 18 C. Kirkby, T. Stanescu, S. Rathee, M. Carlone, B. Murray, and B.G. Fallone, "Patient dosimetry for hybrid MRI-radiotherapy systems," *Med. Phys.* **35**(3), 1019–1027 (2008).
- 19 S.M. Ross, *Introduction to Probability Models*, 9 Edition (Elsevier, San Diego, CA, 2007).
- 20 K. Yosida, *Functional Analysis* (Springer-Verlag, 1968).
- 21 J. Baro, J. Sempau, J.M. Fernandez-Varea, and F. Salvat, "Simplified Monte Carlo simulation of elastic electron scattering in limited media," *Nucl. Instruments Methods Phys. Res. Sect. B Beam Interact. with Mater. Atoms* **84**, 465–483 (1994).
- 22 I. Kawrakow and A.F. Bielajew, "On the representation of electron multiple elastic-scattering distributions for Monte Carlo calculations," *Nucl. Instruments Methods Phys. Res. Sect. B Beam Interact. with Mater. Atoms* **134**(3-4), 325–336 (1998).
- 23 J.M. Fernández-Varea, R. Mayol, J. Baro, and F. Salvat, "On the theory and simulation of multiple elastic scattering of electrons," *Nucl. Instruments Methods Phys. Res. Sect. B Beam Interact. with Mater. Atoms* **73**, 447–473 (1993).

- 24 J. Sempau, J.M. Fernández-Varea, E. Acosta, and F. Salvat, "Experimental benchmarks of the Monte Carlo code penelope," Nucl. Instruments Methods Phys. Res. Sect. B Beam Interact. with Mater. Atoms **207**(2), 107–123 (2003).
- 25 P.R. Almond, P.J. Biggs, B.M. Coursey, W.F. Hanson, M.S. Huq, R. Nath, and D.W. Rogers, "AAPM's TG-51 protocol for clinical reference dosimetry of high-energy photon and electron beams.," Med. Phys. **26**(9), 1847–70 (1999).
- 26 D.J. La Russa and D.W.O. Rogers, "Accuracy of Spencer-Attix cavity theory and calculations of fluence correction factors for the air kerma formalism," Med. Phys. **36**(9), 4173 (2009).
- 27 I. Meijnsing, B.W. Raaymakers, A.J.E. Raaijmakers, J.G.M. Kok, L. Hogeweg, B. Liu, and J.J.W. Lagendijk, "Dosimetry for the MRI accelerator: the impact of a magnetic field on the response of a Farmer NE2571 ionization chamber.," Phys. Med. Biol. **54**(10), 2993–3002 (2009).
- 28 K. Smit, B. van Asselen, J.G.M. Kok, a H.L. Aalbers, J.J.W. Lagendijk, and B.W. Raaymakers, "Towards reference dosimetry for the MR-linac: magnetic field correction of the ionization chamber reading.," Phys. Med. Biol. **58**(17), 5945–57 (2013).
- 29 M. Reynolds, B. Fallone, and S. Rathee, "Dose response of selected ion chambers in applied homogeneous transverse and longitudinal magnetic fields," Med. Phys. **40**(4), 042102 (2013).
- 30 E. Barnett, Diamond Detector for IMRT Dosimetry (University of Alberta, 2004).
- 31 G. Shani, *Radiation Dosimetry Instrumentation and Methods*, 2 Edition (CRC Press, 2000).
- 32 L. Bøtter-Jensen, S.W.S. McKeever, and A.G. Wintle, *Optically Stimulated Luminescence Dosimetry* (Elsevier, Amsterdam, 2003).

## Chapter 3: Implementation

This chapter will provide specific details on the simulation and measurement methodologies implemented to accrue the results found in Chapter 4. Schematics and illustrations of the detectors and the orientations of interest will be presented alongside other parameters relevant to the simulation and measurement protocols employed. The information contained in this chapter is more than sufficient to repeat, and build upon the research data this work adds to dose measurement within an applied magnetic field environment, such as that within the Linac-MR.

### 3.1 Orientations of the Photon Beam, B Field, and Detector

There are four standard relative orientations of the photon beam, magnetic field, and radiation detectors' long axis that have been previously investigated<sup>1-3</sup>. These orientations are presented in figure 3.1. The long axis of the detector can be oriented either parallel (figures 3.1.I and 3.1.III) or perpendicular (figures 3.1.II and 3.1.IV) to the incident photons. The magnetic field strength is varied in this investigation, and its orientation can be either longitudinal with the photon beam (figures 3.1.III and 3.1.IV), or transverse to the photon beam (figures 3.1.I and 3.1.II). It should be noted that the magnetic field is also perpendicular to the long axis of the detector in orientations 3.1.I and 3.1.II. The electric field direction in the detectors does not change with respect to the detector long axis, and thus the relative orientation of electric and magnetic fields changes as we rotate the long axis through orientations I-IV. The electric field simply ensures that all the charges produced in the detector are collected; the charges in the simulation are assumed to be collected, and thus no electric field is required

in simulations. The average velocity of the charges produced in the detector which will eventually be collected is minimal; resultantly the magnetic force is far weaker than the electric force on these particles.

These permutations of orientation yield four cases to investigate. In fact, the solid state detectors investigated (PTW 60003 diamond and IBA PFD diode detectors) are asymmetric along the long axis of the detector (see figure 3.5 for detailed detector schematics), more specifically, the materials encountered in front, and behind the face of the cylindrical detector disc differ. This is in contrast to the relatively symmetric design of farmer chambers used in similar studies (see figures 3.2-3.4)<sup>1, 2</sup>. As a result, the two solid state detectors were additionally investigated under a 180 degree rotation of orientation II in the plane of the long axis of the detector. This geometry is referred to as orientation II-2 in this work. It should be noted that orientation IV does not require investigation under 180 degree rotation. This is because the majority of electrons are forward directed i.e. these electrons make a very small angle with respect to the magnetic field, and will be focused along the forward direction. Thus, the electron's trajectory as influenced by the magnetic field will remain relatively forward in direction, making changes in lateral electron fluence increasingly inconsequential with magnetic field strength.

One final unique orientation of magnetic field, chamber, and radiation beam orientation still exists. Where the long axis of the detector is parallel to the magnetic field, and both are perpendicular to the incident radiation beam. This orientation is not explicitly presented in figure 3.1, but it can be visualized by rotating the chamber in orientation II by 90° about the central axis of the beam. This final orientation will be referred to as orientation V henceforth.

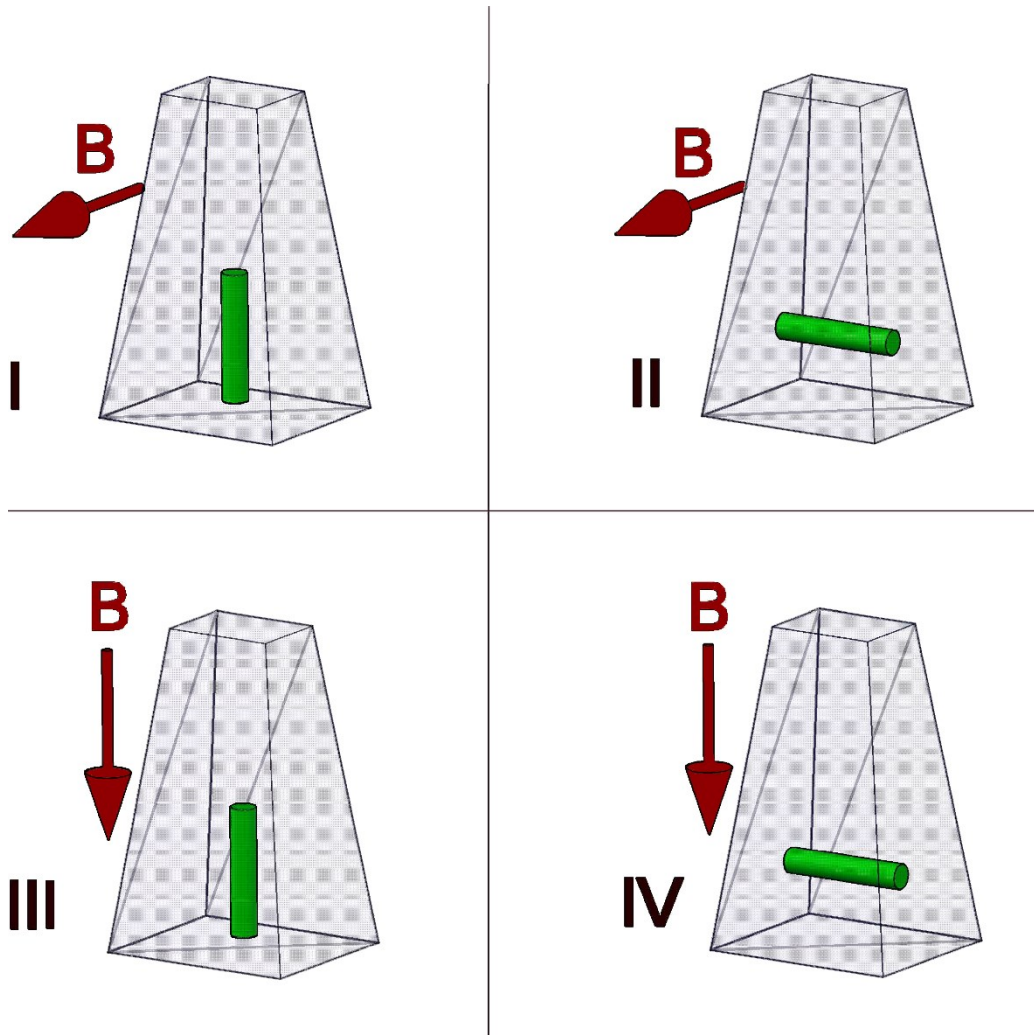


Figure 3.1 Various geometrical orientations for radiation detector's long axis (central cylinder) magnetic field (arrow) and radiation beam (transparent rectangular prism) as used in Monte Carlo simulation and experimental measurements.

### 3.2 Modelling Detectors in PENELOPE

The detectors to have their magnetic field dose response characterized using PENELOPE are the NE2571, PR06C, and A12 cylindrical ionisation chambers, the PTW60003 diamond detector, and the IBA PFD diode detector. The NE2571 chamber was selected for this study to compare directly to the Meijising group measurements<sup>1</sup>. The PR06C was selected because it is widely used for relative dose and quality assurance measurements, and its central electrode is made of C-552 compared to

aluminum used in the NE2571. The final ionisation chamber (A12) was chosen as it is the chamber used as the primary calibration standard at the Cross Cancer Institute (CCI). The solid state detectors (PTF60003, IBA PFD) were chosen as both were available for experimental use, and both types are used regularly for relative dose measurements.

### **3.2.1 PENELOPE Code**

All Monte Carlo simulations used the thoroughly benchmarked code system PENELOPE<sup>4-6</sup>. PENELOPE was used in part because it is capable of low cut-off energies, derived from the well benchmarked<sup>5</sup> special treatment of low energy effects in the physics models used for particle tracking and the generation of interaction cross sections<sup>7</sup>. This special treatment accounts for various atomic effects, and increases low energy accuracy at the expense of simulation speed. This low energy capability allows for the possibility of tracking lower energy particles, which may have a significant effect on the dose deposited in the active volumes of the detectors. This becomes increasingly important as the range of lower energy electrons approaches the scale of the small detection volumes of these solid state detectors, necessitating explicit tracking down to lower energies. PENELOPE also benefits from a simple and powerful detector geometry construction approach. Geometries can be built and viewed in 2D by slice, or in 3D with or without a cutaway, in a short period of time. This helps to ensure completeness of geometries. After each geometry is constructed, the viewer application allows the user to scroll through cross sectional planes along the 3 cardinal axes, or to rotate a 3D representation in space to check for inconsistencies. The geometry can be viewed by material type, or by body type, where a body is a defined sub-volume in the entire geometry (e.g. the diamond disc in the diamond detector). Moreover, PENELOPE contains a main file which implements a rigorous treatment of electromagnetic fields, as presented in the user manual<sup>7</sup>; PENELOPE

methods in conjunction with magnetic field have been used previously by the ART<sup>2</sup> team<sup>2, 3, 8, 9</sup>. The free to use main program pm-field.f (available from the OECD/NEA databank) was used with minimal modifications to eliminate electron track logging. Namely, all lines that wrote electron trajectory to file were commented out.

There are a handful of parameters of interest for the user to define in PENELOPE. WCR and WCC define the energy thresholds for the radiative and hard inelastic collisions respectively. These parameters define the lower cutoff energies for hard inelastic collisions and radiative events, in a mixed random hinge simulation hard interactions do not occur with energies below these values. Eabs is the energy absorption criteria in particle transport. Below this energy a particle is assumed to deposit its energy in place, and is no longer tracked. In the simulation flow the energy and positional information of such particles are tallied, and then the particles are removed from the simulation stack. The WCC, WCR, and Eabs values for electrons, positrons, and photons, are set at 1keV kinetic energy for all detectors. This value gives a good balance between simulation speed, and simulation accuracy, considering the size and composition of the detectors. The maximum step size parameter pertains to the simulation only in the active volumes of the solid state detectors. This value limits the maximum step size of particle transport, which becomes an important parameter as the thickness of a volume of interest decreases. The value is set to 1 micron for both solid state detectors to help ensure particles are modelled appropriately in the volume of interest. The degree by which the mean free path between hard elastic events can be determined by the first transport mean free path is affected by the C1 parameter. The maximum fractional energy loss between hard elastic events is in turn governed by the C2 parameter. These define the degree of mixed simulation by the random hinge method in PENELOPE<sup>4</sup>. They can be varied from 0 (full simulation) to 0.2 (maximum allowed mixed simulation value). The C1 and C2 parameters were set to favour simulation accuracy over speed, and were

more stringent for the PTW 60003 and IBA PFD detectors as compared to the ionisation chambers, owing to the differences in active volume size.

### **3.2.2 Simulation Setup**

A 6 MV photon spectrum for an Elekta linac<sup>10</sup> was used for the NE2571 simulations in order to compare to measured dose response data from another study<sup>1</sup>. A photon spectrum from a 6 MV Varian 600C linac<sup>10</sup> was used for all other detector simulations, as at the time, a Varian 600C linac was available for experiments. Unless otherwise stated, all detectors were simulated at isocentre, 100 cm from the radiation source; the field sizes varied from detector to detector to account for experimental limitations imposed by the magnets used experimentally. All simulation parameters are summarized in table 3.1, and detailed simulation geometries for the detectors are to follow.

Orientations I-IV, as discussed in section 3.1, were simulated for all detectors with the above parameters in a range of magnetic field strengths; additionally, orientations II-2 and V were simulated for the solid state detectors (PTW60003, IBA PFD). In each case, the mean energy deposited in the active volume of each detector as a function of magnetic field strength was scored. The data presented (i.e. the dose response) is the ratio of energy deposited in the presence of the magnetic field, to the energy deposited under identical circumstances without any magnetic field. Simulations in all cases were run for either  $9 \times 10^9$  histories or a number of histories that yielded active volume energy deposition standard deviations on the order of 0.5%, whichever came first.

Detector	Source to detector distance	Field size (cm x cm)	Spectrum	Max Step	PENELOPE parameters
NE Technology ltd NE2571	100cm	4 X 10	6 MV Elekta	N/A	$W_{CR}=W_{CC}=E_{abs}=1 \text{ keV}$ $C1=C2=0.1$
Capintec PR06C	100cm	3.6 X 7	6 MV Varian 600C	N/A	$W_{CR}=W_{CC}=E_{abs}=1 \text{ keV}$ $C1=C2=0.1$
Exradin A12	100cm	10 X 10	6 MV Varian 600C	N/A	$W_{CR}=W_{CC}=E_{abs}=1 \text{ keV}$ $C1=C2=0.1$
PTW60003 Diamond	100cm	2 x 4	6 MV Varian 600C	0.0001 cm	$W_{CR}=W_{CC}=E_{abs}=1 \text{ keV}$ $C1=C2=0.01$
IBA PFD Diode	100cm	2 x 4	6 MV Varian 600C	0.0001 cm	$W_{CR}=W_{CC}=E_{abs}=1 \text{ keV}$ $C1=C2=0.05$

Table 3.1 Geometrical setup and PENELOPE simulation parameters for each detector investigated.

### 3.2.3 Detector Geometries

All material compositions used in the construction of the simulation geometries were generated within the PENELOPE code system. PENELOPE allows the user to either create new materials with defined elemental abundances and associated cross sections, or use the default pre-defined materials whose compositions are well known. The material files used in this investigation were all generated from a pre-defined database of known materials using a companion program contained in the PENELOPE code.

The NE2571 chamber's simulated geometry (seen in figure 3.2) was a series of cylinders corresponding to the cross sectional layout of the chamber. The air cavity was cylinder of 6.3 mm diameter and 21.8 mm

length. The air cavity was surrounded by a graphite wall of 0.35 mm annular thickness. The central, solid electrode with 1 mm diameter and 20.6 mm length was made from aluminum. This chamber was placed in water phantom (30x30x30 cm<sup>3</sup>) at a depth of 4 cm in order to match the simulation geometry to previous work done with the same chamber by Meijnsing *et al*(2009)<sup>1</sup>.

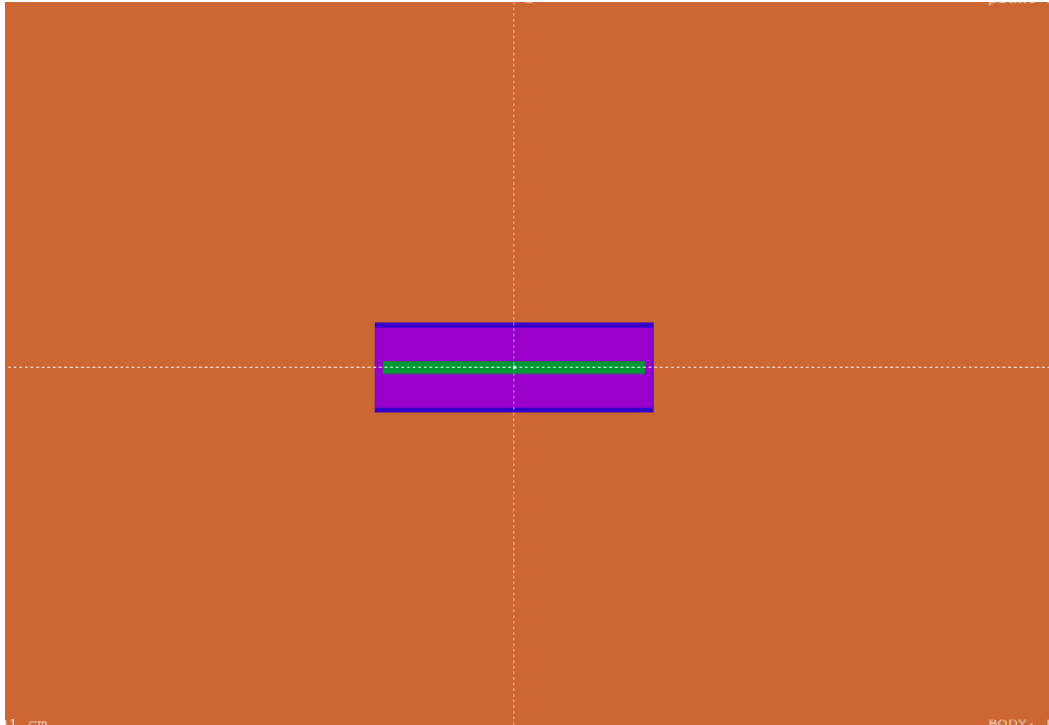


Figure 3.2 Schematic of the NE2571 ionisation chamber. Purple is the air cavity itself, green the Al electrode, blue the graphite wall, and orange the water buildup.

The PR06C chamber had a simulation geometry (see figure 3.3) that matched the readily available data from manufacturers and distributors. The PR06C chamber was modelled as a central cylindrical air cavity of 6.4 mm diameter and 20.2 mm length with a spherical tip extending a further 1.8 mm. The central C-552 electrode has a diameter of 1.6 mm and length of 21.1 mm where C-552 refers to a synthetic, conducting plastic that is considered to be air equivalent in its photon mass attenuation properties. The C-552 annular wall had a constant radial thickness of 0.28mm that surrounded the air cavity. A 24 mm long solid C-552 cylindrical stem with a diameter matching the outer diameter of the wall was also included in the

simulation. The PR06C chamber was simulated in air with a PMMA buildup cap that fit snugly, as per the experimental conditions. The buildup cap was simulated with a cylindrical body and spherical tip with an inner surface matching the chamber; it extends through the length of the stem, and is of uniform thickness of 12.7mm.

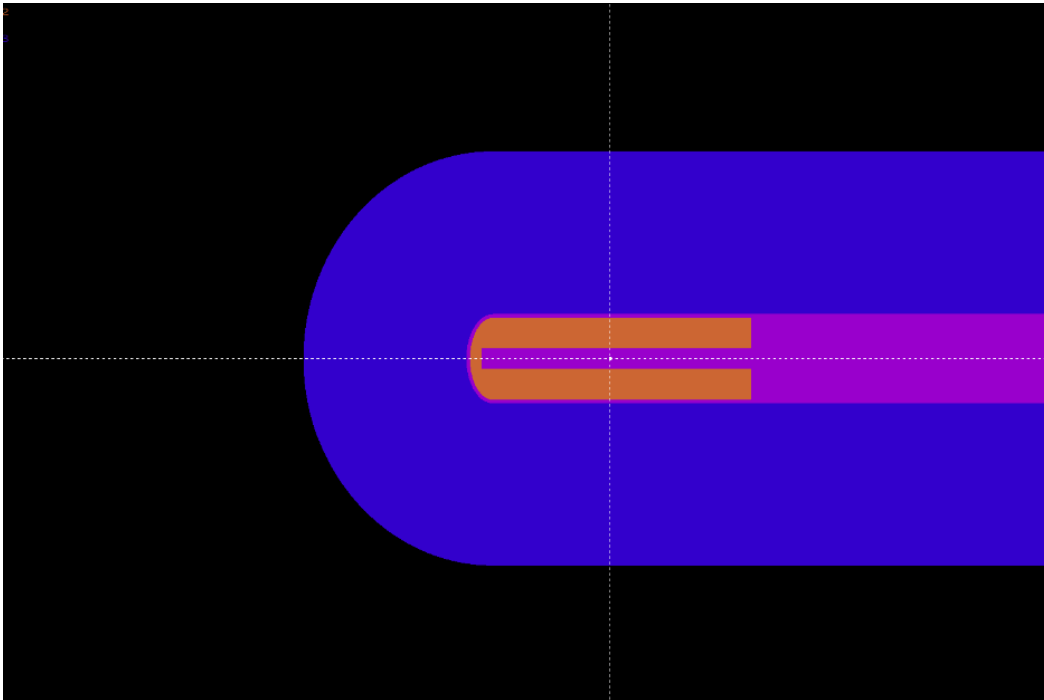


Figure 3.3 Schematic of the PR06C ionisation chamber. The central orange region is the air cavity, the purple wall, electrode, and stem are the C-552 conducting plastic, blue is the PMMA buildup cap, and black is vacuum.

The A12 chamber (figure 3.4) is used as a primary calibration standard for TG-51, and as such it was simulated as per the TG-51 protocol at 10 cm depth in a homogeneous 30x30x30 cm<sup>3</sup> water phantom<sup>11</sup>. Due to the large dimensions of the chamber itself, in addition to the dimensions of the water tank, the A12 ionisation chamber did not have an experimental counterpart. The air cavity for the A12 was modelled as a cylinder of 6.1mm diameter and 19.8 mm in length, with a spherical tip extending a further 3 mm at one terminus of the cylinder. Both the wall and electrode materials were simulated as C-552 plastic; the wall is 0.5 mm in thickness at all points surrounding the air cavity, and the electrode is 1mm in diameter and 20.2 mm in length. The stem of the chamber was modelled as two C-552

cylinders immediately adjacent to the air cavity. The first cylinder is 9.8 mm in diameter, and extends 5.41 mm from the terminus of the air cavity, while the second is 2.502 cm in diameter and extends 3.58 cm from the first stem cylinder.

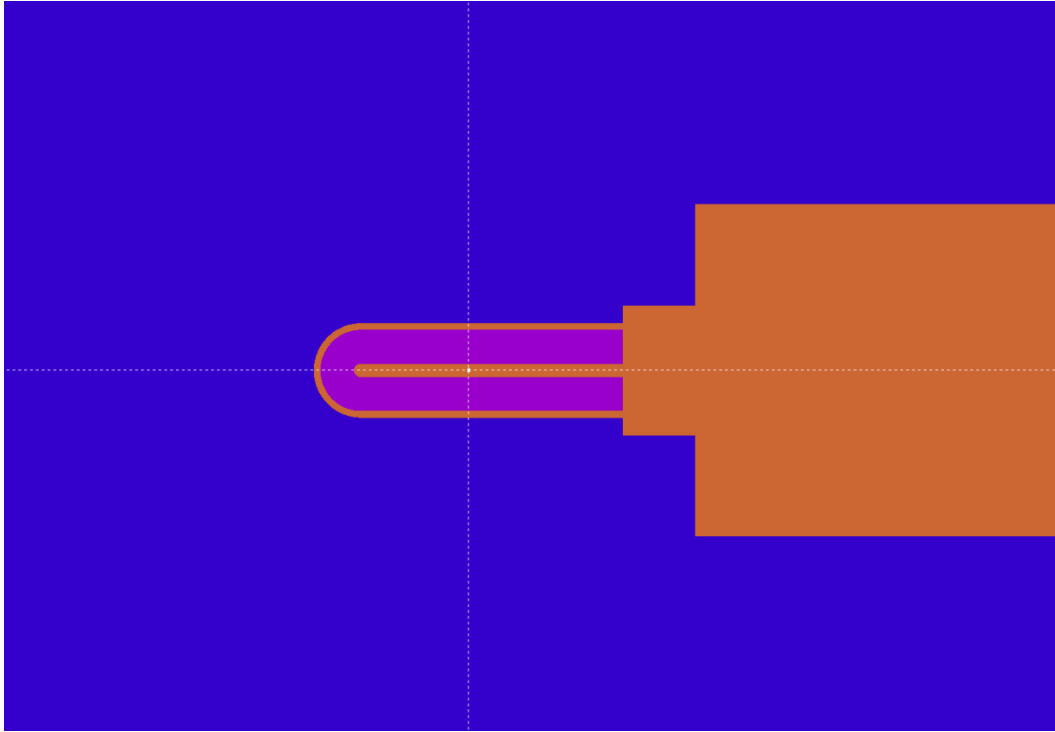


Figure 3.4 Schematic of the A12 ionisation chamber. The central purple region is the air cavity, the orange wall, electrode, and stem are C-552 conducting plastic, and the blue is water.

To ensure the accuracy of the ionisation chamber geometries, two of the simulated chambers were benchmarked without a magnetic field in addition to being compared to the measured relative data in a magnetic field. Benchmarking simulations were performed for the NE2571 and PR06C chambers in the absence of magnetic field. For each chamber model, the values of the factor  $k_Q$  as used in the TG-51 protocol<sup>11</sup> were determined using the formalism outlined by Muir *et al* (2010)<sup>12</sup>:

$$k_Q = \frac{\frac{D_w^Q}{D_{ch}^Q}}{\frac{D_w^{60Co}}{D_{ch}^{60Co}}} \quad (3-1)$$

Where  $D_w^Q$  is the dose to a small mass of water (0.025 cm thick disc of 1 cm radius) at 10 cm depth on the central axis of a beam of quality Q, and  $D_{ch}^Q$  is the dose to the chamber using identical parameters. Likewise,  $D_w^{60Co}$  is the dose to a small mass of water at 5 cm depth in a cobalt-60 beam (5 cm is the calibration depth) and  $D_{ch}^{60Co}$  is the dose to the chamber using identical parameters. All of the  $k_Q$  simulations employed the same PENELOPE simulation parameters outlined in table 3.1. To ensure validity of the chamber models; the results of these simulations were compared to the previous Monte Carlo study of  $k_Q$  values, and published values in TG-51<sup>11</sup>.

The PTW60003 diamond detector's simulation geometry was constructed using a combination of schematics from the manufacturer, and a previously published simulation geometry<sup>13</sup>, it is pictured in figure 3.5 A. The main body of the detector was a cylinder of 7.3 mm diameter and 20 mm length. The active volume of the detector was a diamond, 1.47 mm in radius, and 0.25 mm in thickness. The edge of the active volume was positioned at 1mm below the top surface of the detector's housing. The air cavity positioned behind the active volume of the detector was modelled as being 2.65 mm in radius, and 5 mm in length, its face was positioned 1.75 mm below the end of the active volume of the detector. With exception of the air gap and diamond itself, the detector materials were all simulated as polystyrene, as the exact composition of the epoxy setting is unknown.

The IBA PFD diode detector, as seen in figure 3.5 B, was modelled with similar dimensionality and materials as other Monte Carlo work with the IBA PFD diode detector<sup>14</sup>. The active volume (silicone) was a disc 0.5 mm thick and 2.5 mm in diameter, set 0.3 mm below the surface of the detector. The 2.5 mm diameter region behind the active volume was modelled as epoxy through the remainder of the 17 mm length of the detector. The tip of the detector (0.3 mm in thickness above the silicone) was modelled as ABS plastic. The remainder of the detector is a series of 3 annuli around the

central 2.5 mm diameter central region. The first annulus extends from 2.5 mm to 4.4 mm thickness, and is ABS plastic through the 17 mm length of the detector. The second annulus extends from 4.4 mm to 5.8 mm in thickness. It is composed of tungsten for the first 10 mm in detector length, and epoxy for the remaining 7 mm of detector length. The final annulus extends from 5.8 mm in thickness to 7.2 mm, and is ABS plastic for the entire 17 mm length of the detector. ABS (Acrylonitrile Butadiene Styrene) is a plastic of density  $\sim 1.07 \text{ g/cm}^3$ ; it is a tough, rigid plastic which is commonly used for protective headgear, musical instruments, and Lego.

The diamond and diode detectors were both simulated in air, with a tight fit PMMA buildup cap included. The cap was simulated with a cylindrical body and flat tip, each extending 1.27 cm from the detector to provide sufficient 6MV buildup. This cap has been excluded from figure 3.5 in order to highlight detector compositions, but it was included in the simulation geometry.

In an effort to study the dose response mechanisms of the two solid state detectors, in air simulations of orientations I-IV were additionally repeated with a change in detector composition implemented. The PTW 60003 was simulated with the air gap replaced by polystyrene, and the IBA PFD was simulated with all non-detection volume materials, including the tungsten shield, set to polystyrene. All other simulation parameters, including the presence and composition of the buildup cap, remained unchanged. Models of the modified PTW 60003 diamond and IBA PFD diode detectors are pictured in figures 3.5 C and 3.5 D respectively.

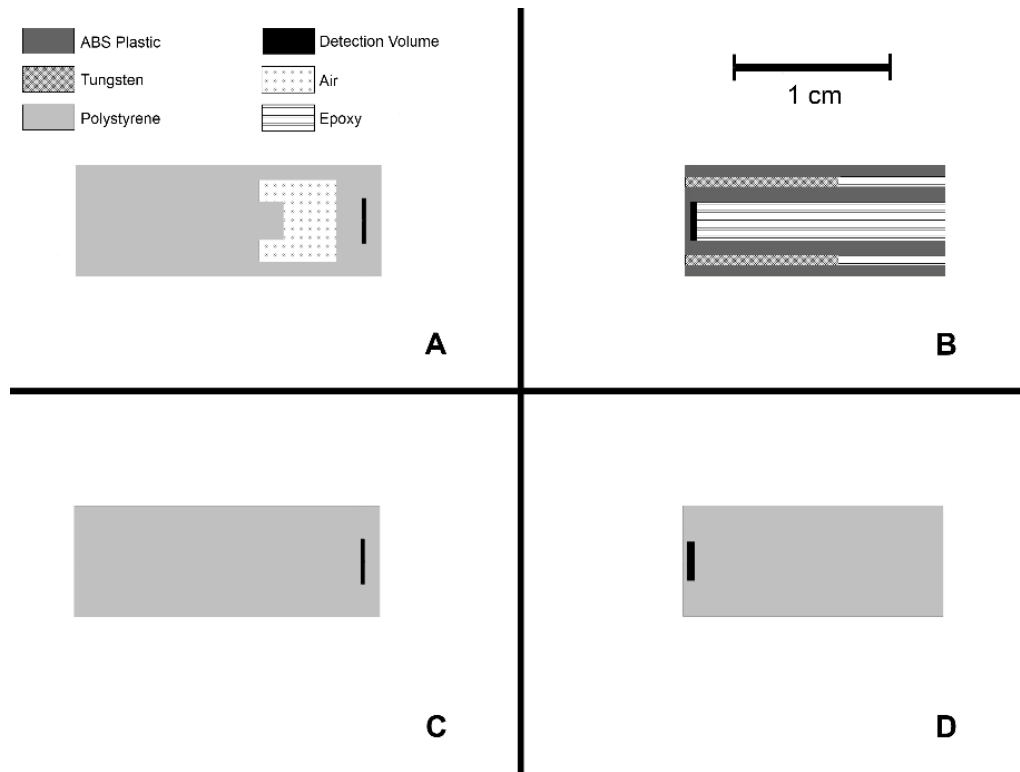


Figure 3.5 PTW 60003 diamond detector (A and C) and IBA PFD diode detector (B and D) simulated geometries without changes (A and B) and with changes to materials (C and D). Material legend is in the top left, background material is not shown, and is PMMA in all cases.

### 3.2.4 Beam Scanning Simulations

The solid state detectors are typically used for relative measurements concerning the beam profile and relative dose at depth in a water tank. In an effort to evaluate both the behaviour of these detectors as they would be used clinically, and the applicability of the in-air measurements, simulations for both solid state detectors were also performed in a 20 cm x 20 cm x 20 cm water tank. These simulations used the aforementioned photon beam at source to surface distance (SSD) of 95 cm, and a 10 cm x 10 cm field size defined at 100 cm from the source. Each simulation was done both without a magnetic field, and with either a transverse (figures 3.1.I, 3.1.II), or longitudinal (figure 3.1.III, 3.1.IV) magnetic field, with a field strength of 0.5 T. The detectors were simulated as they were in air, without the buildup

caps, in dose at depth, and beam profile geometries. The dose at depth geometry used the parallel detector orientation (figure 3.1.I, 3.1.III). Dose at depth simulations were done with the active volume of each detector at  $D_{max}$  (1.5 cm) and again at a depth of 5 cm. The beam profile geometry used the perpendicular detector orientation (figure 3.1.II, 3.1.IV). The beam profile geometry was simulated with each detector in 4 different positions. The centres of the active volumes of the detectors were positioned at  $D_{max}$ , at 5 cm depth on the CAX (central axis), and then at the left and right edges of the collimated photon field dimensions (5 cm from CAX in either direction). The dose response in each case was defined as the ratio of the simulation result with magnetic field to that without a magnetic field in the same geometry.

It is possible that the dose to water changes in the presence of magnetic field, such as at interfaces of differing materials; radiation detectors are expected to accurately measure this change. However, the accuracy of the dose to water as measured by the detector may change depending on the detectors' position in the beam and magnetic field. In order to validate the simulated behaviour of the solid state detectors in a water tank, the dose to water at the simulated points in the absence of any detector was also simulated. The dose to water along the central axis (a percent depth dose), and the dose to water at the periphery of the fields at 5 cm depth, and 5 cm left and right of the central axis (beams eye view) were scored. The ratio of the doses to water with and without a magnetic field applied was taken for comparison to the ratio of energy deposited in the detectors' sensitive volume. The simulation parameters used for the dose to water were identical to the simulation parameters for the diode detector. The detectors' behaviour in the water tank can be compared to both the dose to water at that point, as well as to the in air simulations and measurements to assess any changes to the in air magnetic field dose responses when the detectors are used in a phantom. We can also evaluate the potential use of these detectors in beam scanning situations.

While the solid state detectors above are typically used for the purposes of beam profile and depth scanning, they are not the only detectors to be used for this purpose. The CC13 is a small ( $0.13 \text{ cm}^3$  detection volume) ionisation chamber used for relative dosimetry purposes, such as beam profile and depth scanning. Therefore, in addition to the solid state detector water tank simulations, the CC13 chamber was also simulated at depth in a  $30 \text{ cm} \times 30 \text{ cm} \times 30 \text{ cm}$  water tank for the purposes of comparison and evaluation. These simulations used the aforementioned photon beam at source to surface distance (SSD) of  $90 \text{ cm}$ , and a  $10 \text{ cm} \times 10 \text{ cm}$  field size defined at  $100 \text{ cm}$  from the source. The chamber long axis was oriented perpendicular to the photon beam in all simulations, as per clinical use. Each simulated chamber location within the beam was done both without a magnetic field, and with either a transverse (orientations II, V) or longitudinal (orientation IV) magnetic field of strength  $0.5 \text{ T}$ . The CC13 chamber was simulated at  $D_{\text{max}}$ ,  $5 \text{ cm}$  depth, and  $10 \text{ cm}$  depth on the CAX, and at all four peripheral photon field positions at  $10 \text{ cm}$  depth ( $5 \text{ cm}$  from the CAX left, right, up, and down, see figure 3.6). The dose response in each case was defined as the

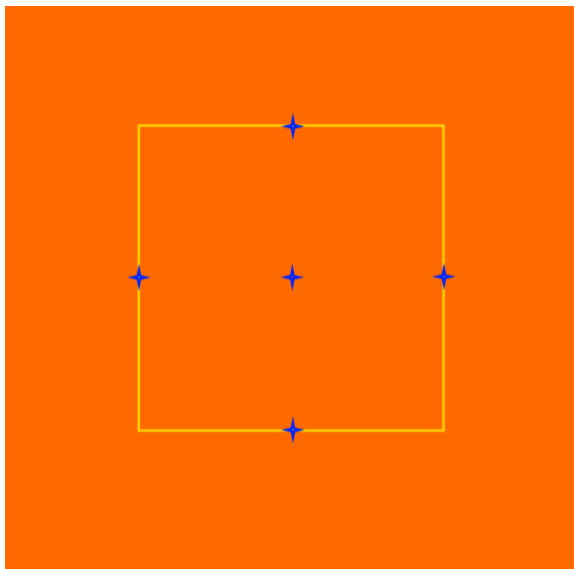


Figure 3.6 Illustration of the water tank simulation positions at  $10 \text{ cm}$  depth for the CC13 chamber. Orange represents the water tank, yellow the  $10 \text{ cm} \times 10 \text{ cm}$  periphery of the radiation field at  $10 \text{ cm}$  depth, and blue are the simulation points.

ratio of the simulation result with magnetic field to that without a magnetic field in the same geometry. As before, the dose to water at the peripheral regions was also scored using identical simulation parameters for the purposes of comparison. Changes in chamber response due to the magnetic field of the beam depth and lateral profiles can be compared to the actual dose to water at that point, and

the use of the CC13 in these situations can be evaluated.

The CC13 chamber itself was modelled as per manufacturer data sheets accompanying the chamber; a schematic of the chamber is pictured in figure 3.7. The inner electrode and outer wall of the collection volume are modelled as C-552 conducting plastic. The inner electrode is 1 mm in diameter, and 3.3 mm in length; the chamber wall is a constant 0.4 mm thick. The inner diameter of the air cavity cylinder is 6.0 mm, and is 2.8 mm in length; the spherical tip of the air cavity is centered at the terminus of the cylindrical section, and is 3.0 mm in radius. The inner electrode and conducting walls of the detector extend a further 6.1 mm into the stem from the air cavity and stem interface. The stem is made from PEEK plastic, and is composed of two consecutive cylinders immediately adjacent to the active volume of the detector. The first cylinder is 6.0 mm in diameter (with a 0.4 mm thick C-552 wall as shown in figure 3.7) and 4.4 mm in length; the second cylinder is 10 mm in diameter, and is modelled as extending a further 17.4 mm from the interface with the first cylinder.

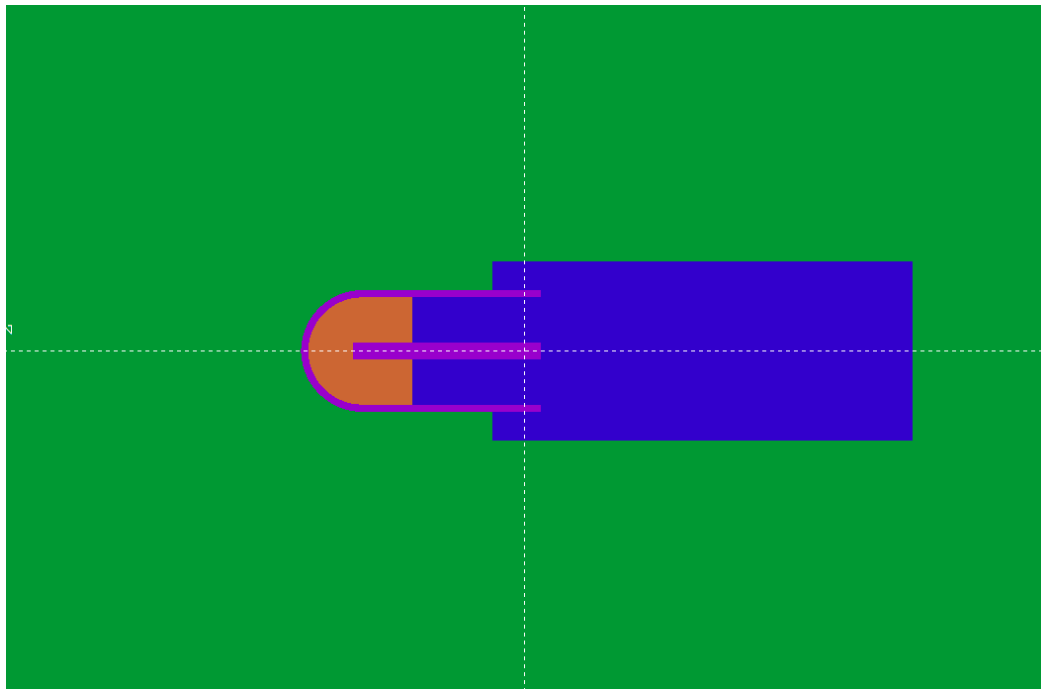


Figure 3.7 Schematic of the CC13 ionisation chamber. The central orange region is the air cavity, the purple electrode and wall are C-552 conducting plastic, blue is the PEEK stem, and green is water.

PEEK (Polyether Ether Ketone) is a plastic of density  $\sim 1.32 \text{ g/cm}^3$ ; PEEK is a robust plastic resistant to degradation, and is one of the few plastics compatible with ultra-high vacuum applications. PEEK is also used to fabricate high stress parts such as bearings, piston parts, and various valves.

### **3.3 Measurement Setup**

Measurements in air using ionisation chambers were limited to the PR06C, as a NE2571 chamber is unavailable for use in our lab, and the A12 is too large physically to be used with the electromagnets available. No water tank measurements were performed with any detector, as the water tank is also too large for use with the available electromagnets. The PR06C, PTW60003 diamond detector, and IBA PFD diode detector were all measured in air in both transverse and longitudinal field geometries (orientations I-IV) for comparison to simulation results. During the course of the dose response measurements the linear accelerator used initially (Varian 600C, Varian Medical Systems, Palo Alto, CA) was replaced. Subsequent measurements were therefore made with a Varian 23EX accelerator (Varian Medical Systems, Palo Alto, CA). Both linacs are produced by Varian, and the differences in the 6MV spectra utilized are expected to be on the order of, or less than, the differences seen between manufacturers<sup>10</sup>. This inter-machine variability is small in magnitude, and will have negligible overall impact, especially compared to the mechanisms driving the dose response of the detectors themselves. The transverse magnetic field measurements of the PR06C and PTW60003 employed the Varian 600C 6 MV photon beam, all other measurements employed the Varian 23EX 6 MV photon beam.

The detectors investigated were pre-irradiated according to manufacturer recommendations before use where applicable. The PR06C chamber operated with a 300V bias, the PTW60003 detector was operated with a 100V bias, and the IBA PFD detector was operated without the application of an external bias. The measurements obtained are presented as the ratio of charge collected with magnetic field, to that collected without magnetic field. This ratio will allow for the determination of a correction factor for the associated radiation detector when used in a particular orientation at a specified magnetic field strength. This correction factor is the inverse of the observed response (0.95 for a response of 1.052). A similar ratio was also calculated using the Monte Carlo simulations and can therefore be compared directly with the measured ratio.

There are several sources of measurement error that lead to uncertainty in the measurement values obtained. These sources of error can come from the resolution of the physical equipment used, such as the limited significant digits on the electrometer used for charge collection, and the mm accuracy of the ruler used for detector positioning. There is also uncertainty in the voltage measured across the Hall probe by the multi-meter, as well as uncertainty in the Hall probe itself (1% as claimed by the manufacturer). Additional uncertainty arises as multiple measurements are taken and averaged, introducing a statistical uncertainty.

### **3.3.1 Transverse Magnetic Field Measurements**

The PR06C transverse magnetic field (orientations I, II) measurements were made in air with a PMMA buildup cap of thickness 1.27 cm fitted onto the chamber to ensure electronic equilibrium. A small electromagnet was used in the experiments to obtain a variable transverse field strength. The chamber and buildup cap combination was placed between the poles of the small electromagnet (EEV M4261, Chelmsford England) at the approximate

center of the magnet in orientations I and II. The poles of the magnet measure 7.5 cm in diameter and are separated by a distance of 7.5 cm. The magnetic field strength at the center of magnet was varied from 0T to ~0.20 T. The magnetic field strength between the poles was measured with a 3 dimensional hall probe (SENIS GmbH C-H3A-2m\_E3D-2.5kHz-1%-0.2T), which has an accuracy of 1% as claimed by the manufacturer. Although, the maximum field strength of the electromagnet was limited to ~0.20 T, this field strength was previously found to be useful for the autocontouring<sup>15</sup> of simulated tumour in lung background. It should also be noted that the phase one prototype Linac-MR system uses 0.21 T permanent magnet<sup>16</sup>, and the currently available commercial MR-simulation<sup>17</sup> and proposed system from ViewRay<sup>18</sup> also use a similar magnetic field strength.

The ionisation chamber was set at the isocentre at a distance of 100 cm from the radiation source. The physical size of the electromagnet limited the radiation field size to 4 x 7 cm<sup>2</sup>; however, this was sufficiently large to cover the buildup cap and the active volume (0.65 cm<sup>3</sup>, 24 mm length) of the chamber in both orientations. In each measurement 100 MUs (where an MU is a monitor unit, a unit of measure of radiation produced by the accelerator calibrated using some standard, TG-51 for example<sup>11</sup>) were delivered and the electrometer reading recorded. This was repeated three times per magnetic field strength, the average of these three was used as the data point associated with the magnetic field. After the measurement set was complete the baseline (no magnetic field) measurement and three intermediate field strengths were verified to ensure the absence of any measurement drifts.

An effort was made to investigate a select few parameters specific to TG-51 for their individual contributions to the change in chamber response due to a magnetic field. Measurements of  $P_{ion}$  and  $P_{pol}$  as defined in TG-51<sup>11</sup> were thus made at magnetic field strengths of 0.0 T, 0.09 T, and 0.14 T. The chamber was set at isocentre (100 cm) in orientation II and irradiated

with 100 MUs at 6 MV using a field size of 4 x 7 cm<sup>2</sup>. P<sub>ion</sub> and P<sub>pol</sub> values were calculated according to well-known methods using chamber readings at varying bias voltages and polarity as follows<sup>11, 19</sup>:

$$P_{ion} = \frac{1 - \frac{V_H}{V_L}}{\frac{M_{raw}^H}{M_{raw}^L} - \frac{V_H}{V_L}} \quad (3-2)$$

$$P_{ion} = \frac{1}{f} \quad (3-3a)$$

$$f = \frac{1}{u} \ln(1 + u) \quad (3-3b)$$

$$\frac{M_{raw}^H}{M_{raw}^L} = \frac{V_H}{V_L} \frac{\ln(1 + u)}{\ln\left(1 + u \frac{V_H}{V_L}\right)} \quad (3-3c)$$

$$P_{pol} = \frac{M_{raw}^+ - M_{raw}^-}{2M_{raw}^+} \quad (3-4)$$

Equations 3-2 and 3-4 are found within the TG-51 protocol<sup>11</sup>, and equations 3-3a – 3-3c define an alternate P<sub>ion</sub> method<sup>19</sup>. Within the P<sub>ion</sub> formulae, V<sub>H</sub> and V<sub>L</sub> represent the high and low bias voltages used, M<sub>raw</sub><sup>H</sup> and M<sub>raw</sub><sup>L</sup> are the raw electrometer readings for the high and low voltages (V<sub>H</sub> and V<sub>L</sub>). Equation 3-2 is a straightforward calculation, and numerical or graphical methods can be used to solve the transcendental equation 3-3c for u, which can be ultimately related to P<sub>ion</sub>. Finally, the equation 3-4 P<sub>pol</sub> measurement requires a positive and equally negative voltage reading (i.e. ±300 V); M<sub>raw</sub><sup>+</sup> and M<sub>raw</sub><sup>-</sup> are the raw electrometer readings for the positive and

negative voltage. The correction factors  $P_{ion}$  and  $P_{pol}$  account for ion recombination and polarity effects respectively.

The relative nature of the simulation data makes it unnecessary to study the consequences of changing field sizes, resulting in variable head or phantom scatter, provided the field size remains the same in simulations with and without the magnetic field. However, to ensure the change in magnetic field dose response does remain constant with field size, the response is measured for a variety of field sizes in two non-zero magnetic field strengths. These measurements were made in orientation II, and used identical parameters as above, with exception to field size. The resultant ratios are compared with one another from field size to field size, and to the original simulation values.

The transverse magnetic field PTW 60003 and IBA PFD measurements were made in air with the aid of a 0.2 cm thick brass buildup cap to ensure electronic equilibrium in the detectors. The detectors with buildup caps were placed at the centre of the two poles of the EEV electromagnet (EEV M4261, Chelmsford England) in each of orientations I and II. Measurements in orientation II were taken twice, with the detector rotated 180 degrees in the plane of the long axis in the second set (orientation II-2). In the experiments involving these solid state detectors, the magnetic field strength was varied from 0 T to ~0.20 T. The field strength of the electromagnet in the central region between the poles was again verified using a 3 dimensional hall probe (SENIS GmbH C-H3A-2m\_E3D-2.5kHz-1%-0.2T), which the manufacturer claims has an accuracy of 1%.

The active volumes of the detectors were set at the isocentre, 100 cm from the source of radiation. The field size used was 2 cm x 4 cm at isocentre, which was sufficient to encompass the entire detector volume. A set of three 100 MU readings was taken at each magnetic field strength and orientation for both detectors. The average of these three measurements was taken as the data point for the associated magnetic field. To verify the stability of the

measurements, once the data set was complete, the baseline (no magnetic field) and readings for three intermediate field strengths were re-measured to ensure they were unchanged.

The measured ratio of dose response with magnetic field to that without magnetic field will be directly compared to the simulation results. It is true that the differences in buildup cap material will alter the composition and spectrum of incident radiation on the active volume of the detector; however, this change is expected to be small, and will differ depending on the exact composition of the brass in the cap, which is unknown. It is also worth noting that the spectrum used in the simulations will differ slightly from that produced by the linac itself, as well as from linac to linac. These spectrum perturbations will be small, and are expected to be inconsequential to the relative nature of this work.

### **3.3.2 Longitudinal Magnetic Field Measurements**

Verification measurements of the simulated longitudinal field dose response of the PR06C farmer chamber<sup>2</sup>, PTW6003 diamond detector<sup>3</sup>, and IBA PFD diode detector<sup>3</sup> were also completed. The longitudinal magnetic field was produced by a pair of solenoidal electromagnet coils (GMW 11801364 coil X 2, San Carlos, CA) stacked on one another. The central bore created in this configuration is 26.5 cm in depth, and 17.7 cm in diameter; the outer diameter of the coils is 39.3 cm. This configuration allows for a relatively homogeneous longitudinal magnetic field in the central bore region; this is the region where the detectors will be placed in either orientation III or IV and irradiated. The magnetic field in the bore was measured with a 3 dimensional hall probe (Metro Lab THM1176) as a function of applied current, and was 0.003 T per ampere in the central region. It should be noted that the magnetic field is produced by the coils in the air gap; there is neither a pair of pole tips nor a yoke to enhance the magnetic field. The

weight of the electromagnet configuration is too substantial to be placed in the accelerator couch, as a result, the magnets reside on a small stand on the floor beneath the accelerator source. The centre of the bore of the electromagnet resultant sits at 182 cm from the accelerator photon source. This distance differs from the 100 cm distance employed in the simulation studies, however, this change in distance will only have a significant effect on the dose rate seen by the detector. The relative nature of the dose response measurements precludes any correction for this effect. Each of the three detectors was placed in the centre of the bore of the electromagnet, and measurements were taken in orientations III and IV as the magnetic field strength was varied from 0 to ~0.2 T. Measurements were made in air with a 1.27 cm PMMA buildup cap (PR06C) or a 0.2 cm brass buildup cap (PTW60003, IBA PFD) to ensure electronic equilibrium. The field sizes at the centre of the detectors were 4 cm x 7 cm for the PR06C, and 2 cm x 4 cm for the PTW60003 and IBA PFD detectors. The longitudinal field measurements were in part completed to compare with previously simulated results. Thus the field sizes used for the various detectors are identical to those that were simulated previously<sup>2, 3</sup>. These fields are also significantly smaller than bore size (7.5 cm diameter) of the transverse field electromagnet so as to avoid irradiation of the electromagnet.

Three 100 MU readings were taken at each magnetic field strength, and the average of these three measurements was taken as the data point for the associated magnetic field. The stability of the measurements was verified by re-measuring three field strengths (including zero magnetic field) to ensure they were unchanged.

### **3.3.3 OS� Measurements**

Finally, Landauer Nanodot OS�s (Optically Stimulated Luminescence detectors) were investigated experimentally for their dose response as a

function of magnetic field. These detectors are commonly used clinically as dose verification devices, and their dose response in a magnetic field is of interest. The Nanodot is a small flat OSL encased in plastic measuring 1 cm square containing a small mass of  $\text{Al}_2\text{O}_3$  OSL material; more information on the Nanodot can be obtained from the manufacturer (Landauer, Glenwood Illinois). The 6MV beam from a Varian 23EX accelerator was used in conjunction with longitudinal (GMW 11801364 coil X 2, San Carlos, CA) and transverse (EEV M4261, Chelmsford England) electromagnets to measure the dose responses of the OSL detectors. The source to OSL distance for the longitudinal magnetic field measurements was 182 cm, and the source to OSL distance in all transverse magnetic field measurements was 100 cm. In each case, the OSL was centred in a beam of size 4 cm x 4 cm at the surface of the OSL. "Super Flab" bolus, a synthetic oil gel with a density of 1.02 grams per cubic cm, of 2 cm thickness was placed on top of the OSL in all measurements made. The bolus was used to ensure electronic equilibrium incident on the OSL. In order to investigate the electron return effect, an additional set of measurements with 2 cm of "Super Flab" bolus at both the beam entrance and exit side of the OSL was conducted in transverse magnetic fields.

To obtain measurements, 100 MU was delivered to the bolus and OSL configuration as the magnetic field was incremented from 0 to ~0.2 T. Both the initial dose of the OSLs, and the dose after irradiation were taken to be the average of 3 readings. The difference between the average initial and final dose readings was considered to be the dose deposited in the OSL detector. The actual dose values in the longitudinal field and transverse field cases are significantly different due to the increased source to measurement distance. However, the data is (as prior) presented as the ratio of dose with magnetic field to that without magnetic field. This allows us to directly compare the longitudinal and transverse magnetic field cases. This ratio may also allow us to determine, from the dose response, a

correction factor for the use of OSLs in these situations, if the need for any correction exists.

### 3.4 References

- 1 I. Meijnsing, B.W. Raaymakers, A.J.E. Raaijmakers, J.G.M. Kok, L. Hogeweg, B. Liu, and J.J.W. Lagendijk, “Dosimetry for the MRI accelerator: the impact of a magnetic field on the response of a Farmer NE2571 ionization chamber.,” *Phys. Med. Biol.* **54**(10), 2993–3002 (2009).
- 2 M. Reynolds, B. Fallone, and S. Rathee, “Dose response of selected ion chambers in applied homogeneous transverse and longitudinal magnetic fields,” *Med. Phys.* **40**(4), 042102 (2013).
- 3 M. Reynolds, B.G. Fallone, and S. Rathee, “Dose response of selected solid state detectors in applied homogeneous transverse and longitudinal magnetic fields,” *Med. Phys.* **41**(9), 092103 (2014).
- 4 J. Baro, J. Sempau, J.M. Fernández-Varea, and F. Salvat, “PENELOPE: an algorithm for Monte Carlo simulation of the penetration and energy loss of electrons and positrons in matter,” *Nucl. Instruments Methods Phys. Res.* (100), 31–46 (1995).
- 5 J. Sempau, J.M. Fernández-Varea, E. Acosta, and F. Salvat, “Experimental benchmarks of the Monte Carlo code penelope,” *Nucl. Instruments Methods Phys. Res. Sect. B Beam Interact. with Mater. Atoms* **207**(2), 107–123 (2003).
- 6 J. Sempau, E. Acosta, J. Baro, J.M. Fernández-Varea, and F. Salvat, “An algorithm for Monte Carlo simulation of coupled electron-photon transport,” *Nucl. Instruments Methods Phys. Res. Sect. B Beam Interact. with Mater. Atoms* **132**(3), 377–390 (1997).
- 7 F. Salvat, J.M. Fernandez-Varea, and J. Sempau, *PENELOPE: A code system for Monte Carlo simulation of electron and photon transport* (2006).
- 8 C. Kirkby, T. Stanescu, S. Rathee, M. Carlone, B. Murray, and B.G. Fallone, “Patient dosimetry for hybrid MRI-radiotherapy systems,” *Med. Phys.* **35**(3), 1019–1027 (2008).
- 9 C. Kirkby, T. Stanescu, and B.G. Fallone, “Magnetic field effects on the energy deposition spectra of MV photon radiation.,” *Phys. Med. Biol.* **54**(2), 243–57 (2009).

- 10 D. Sheikh-Bagheri and D.W.O. Rogers, "Monte Carlo calculation of nine megavoltage photon beam spectra using the BEAM code," *Med. Phys.* **29**(3), 391–402 (2002).
- 11 P.R. Almond, P.J. Biggs, B.M. Coursey, W.F. Hanson, M.S. Huq, R. Nath, and D.W. Rogers, "AAPM's TG-51 protocol for clinical reference dosimetry of high-energy photon and electron beams.," *Med. Phys.* **26**(9), 1847–70 (1999).
- 12 B.R. Muir and D.W.O. Rogers, "Monte Carlo calculations of  $k_{[sub Q]}$ , the beam quality conversion factor," *Med. Phys.* **37**(11), 5939–5950 (2010).
- 13 P.N. Mobit and G. a Sandison, "An EGS4 Monte Carlo examination of the response of a PTW-diamond radiation detector in megavoltage electron beams.," *Med. Phys.* **26**(5), 839–44 (1999).
- 14 K. Eklund and A. Ahnesjö, "Spectral perturbations from silicon diode detector encapsulation and shielding in photon fields," *Med. Phys.* **37**(11), 6055–6060 (2010).
- 15 J. Yun, E. Yip, K. Wachowicz, S. Rathee, M. Mackenzie, D. Robinson, and B.G. Fallone, "Evaluation of a lung tumor autocontouring algorithm for intrafractional tumor tracking using low-field MRI: a phantom study.," *Med. Phys.* **39**(3), 1481–94 (2012).
- 16 B.G. Fallone, B. Murray, S. Rathee, T. Stanescu, S. Steciw, S. Vidakovic, E. Blosser, and D. Tymofichuk, "First MR images obtained during megavoltage photon irradiation from a prototype integrated linac-MR system," *Med. Phys.* **36**(6), 2084–2088 (2009).
- 17 L. Chen, R. Price, J. Li, L. Wang, L. Qin, and C. Ma, "Evaluation of MRI-based Treatment Planning for Prostate Cancer using the AcQPlan System," *Med. Phys.* **30**(6), 1507 (2003).
- 18 S. Goddu, O. Pechenaya Green, and S. Mutic, "TG-51 Calibration of First Commercial MRI-Guided IMRT System in the Presence of 0.35 Tesla Magnetic Field," *Med. Phys.* **39**, 3968 (2012).
- 19 M.S. Weinhaus and J. a Meli, *Determining Pion, the correction factor for recombination losses in an ionization chamber.*, *Med. Phys.* **11**(6), 846–9 (1984).

# Chapter 4: Results and Discussion

This chapter will detail the results of the simulation and experimental designs outlined in chapter 3. Preliminary measurements of various correction factors affecting the dose deposition and dose reading are first evaluated experimentally. The dose response of the ionisation chambers and solid state detectors of interest, as simulated using PENELOPE or measured with the aid of electromagnets, will then be analyzed for gross trends. The ionisation chamber trends will be linked to previously postulated electron path length and electron number arguments for the dose response of ionisation chambers<sup>1</sup>. The mechanisms of dose response regarding the solid state detectors will be analyzed under the removal of key materials. Further, the results for solid state detectors as simulated in the water tank will be presented, and compared to both the dose to water at the detector positions, and the relative response in air. The CC13 chamber will additionally be investigated in a water tank, and its use in beam scanning will be evaluated. Finally, the experimental findings of the OSL detectors will be evaluated.

## 4.1 Ionisation Chambers

### 4.1.1 $k_Q$ , Field Size, $P_{ion}$ , and $P_{pol}$ Measurements

This section will examine the  $k_Q$ , field size,  $P_{ion}$ , and  $P_{pol}$  measurements referred to in chapter 3. The field size measurements represent measurements made in different incident photon field sizes, hence in different scattered radiation circumstances. The remaining three parameters,  $k_Q$ ,  $P_{ion}$ , and  $P_{pol}$  are corrections in the TG-51 formalism which account for beam quality, ion recombination, and polarity effects

respectively<sup>2</sup>. The results of the  $k_Q$  simulations are provided in Table 4.1 along with the previously determined values<sup>2, 3</sup>. The simulated  $k_Q$  values for both chamber models matched the literature values closely. These results, in addition to the measurement verifications of presented data, confirm the accuracy of the chamber models employed. Additionally, the change in dose response as a function of magnetic field strength remains unchanged through the investigated field sizes, and matches the simulated results within 1%, as presented in Table 4.2 below. This was expected, as the dose response is relative, and any effect field size has on dose deposited – through a change in the amount of scattered radiation – would have disappeared in taking the ratio; thus, so long as all of our results employ the same field (and electron equilibrium exists), the exact size of the field is of little concern. These relative field size results give credence to the use of the Sheikh-Bagheri *et al* (2002)<sup>4</sup> square field spectra in this instance.

It was found that  $P_{ion}$  and  $P_{pol}$  values remained unchanged within measurement error from 0.0 T to 0.09 T and 0.14 T. The magnetic field appears not to have any effect on ion collection efficiency at these lower field strengths. The numerical results of the  $P_{ion}$  and  $P_{pol}$  measurements are presented in Table 4.3 below. Unsurprisingly, the vast majority of the gross chamber response appears to originate from factors outside  $P_{ion}$  and  $P_{pol}$ . These factors are not expected to change appreciably with increasing magnetic field strength, as the electric potential driving the collection of these charges is far greater than the magnetic force experienced by the majority of the charges produced in the detectors.

Chamber	TG-51 $k_Q$ Values <sup>2</sup>	Previous $k_Q$ MC study <sup>3</sup>	Simulated $k_Q$ values
NE Technology ltd NE2571	0.995	0.992	0.990 ( $\pm 0.04$ )
Capintec PR06C	0.994	0.994	0.991 ( $\pm 0.02$ )

Table 4.1 Chamber  $k_Q$  values without the magnetic field are compared with the previously published results. Errors quoted are 1 standard deviation.

Field Strength (T)	2cmx2 cm Ratio	3cmx3 cm Ratio	4cmx4 cm Ratio	5cmx5 cm Ratio	7cmx5 cm Ratio	10cmx5 cm Ratio	Simulated 10cmx10 cm Ratio
<b>0.08</b>	1.0030	1.0024	1.0029	1.0025	1.0030	1.0025	1.0033
<b>0.14</b>	1.0060	1.0056	1.0058	1.0053	1.0059	1.0060	1.0057

Table 4.2 Ratio of readings with the magnetic field indicated to no magnetic field as a function of field size. All measured values are  $\pm 0.02\%$

Field Strength (T)	$P_{ion}^5$	$P_{ion}^2$	$P_{pol}^2$
<b>0</b>	1.0021	1.0023	1.004
<b>0.09</b>	1.0021	1.0023	1.004
<b>0.14</b>	1.0027	1.0029	1.005

Table 4.3  $P_{pol}$  and  $P_{ion}$  values as a function of magnetic field. Calculation formalism used as per column reference. All values are  $\pm 0.02\%$

#### 4.1.2 NE2571

Figures 4.1 and 4.2 present the dose response of the NE2571 chamber as a function of magnetic field strength. The results from the Monte Carlo

simulations in orientations I-IV and from the measurements made by Meijnsing et al (2009) in orientations I and II are shown.

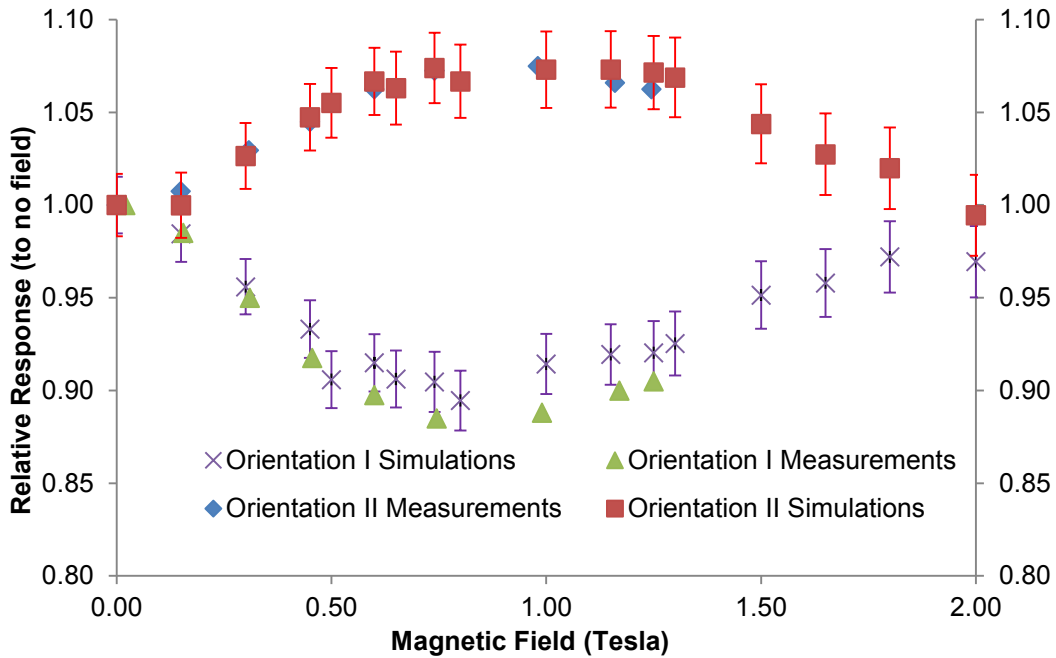


Figure 4.1 NE2571 relative dose deposited as a function of magnetic field in orientations I, II as determined in Monte Carlo simulations, and orientations I and II as determined in the measurements previously published by Meijnsing *et al* (2009)<sup>1</sup>.

In orientation I, the simulated response first decreases to a minimum of 0.89 at 0.8T and climbs slowly back toward 1.0 at further increasing magnetic field strengths. The response exhibited in the orientation II simulations shows the opposite trend, increasing slowly to a maximum of 1.07 at 1.0 T before further decreasing towards 1.0 at higher magnetic field strengths. There is good agreement between measurement and simulation results in orientation II at the field strengths where measurements are available; simulations and measurements differ on average by 0.45%. The simulations in orientation I agree within 1% up to magnetic field strengths of 0.45 T, however, the simulated data exhibits a slightly higher dose response than the measurements at field strengths beyond 0.45 T; simulations and measurements at field strengths over 0.45 T in orientation I differ an average of 2.1%. These differences are most likely due to the

approximations allotted to the simulation geometry in the interest of simulation speed, namely the lack of a conical tip or stem on the ion chamber. Deviations in these orientations have also been discussed by the Meijsing group with respect to measurement setup<sup>1</sup>. Specifically, small rotational errors, on the order of a few degree with respect to the primary photon direction, were found to have significant implications in measured dose response, especially at higher magnetic field strengths. The simulated histories in orientations I and II were run until the error bars would match the Meijsing et al simulated results<sup>1</sup>. No previously simulated or measured data was available to match for orientations III and IV, so histories were run until the standard deviation of the error in the simulation was near 0.5%.

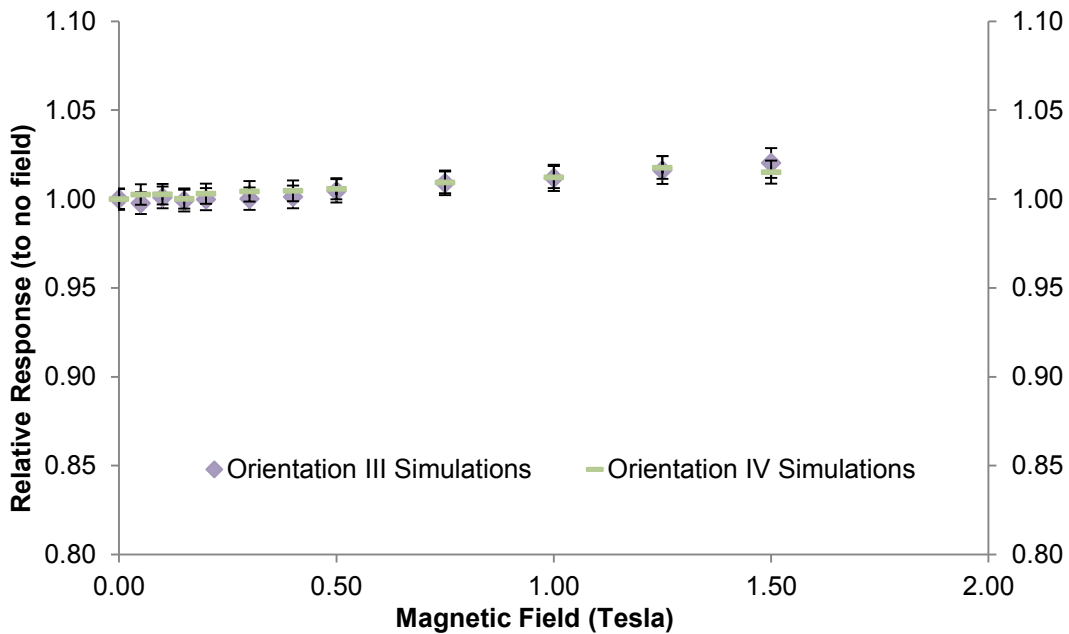


Figure 4.2 NE2571 relative dose deposited as a function of magnetic field in orientations III, IV as determined in Monte Carlo simulations, please note the simulation data points nearly lie on top of each other.

The dose response of the chamber in magnetic field has been previously related to the nature of electron tracks within the chamber cavity. The response can be directly coupled to both the number of electrons, and average track length of the electrons within the air cavity of the chamber

itself<sup>1</sup>, as follows: As the magnetic field increases, the electrons, under the influence of the Lorentz force, have an increasingly curved path within the chamber volume<sup>1</sup>. In orientation II the Lorentz force bends the electrons towards the long axis of the chamber, which increases the average electron track length within the chamber initially. For a given electron energy, beyond a certain magnetic field strength, the path length of the electrons in the chamber will begin to decrease as they are bent out of the anterior face of the chamber. While in orientation I the electron trajectories tend to curve outside of the volume of the chamber due to the Lorentz force, decreasing track length within the chamber initially. At certain magnetic field strength, which depends on the energy of the electrons, the electrons will be able to complete a larger portion of their curved path within the chamber, and the path length will increase again. Electrons outside of the chamber also have their path altered by the magnetic field, and can be curved into the chamber as shown by previously investigated point spread kernels<sup>1</sup>. In orientation I, the electrons leaving the chamber have been found to balance those entering the chamber, while in orientation II the total electron number has been found to decrease steadily. The dose deposited in a medium by electrons is dependent on the number of electrons, and the average length of their track within the medium; the product of the electron number and average track length in the ionisation chamber was shown by Meijnsing *et al* (2009) to follow the observed NE2571 dose response trend to first order.

Orientations III and IV show little change in response with increasing magnetic fields. There is less than 1% change in dose response up to field strength of 1.0 T for both orientations. After this point the response slowly increases to near 1.02 at the highest field strength simulated (1.5 T). This relatively small response was expected, as electrons are being focused along the magnetic field lines in orientations III and IV, as opposed to being deflected outside of the chamber in orientations I and II. This focusing effect will tend to maintain electronic equilibrium<sup>6</sup>, and prevent electrons from

travelling increased or decreased lengths within the detection volume; thus allowing dose response to remain unchanged.

### **4.1.3 PR06C**

Figure 4.3 shows the Monte Carlo simulation results of the PR06C chamber in orientations I-IV, and figure 4.4 the measurement results in orientations I and II. The observed response exhibits nearly identical trends to the NE2571 chamber, as was expected due to the similarities in chamber geometries. The simulated response for orientation I was found to decrease to a minimum of 0.91 at 0.8 T before increasing slowly towards 1.0 with increasing magnetic field strengths. The simulated results for orientation II showed an increase to a maximum of 1.08 at 1.0 T before decreasing towards 1.0 at higher magnetic field strengths. This behaviour was expected due to the similarities in chamber design to the NE2571, and is a consequence of the electron number and electron paths discussed above. The transverse field (orientations I and II) measurements made with this chamber match the simulated results very closely (0.2% average difference), and verify the simulations of orientation I and II to a field strength of ~0.21 T. We expect that if measurements could be made at higher field strengths they would follow the simulations closely, which is suggested by the NE2571 measurement trends.

Figure 4.3 also shows that orientations III and IV have a nearly identical response to the NE2571 chamber. This result was also expected due to similarities in chamber design. The data for orientations III and IV both show relative responses of less than 1.01 up to 1.0 T, before increasing slowly to 1.02 at 1.5 T. The results of the longitudinal field measurements of the PR06C ionisation chamber are presented in figure 4.5. This figure contains both the orientation III and IV measurements at low field longitudinal

magnetic fields, and the simulation data of the PR06C in orientations III and IV.

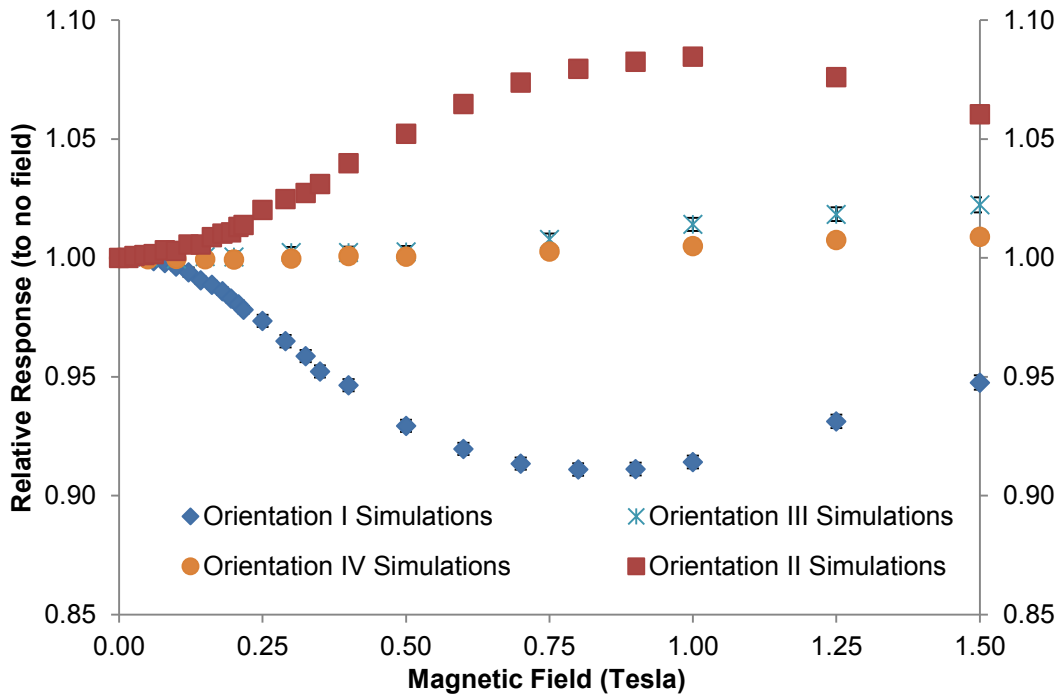


Figure 4.3 PR06C simulated relative dose deposited as a function of magnetic field in orientations I-IV

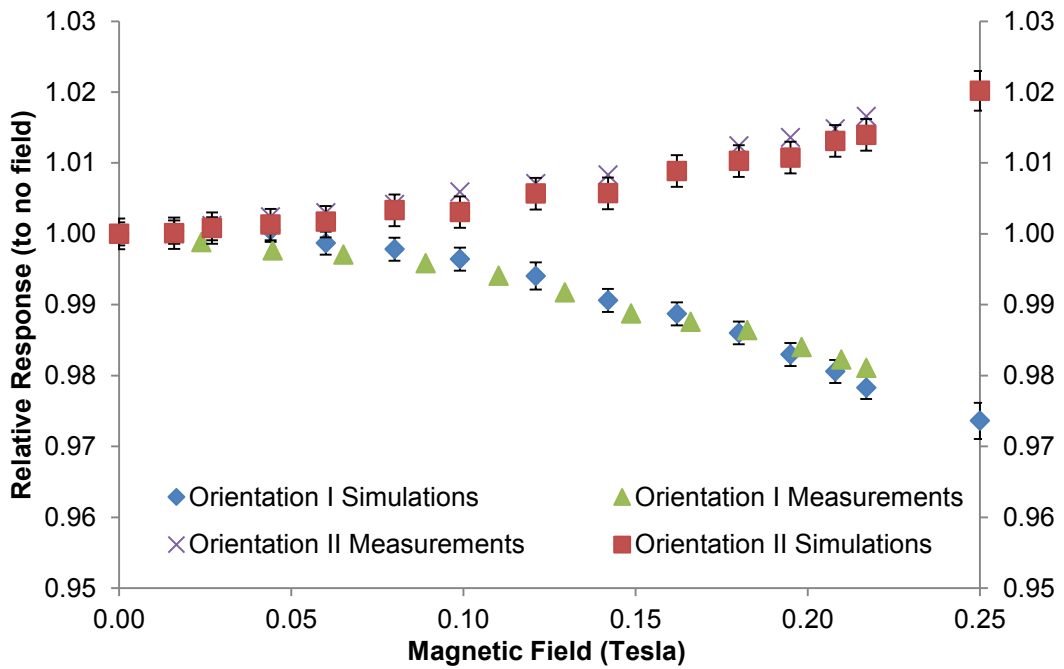


Figure 4.4 Measured and simulated relative dose response of the PR06C ion chamber as a function of transverse magnetic field strength

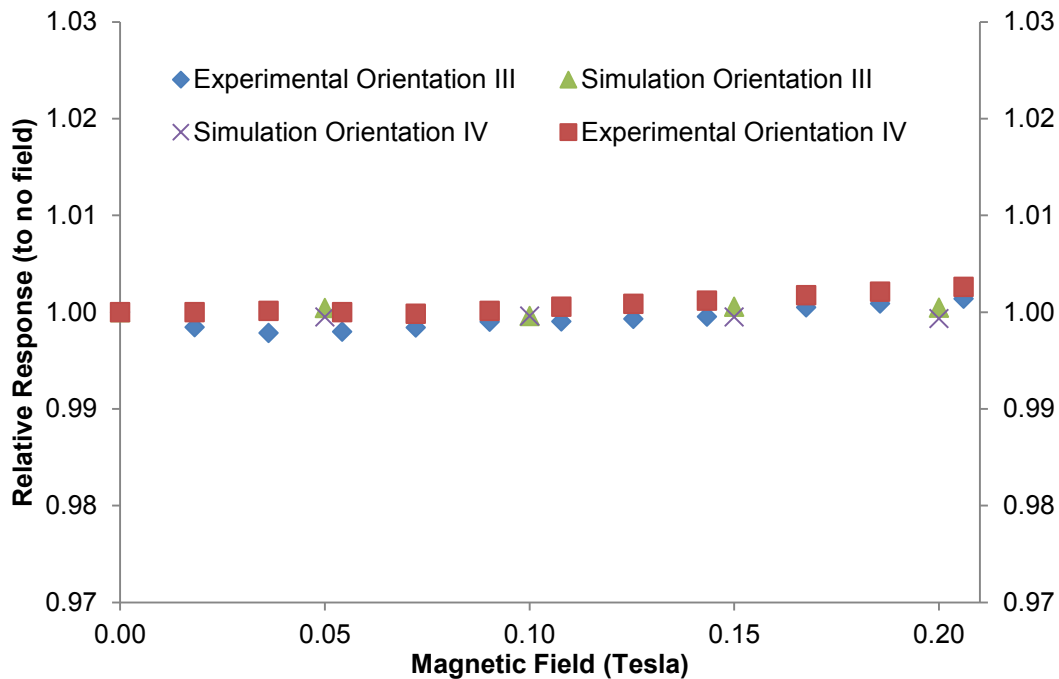


Figure 4.5 Measured and simulated relative dose response of the PR06C ion chamber as a function of longitudinal magnetic field strength

The maximum observed difference from 1.0 in the ratio of doses without magnetic field to with magnetic field is near 0.3%. The statistical uncertainty in the simulation data sets was  $\sim 0.25\%$ , while the spread in the measurements was  $\sim 0.1\%$  to  $\sim 0.2\%$ . Both the measurements as well as the simulated values never stray far from a ratio of 1.0. Moreover, it is likely that the observed deviances between the measurements and simulated data are merely statistical anomalies, as the difference between measurement and simulation are in all cases smaller than the combined standard deviation. Specifically, the orientation III and IV measurements for the PR06C detector appear to rise slightly at 0.2 T. This may be evidence of a weak trend with increasing magnetic field, but the absolute deviation is too small compared to the variance to form any strong conclusions. The measurements suggest that there is no appreciable magnetic field dose response at field strengths up to  $\sim 0.21$  T in longitudinal magnetic field configurations. Further, these

measurements validate the low field orientation III and IV simulations, giving credence to the validity of the higher magnetic field simulation results.

#### **4.1.4 A12**

Please note that this chamber was simulated in water at a depth of 10 cm in a 10 x 10 cm<sup>2</sup> field size to simulate the beam calibration geometry as adopted in TG-51 protocol of the AAPM<sup>2</sup>. Shown in figure 4.6 are the simulated results of the A12 chamber in orientations I-IV. As expected, it too exhibits nearly identical response to both the PR06C and NE2571 ionisation chambers. The response for orientation I decreases to a minimum 0.91 at 0.8 T before slowly increasing towards 1.0 with higher magnetic fields. In orientation II the response increases to a maximum of 1.07 at 0.8 T before decreasing towards 1.0 at higher field strengths. Again this behaviour was expected due to similarities in chamber design to the NE2571 and PR06C, and similar reasoning pertaining to electrons can be applied. Errors in this simulation data are larger than the PR06C simulations owing to the decreased efficiency of scoring the dose in the chamber within the TG51 geometry, namely the large field size and water tank. We would expect any measurements made to match simulated data, since the simulated response closely matches that of the other chambers, whose results have been verified to some extent by measurements.

Simulation results for orientations III and IV again show nearly identical response to the previous two chambers. Orientations III and IV both exhibit relative responses of less than 1.01 up to 1.0 T, and show a slowly increasing response to 1.02 at 1.5 T. Once more, because of the similarities between the three chambers investigated, these results are expected.

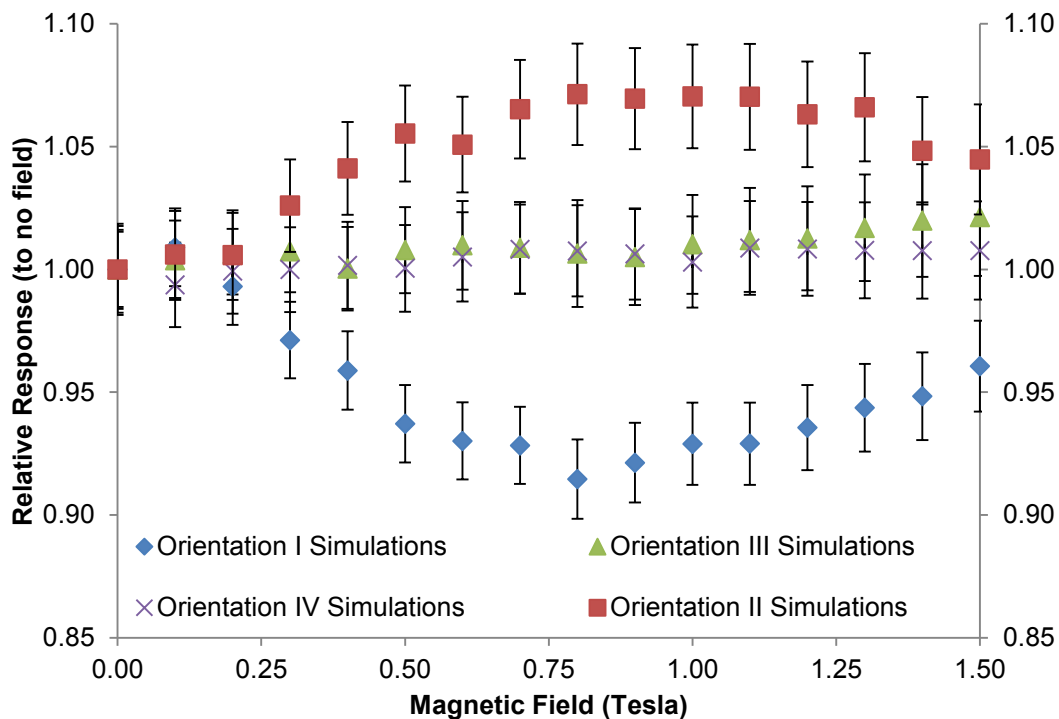


Figure 4.6 A12 simulations of relative dose deposited as a function of magnetic field in orientations I-IV

## 4.2 Solid State Detectors

### 4.2.1 PTW60003 Diamond Detector

Figures 4.7 and 4.8 depict the Monte Carlo simulated dose response for the PTW 60003 Diamond Detector in all orientations. Figure 4.9 depicts the simulations and measurement dose responses for 3 transverse field orientations (orientations I, II, and II-2). Figure 4.10 shows the difference in simulations with and without the air gap (figure 3.5 A as compared to 3.5 C) to illuminate mechanisms of the observed dose response. It should be noted that orientations III and IV are excluded from figure 4.10. The orientation III and IV results with and without the air gap are nearly identical, and their removal aided readability of the figure.

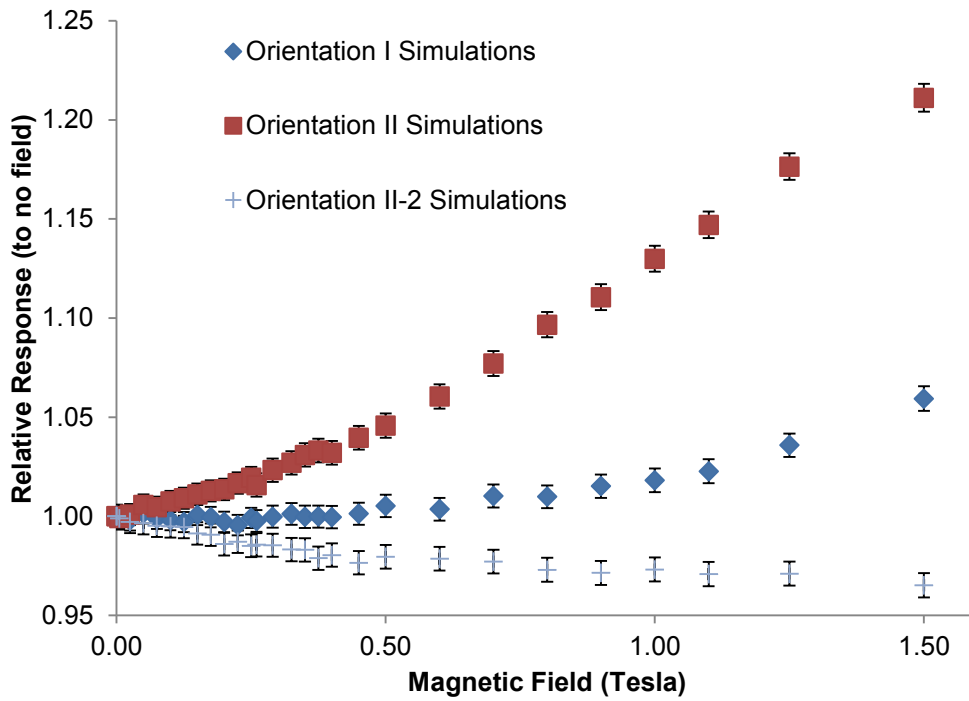


Figure 4.7 Monte Carlo generated dose response of the PTW60003 diamond detector as a function of magnetic field strength, error bars are  $\pm 1$  standard deviation

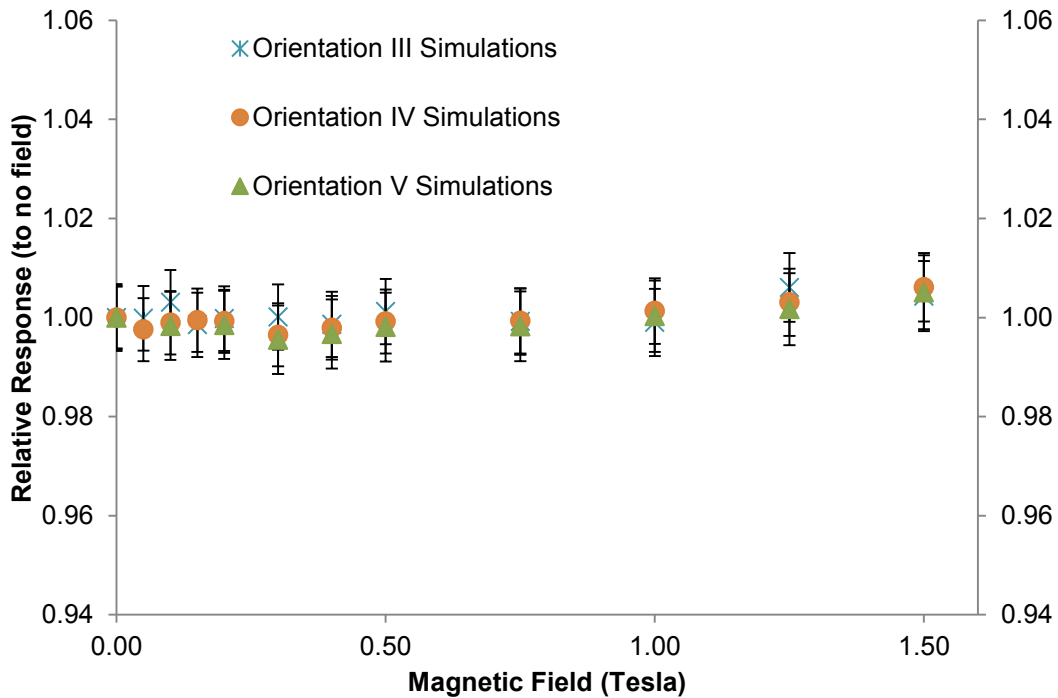


Figure 4.8 Monte Carlo generated dose response of the PTW60003 diamond detector as a function of magnetic field strength, error bars are  $\pm 1$  standard deviation

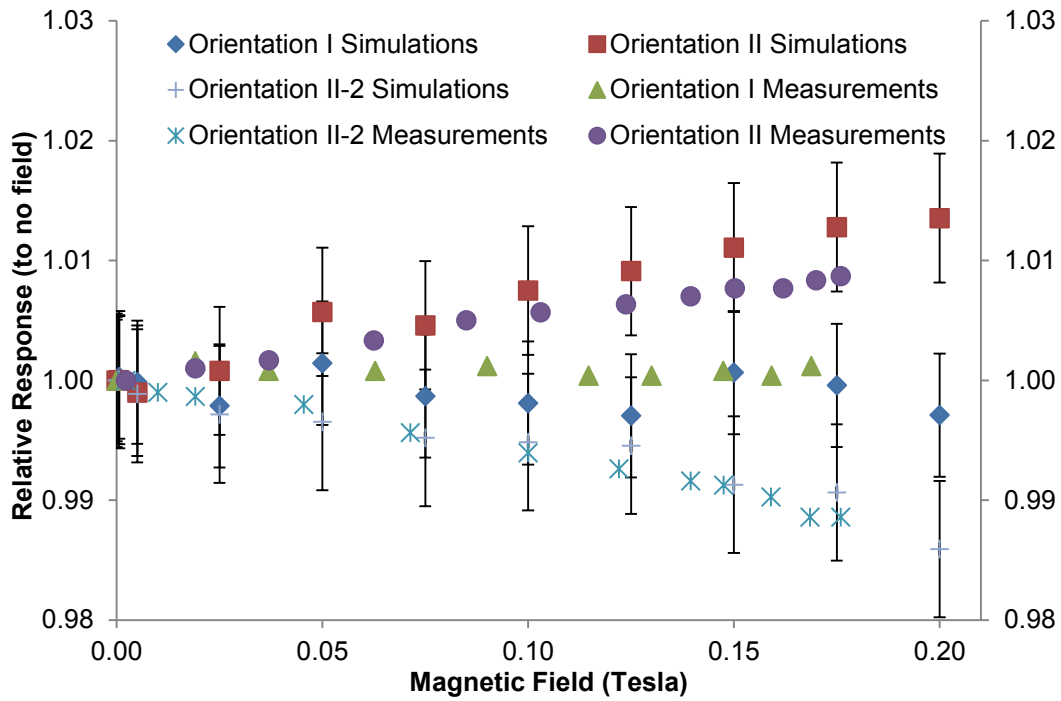


Figure 4.9 Monte Carlo generated dose response of the PTW60003 diamond detector compared to measurements as a function of magnetic field strength, error bars are  $\pm 1$  standard deviation

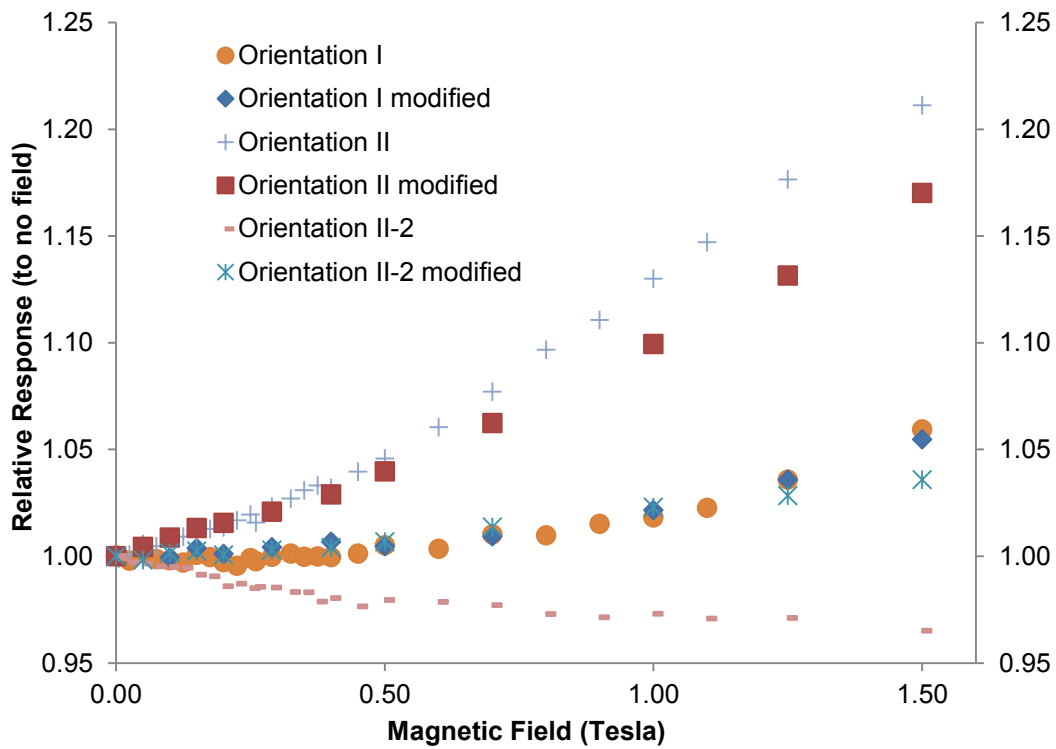


Figure 4.10 Comparison of the PTW 60003 diamond detector original build (figure 3.5A) to the modified build (figure 3.5C, labelled "modified"), average standard deviation of simulation points for the "modified" build is 0.70%

The PTW60003 detector simulations have an average standard deviation of uncertainty of  $\pm 0.65\%$  for all orientations. The simulated dose responses for orientations III and IV as presented in figure 4.8 are nearly the same; both orientations exhibit a slight upward trend with the relative response approaching 1.005 (0.5%) at 1.5 T, which is less than one standard deviation of simulation uncertainty. A similar response in these orientations was also found for ion chambers. Orientation V also exhibits little change as a function of magnetic field strength, showing a possible slight increase in dose response (1.006) towards 1.5 T. This was expected, as the regions surrounding the detection volume are radially symmetric in the direction of electron curvature in this orientation, meaning electrons will see little to no difference with and without a magnetic field.

The dose response in orientation I does not change much up to 0.5 T transverse magnetic field; however, thereafter it increases slowly to 1.06 at 1.5 T. The mechanism for this behaviour is likely the electron return effect, where above 0.5 T, electrons entering the polystyrene curve back and re-enter the diamond and deposit energy in the active volume of the detector. Replacing air gap with polystyrene does not appear to be of consequence to this dose response, as is evident in figure 4.10. In figure 4.9 we see that the transverse field measurements made in all orientations follow the simulated results, staying near 1.0 in orientation I, rising to near 1.01 in orientation II and falling to near 0.99 in orientation II-2 at  $\sim 0.18$  T. The transverse field measured data points generally do not stray far from the simulated data. There is a clear rise, fall, or null result through low field strengths in the measured data, depending on the orientation considered. The average spread in the transverse field measured data points is  $\pm 0.4\%$ . It can be seen that these measurements agree with the simulations within 0.5% through all measured field strengths. Given the good comparison between these measured and simulated results, it could be suggested that the simulations accurately model the detector, and had measurements with

higher magnetic fields been possible, the agreement between the measured and simulated values would remain.

The orientation II and II-2 responses are opposite of each other. The orientation II simulation shows a sharp rise in dose response as a function of magnetic field, reaching higher than 1.20 at 1.5 T. In this orientation the electrons incident on the active volume are first curved through the internal detector components situated nearer the stem (from left to right in figure 3.5 A). The active volume of the diamond detector is a thin circular slab, and as secondary electrons are curved via the Lorentz force, those incident on the active volume see a larger, more circular cross section of the active volume, rather than a thin disc of diamond on edge leading to an increased dose response. Additionally, electrons entering the air gap are able to freely follow their curved trajectories, and are bent towards the active volume of the detector increasing the number of electrons incident. As seen in figure 4.10, these electrons originating from the air gap region contribute to the increased dose response, but are not the sole cause of the response, as evidenced by the rise in dose response as a function of magnetic field without the air gap present. Orientation II measurements are generally of lower dose response than the simulations, however, they are still within 0.5% deviation from the simulated values. The closeness of the measured and simulated data suggests that this orientation is simulated accurately, and higher magnetic field strengths are likely to represent the actual behaviour of the detector.

The diamond detector orientation II-2 case exhibits a different response than the orientation II results. Where in orientation II there is a sharp rise in dose response, the orientation II-2 trend is a slow decrease in dose response, trending towards 0.97 at 1.5 T. The orientation of the detector in the II-2 case is actually mirrored to that shown in figure 3.5 A. Although the curving of electrons due to magnetic field is in the same direction with respect to the magnetic field as in orientation II, the electrons will appear to

curve from right to left with respect to the internal structure of the diamond shown in figure 3.5 A. It is true that in this orientation the electrons incident on the active volume of the detector see an increasing cross sectional area as was the case for orientation II. This increase in cross sectional area seen would tend to increase dose response as more electrons are incident on the detection volume, but this is not what the simulations would suggest. It appears that the effect of air pocket in the detector structure dominates the observed response. Figure 4.10 shows that the decrease in response is due to the electrons in this orientation entering the air gap and curving away from the active volume of the detector via the Lorentz force, thus decreasing the energy deposited in the active volume. It is evident that the bending away of the electrons due to the presence of the air gap has a larger impact on the total dose response than the increasing cross sectional area, yielding an overall decrease in dose response as a function of magnetic field strength. When the air gap is replaced by the polystyrene (figure 3.5 C), the dose response increases slightly due to the increase in the apparent cross-section of the active volume. Measurements in this orientation are seen to follow the simulation results within 0.3%, and again support the accuracy of the detector modelling.

The results of the longitudinal field measurements for the PTW60003 diamond detector are presented in figure 4.11. This figure contains both the orientation III and IV measurements at low field longitudinal magnetic fields, and the simulation data of the PTW60003 in orientations III and IV. The maximum observed difference from 1.0 in the ratio of doses without magnetic field to with magnetic field is near 0.4%. The uncertainty in the simulation data sets was 0.7%, and the spread in the measurements was ~0.2% to ~0.4%. Both the measurements as well as the simulated values never stray far from a ratio of 1.0. Moreover, it is likely that the observed deviances from 1.0 are merely statistical anomalies, as the deviances are small and well within the margin of uncertainty. Specifically, the orientation III measurements for the PTW60003 detector appear to fall near 0.2 T. This

may be evidence of a weak trend with increasing magnetic field, but the absolute deviation is too small compared to the variance to form any strong conclusions. The measurements suggest that there is no appreciable magnetic field dose response at field strengths up to near 0.21 T in longitudinal magnetic field configurations. Further, these measurements validate the low field orientation III and IV simulations, giving credence to the validity of the higher magnetic field simulation results.

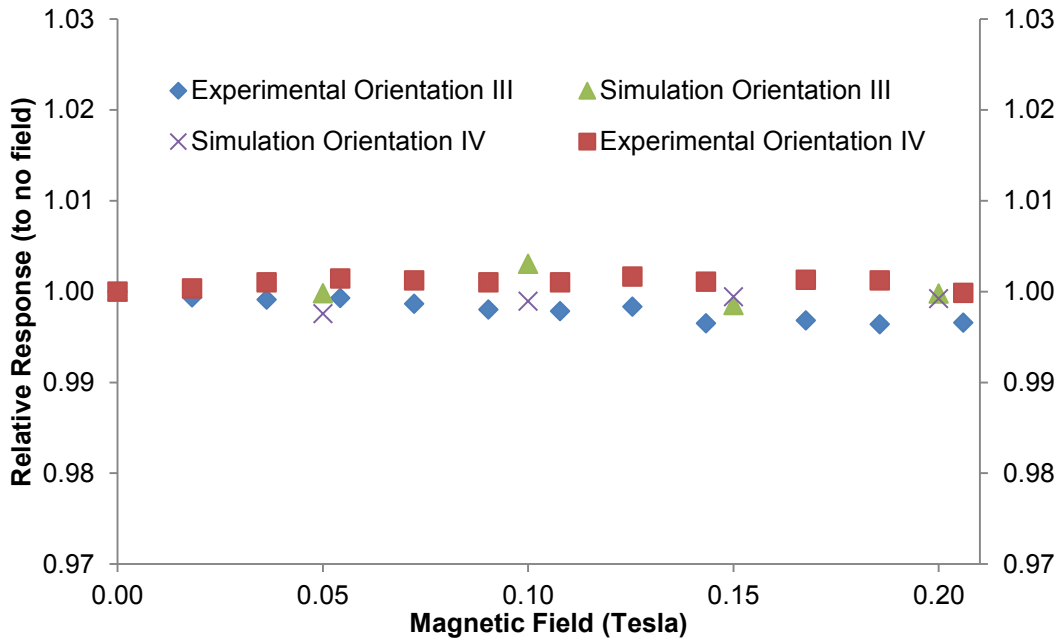


Figure 4.11 Measured and simulated relative dose response of the PTW60003 diamond detector as a function of longitudinal magnetic field strength

## 4.2.2 IBA PFD Diode Detector

Figures 4.12 and 4.13 depict the Monte Carlo results for the IBA PFD Diode Detector in all orientations. Figure 4.14 depicts the simulations and measurement quantities for the transverse field orientations. Figure 4.15 presents the difference in simulations with the change in detector materials implemented (figure 3.5 B as compared to 3.5 D) to illuminate mechanisms of the observed dose response. It shall be noted that orientations III and IV are excluded from figure 4.15 as for the PTW60003.

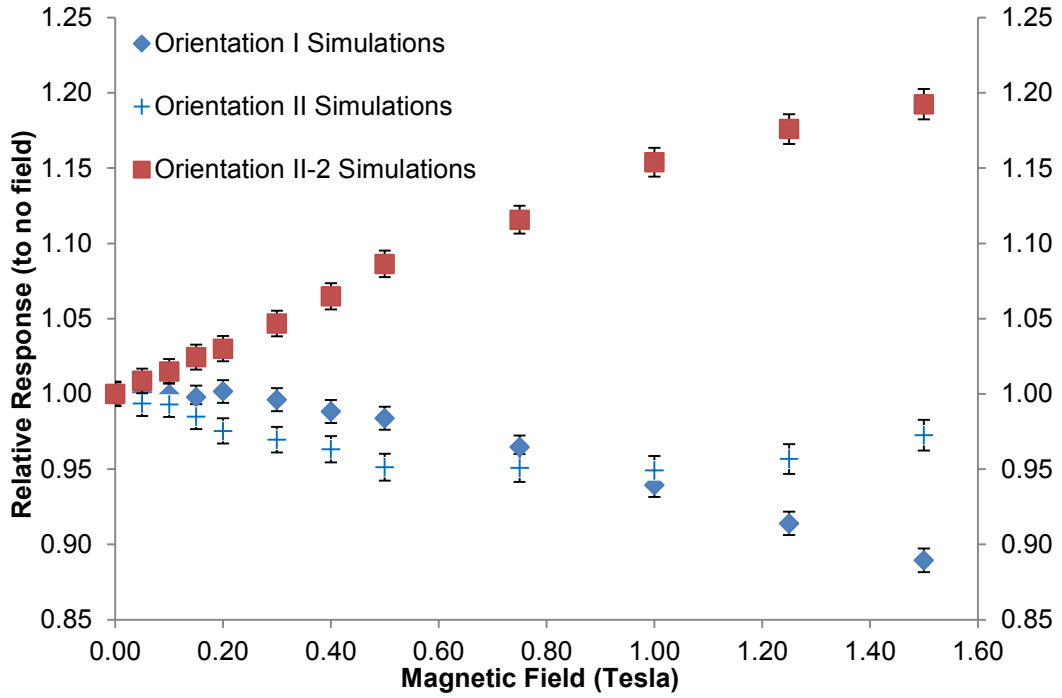


Figure 4.12 Monte Carlo generated dose response of the IBA PFD diode detector as a function of magnetic field strength, error bars are  $\pm 1$  standard deviation

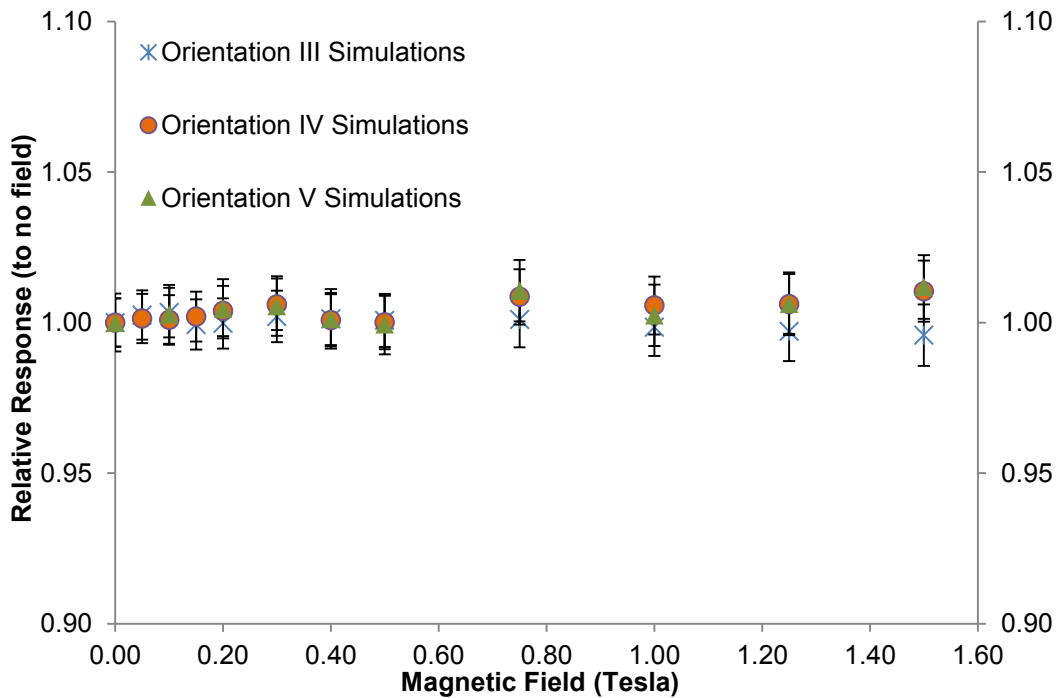


Figure 4.13 Monte Carlo generated dose response of the IBA PFD diode detector as a function of magnetic field strength, error bars are  $\pm 1$  standard deviation

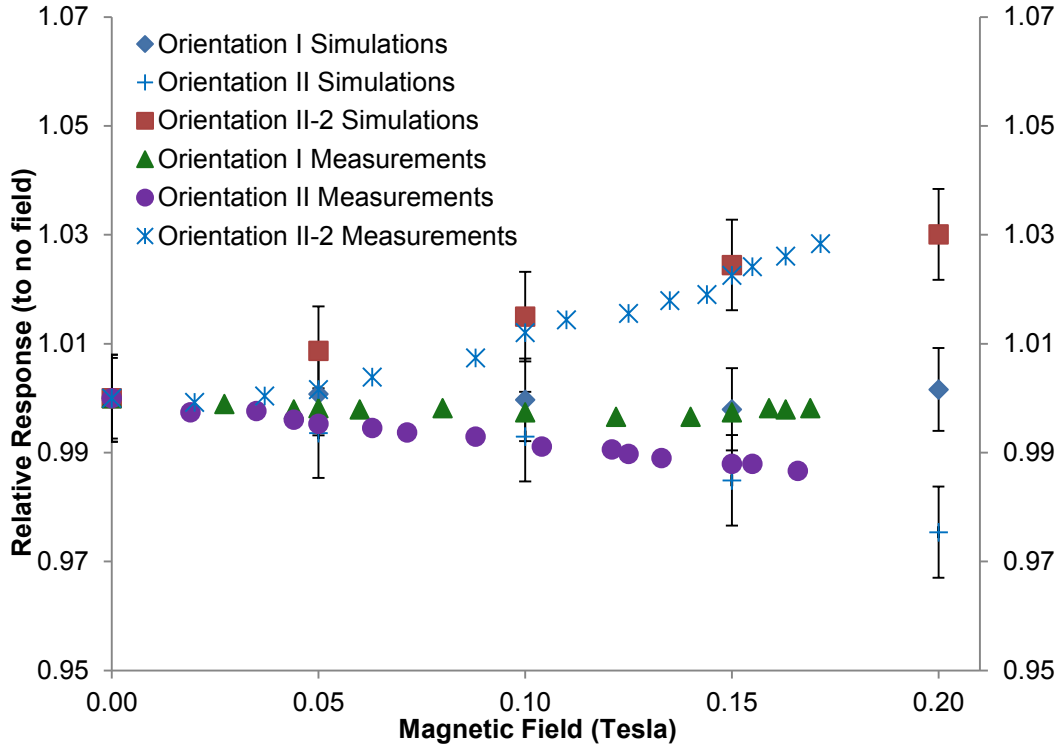


Figure 4.14 Monte Carlo generated dose response of the IBA PFD diode detector compared to measurements as a function of magnetic field strength, error bars are  $\pm 1$  standard deviation

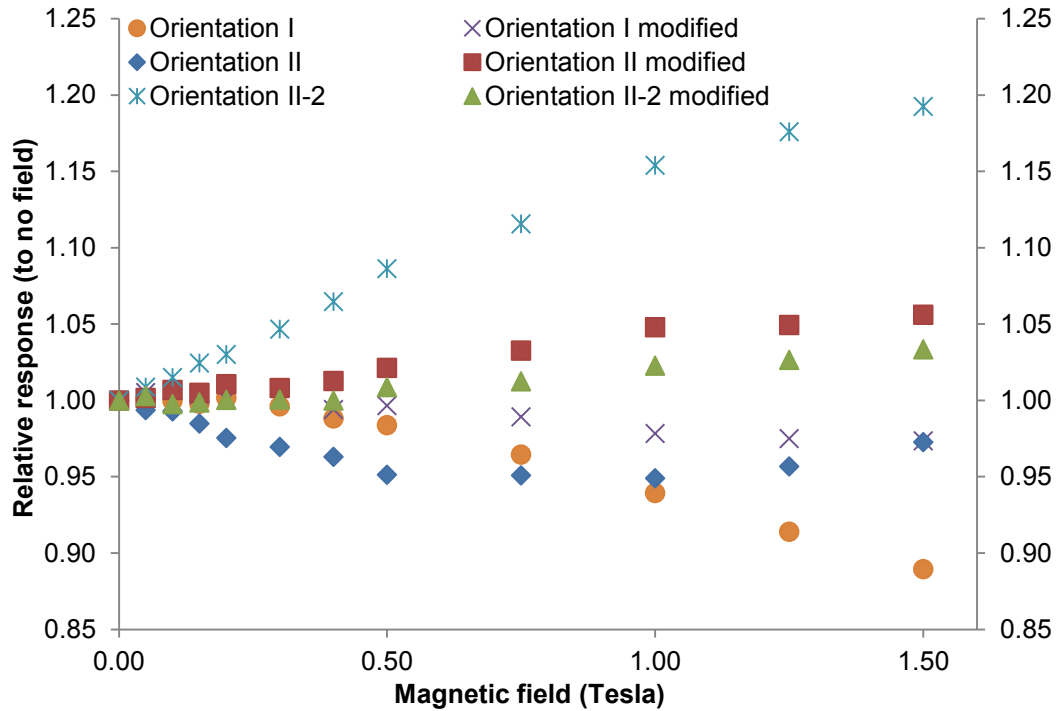


Figure 4.15 Comparison of the IBA PFD diode detector original build (figure 3.5B) to the modified build (figure 3.5D, labelled "modified"), average standard deviation of simulation points for the "modified" build is 0.98%

The IBA PFD diode detector simulations have an average standard deviation of  $\pm 0.85\%$  for all orientations. The simulated responses for orientations III and IV as presented in figure 4.13 nearly lie on top of one another, and exhibit a slight upward trend with a relative response approaching 1.01 (1%) at 1.5 T. This kind of response was not unexpected, and was found to be the same for the PTW 60003 diamond detector, and selected ion chambers. Again, a similar response to orientations III and IV was found for orientation V, which is the same behaviour as was found for the PTW 60003. The largest change in the response of 1.017 occurs at the largest magnetic field strength of 1.5 T. This was expected as the diode detector is also radially symmetric about the detection volume in the direction of electron curvature in this orientation.

The relative dose response of the diode detector in orientation I decreases at an increasing rate as magnetic field strength is increased. In this case the Lorentz force tends to curve electrons laterally from the buildup material through the internal detector components, namely the tungsten shielding, towards the active volume of the detector (through the plane of the page in figure 3.5 B). The diode detector's response is predominantly affected (as seen in figure 4.15) by the presence of the cylindrical tungsten shield along the long axis of the detector. The curved electrons encounter the encapsulating tungsten and are removed from the beam, thus resulting in lower dose. When the tungsten shield is replaced by polystyrene, the dose response is increased slightly, as electrons are no longer being attenuated by the tungsten shield (figure 4.15). Transverse magnetic field measurements shown in figure 4.14 hover around the 1.0 relative response mark for orientation I, rise to near 1.03 in orientation II-2, and fall to near 0.99 in orientation II, at  $\sim 0.18$  T. The measurement points follow the simulated data closely at these low magnetic field strengths for orientations I and II. Measurements in orientation II-2 start out 0.5% low until near 0.1 T, where they match more closely (0.2%) through the higher field strengths. Although there is a difference in the degree of agreement of the

measurements and simulations below and above 0.1 T, all measurement points are within simulation statistical uncertainty. The average error in the measurements was  $\pm 0.3\%$ , and their values match the response seen in the simulations within 0.5% up to the highest measured field strength. From the transverse magnetic field measured data, it is clear that in these low field strengths the simulation accurately models the dose response. It is not unreasonable to assume that measurements done at higher field strengths would also agree with the simulations.

In orientation II-2 electrons incident on the active volume of the diode detector will be curved via the Lorentz force through the laterally situated buildup material, from left to right in figure 3.5 B (as presented with the Lorentz Force from left to right, figure 3.5 B is orientation II-2). Unlike in the same orientation with the PTW 60003 diamond detector, there is a monotonic rise in dose response as a function of magnetic field strength, up to a relative response of 1.2 at 1.5 T seen in figure 4.12. This is because the active volume of the diode detector is a thin disc, geometrically similar to the diamond detector. As the magnetic field increases, the electrons curve more, and the detection volume cross section seen by the curved electrons incident increases, leading to an increased dose response. This differs from the diamond detector in that there is no air gap giving rise to a dominating loss of scattered radiation from the stem side of the detection volume. Figure 4.15 shows that upon removal of the tungsten shield, the relative response is somewhat lower than with the shield. This can be easily explained by looking at the zero magnetic field cases of both detector constructions. In the zero field case, electrons still must travel through tungsten to reach the active volume in the original design; where in the modified design the tungsten is absent (giving a larger zero field reading). Because the results are normalized to this measurement in each case, it is clear that without the tungsten shield, the larger baseline measurement (no magnetic field) will decrease relative response with increasing field strengths. Orientation II-2 measurements are generally of a lower, if not the

same dose response when compared to the simulations; they are well within 0.5% deviation from the simulated values. The closeness of the measured and simulated data suggests that this orientation is simulated accurately, and higher magnetic field strengths are likely to represent the actual behaviour of the detector, as was the case for the PTW60003.

As seen in figure 4.12, the relative dose response of orientation II decreases slowly to 0.95 at 1.0 T, then rises slowly to 0.97 at 1.5 T. Although the increasing detection volume cross section seen by the curved electrons (electrons travel from right to left in figure 3.5 B) is true for orientation II, we must also consider the materials the electrons incident on the detector must travel through. As seen in figure 4.15, the tungsten encapsulation again has a noticeable effect on dose response, as was the case for orientation I. This encapsulation will remove more of the electrons that traverse it compared to the other materials present, so fewer are available to interact with the detection volume. This removal of electrons tends to decrease the dose response, and is initially a larger effect than the increasing cross section seen by the curved electrons. After 1.0 T the individual response of the increasing cross sectional area begins to increase relative to the removal of beam by the tungsten, and the total relative response increases from a minimum. This response differs from the sharp rise seen in the diamond detector due to the differences in construction materials, namely the tungsten shielding of the diode, and air gap in the diamond detector. Measurements in this orientation are seen to follow the simulation results within 0.5%, and again support the accuracy of the detector modelling.

The results of the longitudinal field measurements of the IBA PFD diode detector are presented in figure 4.16. This figure contains both the orientation III and IV measurements at low field longitudinal magnetic fields, and the simulation data of the IBA PFD in orientations III and IV.

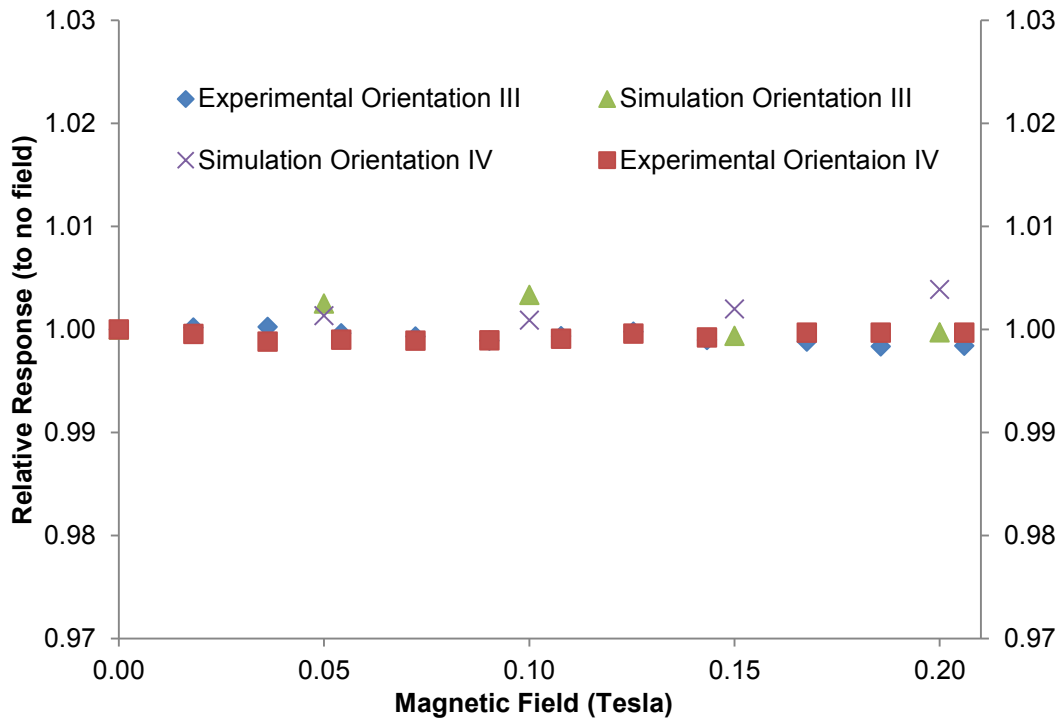


Figure 4.16 Measured and simulated relative dose response of the IBA PFD diode detector as a function of longitudinal magnetic field strength

The maximum observed difference from 1.0 in the ratio of doses without magnetic field to with magnetic field is near 0.4%. The uncertainty in the simulation data sets was 0.9%, and the spread in the measurements was ~0.1% to ~0.2%. Both the measurements as well as the simulated values never stray far from a ratio of 1.0. Moreover, it is likely that the observed deviances from 1.0 are merely statistical anomalies, as the deviances are small and well within the margin of uncertainty. The measurements suggest that there is no appreciable magnetic field dose response at field strengths up to near 0.21 T in longitudinal magnetic field configurations. Further, these measurements validate the low field orientation III and IV simulations, giving credence to the validity of the higher magnetic field simulation results.

## 4.3 Beam Scanning Simulations

### 4.3.1 Solid State Detectors

Figures 4.17 and 4.18 profile the water tank simulations of the diamond and diode detectors respectively, as compared to the relevant simulation results in air and water. It should be noted that only one of the orientation II (orientation II-2) geometries was simulated, orientation V was also omitted.

It is expected that the same trends with respect to the in air measurements will be observed in the remaining orientations while not near the periphery of the field. For reference, as discussed previously, secondary electrons in orientation II-2 (the simulated orientation) tend to curve from the tip of each detector towards the active volume and stem region, namely from right to left in figure 3.5 A and from left to right in figure 3.5 B.

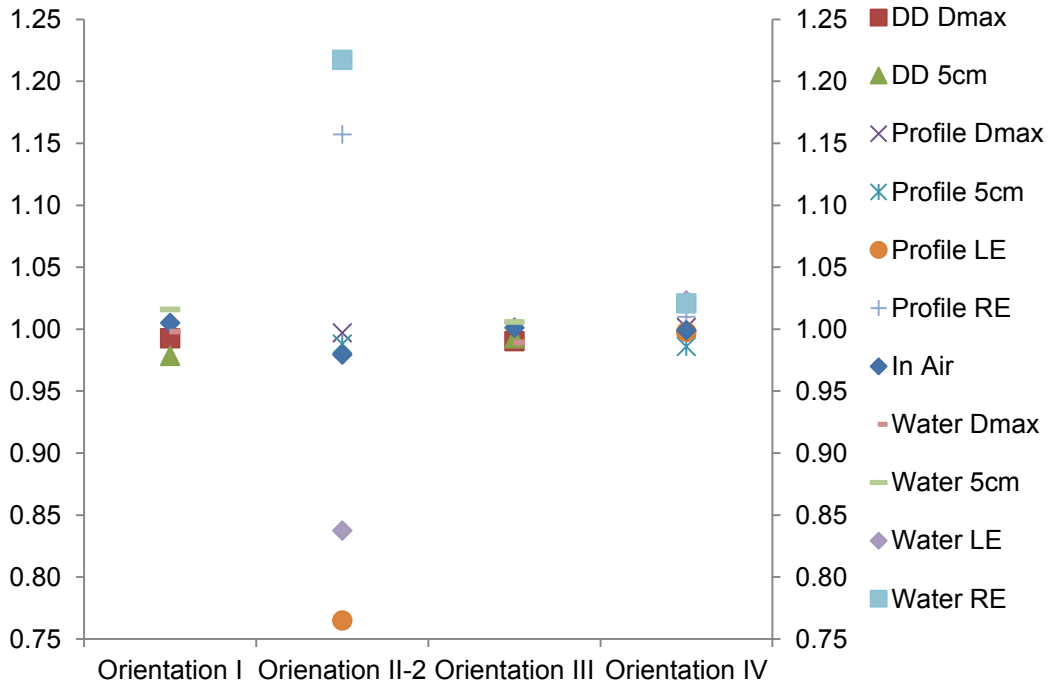


Figure 4.17 PTW60003 diamond detector simulations in air and a water tank, presented as the ratio of dose with to dose without magnetic field (0.5T). Water tank simulations are done in dose at depth (labeled DD, corresponding to orientations I and III depending on magnetic field direction) and profile scanning (labeled Profile, corresponding to orientation II-2 and IV depending on magnetic field direction) geometries, at Dmax, 5cm depth on the CAX, and 5cm depth at beam left (LE) and right (RE) edges (beams eye view). Ratio of dose to water, i.e. in the absence of detector, at all these points in the phantom are also presented.

It should be noted that not all detector positions were investigated for each orientation (i.e. beam profile simulations were not completed in orientations I or III). This is because the detector positions omitted are not typically used in the respective orientation for a given application. As such, the reader should be aware that a water tank simulation done in a particular detector position and orientation may not have a corresponding simulation in another orientation.

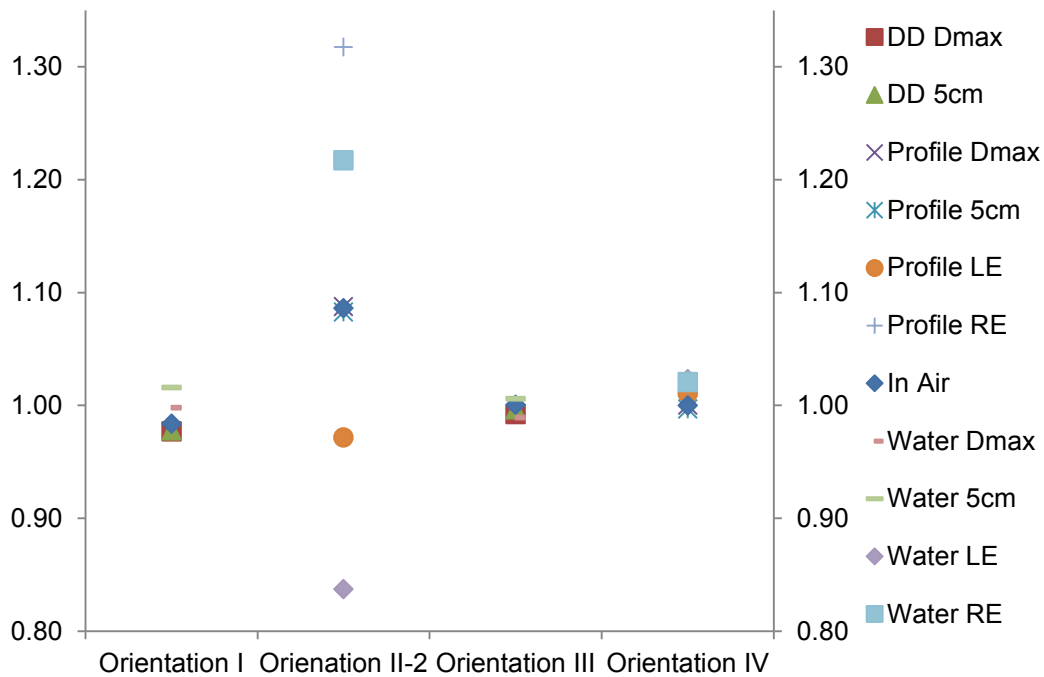


Figure 4.18 IBA PFD diode detector simulations in air and a water tank, presented as the ratio of dose with to dose without magnetic field (0.5T). Water tank simulations are done in dose at depth (labeled DD, corresponding to orientations I and III depending on magnetic field direction) and profile scanning (labeled Profile, corresponding to orientation II-2 and IV depending on magnetic field direction) geometries, at Dmax, 5cm depth on the CAX, and 5cm depth at beam left (LE) and right (RE) edges (beams eye view). Ratio of dose to water, i.e. in the absence of detector, at all these points in the phantom are also presented.

The uncertainty in the water tank simulations was  $\pm 3.5\%$  on average for the PTW60003 diamond detector simulations. The uncertainty for the IBA PFD diode detector was an average of  $\pm 4.0\%$ . The average uncertainty in the ratio of dose (with and without magnetic field) to water – at the point of detector simulation, in the absence of the detector – was 2.75% along the central axis, and 6.0% at the beam periphery. These uncertainties at the left

and right edges are larger than the uncertainties for the in air simulations due to the simulation geometry. The water tank itself is much larger than the active volumes of each detector scored for dose, each particle shower therefore takes much longer to track through the geometry, and is less likely to interact with the volume of interest. While the simulation uncertainty in the ratio of dose to the medium at the beam periphery is large, it is less than the difference between the dose response in water (with and without magnetic field), and dose response in the radiation detector in orientation II-2.

As can be seen in figure 4.17, the water tank and in air simulations for the diamond detector differ by up to 3% in all orientations when not at the edge of the beam. This could suggest a slight depth dependence on dose response; however, this deviance is still close to one standard deviation of the simulations, making an exact postulation impossible. We see that the dose response to water differs to that of the diamond detector in the water tank, as was expected. The dose response of the diamond detector for a given orientation at the water tank field strength (0.5 T) is represented by the difference between the normalized dose to the detector, and the normalized dose to water at this point. The dose response simulations at the left and right edge of the beam in the water tank with transverse magnetic fields (orientation II-2) vary drastically from the in air result (~20%), which was expected, and do not seem to accurately represent the ratio of dose to water in the region. Lateral electronic equilibrium does not exist in these regions, so the introduction of transverse magnetic fields (those which guide electrons across the active volume asymmetrically at either edge of the beam) drastically alters the dose deposited in the detector, as well as in the phantom generally. At the left edge of the beam, electrons that would have reached the scoring volume tend to curve towards the central axis, and are not replaced, leading to lost dose contributions and a lower magnetic field dose response in the water and detector. It is clear from figure 4.17 that the amount by which the dose to water is altered by

the magnetic field at the left edge is not modelled accurately by the detector, differing by ~7%. At the right edge of the beam electrons tend to curve towards the scoring volume. As per previous discussion, these electrons see an increasing cross section of the active volume, leading to an increased dose response in the detector. The dose to water also increases in this case due to electrons curving towards the scoring volume. However, the increase to dose in water is again not accurately modelled by the detector, their responses in fact differ. The left and right edge responses of the water and diamond detector suggest that a combination of dose to water and intrinsic detector response are factors in the overall detector dose response at these positions. The beam periphery cases also differ from the in air simulations, which were done in the centre of a field encompassing the entire detector. The difference was expected, and arises because in this water tank case there is no electronic equilibrium.

Those water tank simulations completed in orientations III and IV using the diamond detector show similar results to the corresponding in air simulations, as was the case in orientations I and II-2 when not at the edge of the beam. However, at the periphery of the beam in orientation IV we do not see the large deviations in dose response that we saw in orientation II-2. The dose response instead is relatively stable. This was again expected, given that the electrons are focused downstream homogeneously throughout the beam, which would tend to lead to a stable response across the beam. The detector does seem to under-report the dose to water at the periphery slightly in orientation IV, but the water tank simulation uncertainty is still larger than the difference between simulations, so exact conclusions are impossible.

The water tank and in air simulations for the diode detector (figure 4.18) appear to lay nearly on top of one another when not at the edge of the beam for all orientations (beam edge simulations only completed in orientations II-2 and IV), differing by an average of 0.75%. This differs from the diamond

detector results, in that the simulation results in the water tank are closer to the corresponding simulation results in air. However, it must be noted that the water tank simulation error is still larger than the average difference between simulations. The dose response to water differs from that of the diode detector in the water tank, similarly to the diamond detector, as was expected. In the same manner as the diamond detector, the dose response of the diamond detector for a given orientation at the water tank field strength (0.5 T) is represented by the difference between the normalized dose to the detector, and the normalized dose to water at this point. Again, similar to the case for the diamond detector, the diode detector simulation results at the periphery of the beam for transverse magnetic fields in the water tank vary from the in air simulations a great deal (~10-20%), and vary from the dose to water simulations, but to a lesser extent (~10-14%). At the left edge of the beam, as was the case with the diamond detector, electrons tend to curve towards the central axis of the beam, and are not replaced, leading to the large decrease in dose response seen in the diode detector, as well as in the dose to water (but by different amounts). In contrast, at the right edge of the beam, there is a large increase in dose response. In the diode detector this is again mainly to the increasing cross section of the active volume seen by the incident electrons, where the difference in the dose to water is due to the increased number of electrons directed towards the scoring volume by the magnetic field. These results again differ from the in air simulations, where electron equilibrium existed. It is clear that the diode detector (in orientation II-2) does not accurately measure dose in the penumbra regions presented, the observed response is some combination of the actual change in dose to water with magnetic field, and the intrinsic response of the diode detector to the magnetic field.

The diode detector simulations completed in orientations III and IV show the same relative response (to the in air simulations) as those simulations completed in orientations I and II-2 when not at the periphery of the beam. The large deviations at the periphery of the beam seen in orientation II-2

are not seen in orientation IV, where instead the dose response is relatively stable through all detector locations. This is again due to the nature of the focused electrons downstream. The electrons in this case are focused symmetrically throughout the entire beam (including the beam edges), and are not preferentially curved in one direction. It is therefore not unexpected that we see the same dose response throughout all areas of the beam. However, we again see that the detector does seem to under-report the dose to water at the periphery slightly in orientation IV. Exact conclusions are still impossible here due to the size of the simulation uncertainty in this case.

### **4.3.2 CC13 Detector**

Figure 4.19 presents the CC13 water phantom simulation results. Displayed are the results whilst the chamber is positioned at each of the points described in section 3.2; additionally, the dose to water in the absence of the chamber at the beam edges in the direction of electron travel are also displayed. The average simulation uncertainty for the dose response for the CC13 is 4.0%, and the uncertainty in the dose to water at the periphery is 6.0%.

The ratio of dose with to that without magnetic field for the CC13 lingers around 1.0, or no magnetic field response, for all locations and orientations, provided the chamber is not at the periphery of the beam in the direction (or opposite direction) of electron travel. The direction of electron travel is henceforth defined as the direction an electron initially travelling in the beam's direction would tend to bend towards under the influence of the magnetic field. The influence of the electron path length and electron number that drove the dose response in the cylindrical ionisation chambers appears to have little effect on the CC13. This was expected, as the CC13 is nearly spherical, and thus changes in electron trajectory will alter the total

path length within the CC13 very little, and electron number should remain nearly constant due to the symmetry of the detector.

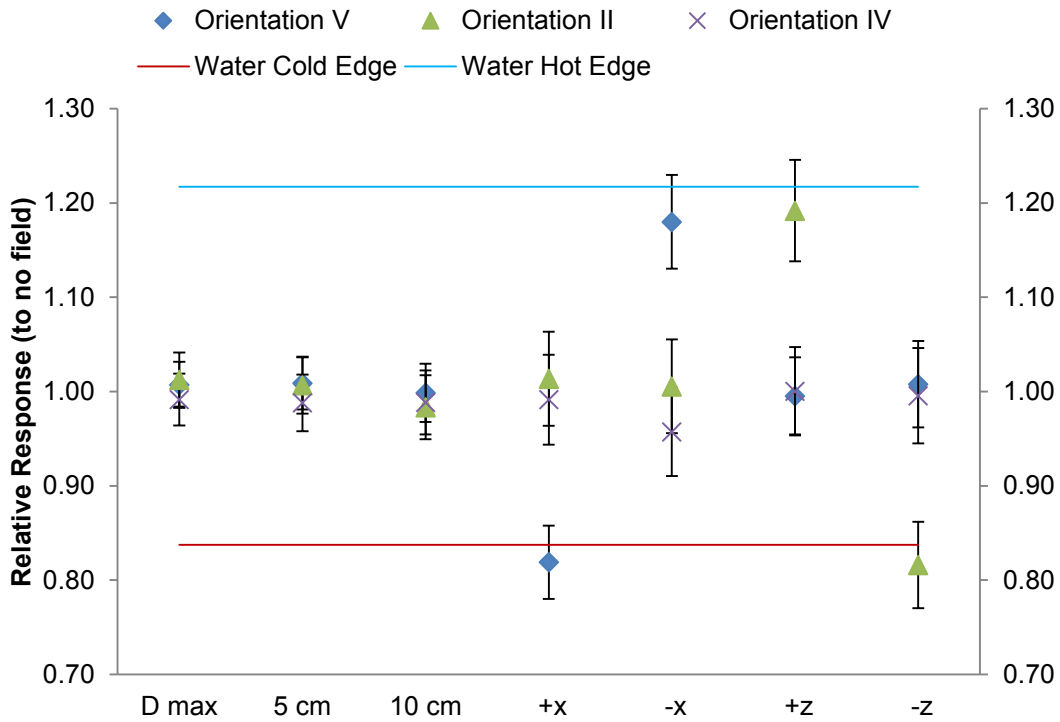


Figure 4.19 CC13 simulations in a water tank presented as the ratio of dose with to dose without magnetic field (0.5T). Water tank simulations are done at various depths in the phantom, and at the beam peripheries at 10cm depth. The ratio of dose to water, i.e. in the absence of the detector, at the periphery in the direction of electron travel also presented.

As per prior discussion, the dose to water in the central region of the beam will not change with application of a magnetic field<sup>6-12</sup>; this is due to continued electronic equilibrium in all directions. It is thus clear that the CC13, which has a response of near 1.0 in these regions, appears to accurately measure the dose deposition in these central regions of the beam. The response of the CC13 chamber at the periphery of the beam when not in the direction (or the opposed direction) of electron travel is again near 1.0. The dose to water at these points does not change with magnetic field strength, as the electronic equilibrium in this lateral direction is not altered by the magnetic field<sup>7-11</sup>. Therefore, it is clear that the CC13 appears to accurately measure the dose in this region as well. Finally, in the lateral penumbra positions in the primary and opposed directions of electron travel

the dose to water is increased and decreased respectively, as seen in figure 4.15. Also of note is that the response of the CC13 matches this increase and decrease; it is therefore natural to conclude that the CC13 chamber accurately models the dose deposition in these locations as well. In fact, the CC13 appears to model the dose deposition at all points within the phantom correctly.

#### **4.4 OSL Measurements**

Figure 4.20 depicts the magnetic field dose response of the Nanodot OSL devices. The transverse field cases are separated into without, and with the 2 cm of backscatter bolus, labelled “Transverse”, and “Transverse w/ backscatter” respectively. The average error in the ratio in transverse magnetic fields is ~7%, where the average error of the dose ratio in longitudinal magnetic fields is ~15%. The larger error in the longitudinal field case is due to the inverse square effect of the measurement setup on the dose deposited in each OSL. The large error in general is due to the variation in the individual OSL readings themselves. The same OSL, when read twice consecutively were found to have readings which can vary as much as 10 cGY. The average errors in dose deposited for each field strength are added in quadrature to the error in the zero field case obtaining the error in the ratio.

The average values of the OSL readings appear to have little to no response to the applied magnetic field in the longitudinal field and transverse field with backscatter cases. We would expect a small increase in dose response as a function of magnetic field strength for the case of transverse magnetic field case without backscatter, where the electron return effect will increase dose in this region with as magnetic field strength is increased. There is a small increase in dose observed with increasing magnetic field strength in

this case; however, at these magnetic field strengths this effect is small<sup>11</sup>, and is overwhelmed by the error in the associated measurements.

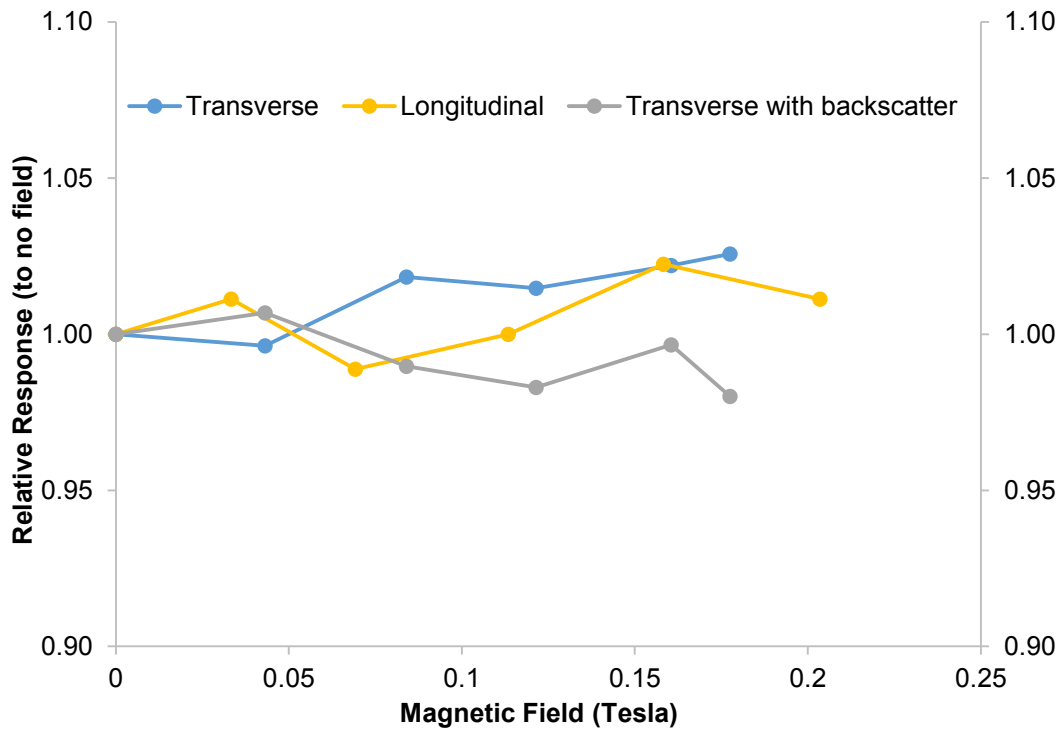


Figure 4.20 Relative dose response of Nanodot OSLs in transverse (without and with backscatter bolus) and longitudinal magnetic fields as a function of magnetic field strength.

## 4.5 References

- 1 I. Meijnsing, B.W. Raaymakers, A.J.E. Raaijmakers, J.G.M. Kok, L. Hogeweg, B. Liu, and J.J.W. Lagendijk, "Dosimetry for the MRI accelerator: the impact of a magnetic field on the response of a Farmer NE2571 ionization chamber.," *Phys. Med. Biol.* **54**(10), 2993–3002 (2009).
- 2 P.R. Almond, P.J. Biggs, B.M. Coursey, W.F. Hanson, M.S. Huq, R. Nath, and D.W. Rogers, "AAPM's TG-51 protocol for clinical reference dosimetry of high-energy photon and electron beams.," *Med. Phys.* **26**(9), 1847–70 (1999).
- 3 B.R. Muir and D.W.O. Rogers, "Monte Carlo calculations of  $k_{[sub Q]}$ , the beam quality conversion factor," *Med. Phys.* **37**(11), 5939–5950 (2010).
- 4 D. Sheikh-Bagheri and D.W.O. Rogers, "Monte Carlo calculation of nine megavoltage photon beam spectra using the BEAM code," *Med. Phys.* **29**(3), 391–402 (2002).
- 5 M.S. Weinhaus and J. a Meli, *Determining Pion, the correction factor for recombination losses in an ionization chamber.*, *Med. Phys.* **11**(6), 846–9 (1984).
- 6 A. Bielajew, "The effect of strong longitudinal magnetic fields on dose deposition from electron and photon beams," *Med. Phys.* **20**(4), 1171–1179 (1993).
- 7 A.J.E. Raaijmakers, MR-guided radiotherapy : magnetic field dose effects (Ph.D. Thesis, Utrecht University, 2008).
- 8 A.J.E. Raaijmakers, B.W. Raaymakers, and J.J.W. Lagendijk, "Integrating a MRI scanner with a 6 MV radiotherapy accelerator: dose increase at tissue-air interfaces in a lateral magnetic field due to returning electrons.," *Phys. Med. Biol.* **50**(7), 1363–76 (2005).
- 9 B.W. Raaymakers, A.J.E. Raaijmakers, a N.T.J. Kotte, D. Jette, and J.J.W. Lagendijk, "Integrating a MRI scanner with a 6 MV radiotherapy accelerator: dose deposition in a transverse magnetic field," *Phys. Med. Biol.* **49**(17), 4109–4118 (2004).
- 10 C. Kirkby, T. Stanescu, S. Rathee, M. Carlone, B. Murray, and B.G. Fallone, "Patient dosimetry for hybrid MRI-radiotherapy systems," *Med. Phys.* **35**(3), 1019–1027 (2008).

- 11 A.J.E. Raaijmakers, B.W. Raaymakers, and J.J.W. Legendijk, "Magnetic-field-induced dose effects in MR-guided radiotherapy systems: dependence on the magnetic field strength.," *Phys. Med. Biol.* **53**(4), 909–23 (2008).
- 12 C. Kirkby, B. Murray, S. Rathee, and B.G. Fallone, "Lung dosimetry in a linac-MRI radiotherapy unit with a longitudinal magnetic field," *Med. Phys.* **37**(9), 4722–4732 (2010).

# Chapter 5: Conclusion

## 5.1 Overview

In the previous chapters we have investigated the mechanics of cancer, and its impact on both individual persons and society as a whole; which commenced the discussion on radiotherapy, a common method of treatment of various cancers in Canada. Further, we laid forth a cohesive argument for the advancement of radiotherapy through the unification of a medical linear accelerator and an MR imaging device, known as the Linac-MR. Thereupon we were led to consider the need for an investigation into the behaviour of radiation detection devices which would operate within the magnetic field of the MR imaging device; specifically, the investigation of magnetic field corrections for radiation detectors as a function of magnetic field strength, and the relative orientations of the radiation detector, magnetic field, and incident photon beam.

In preparation for the detailed formulation of this study, and its eventual analysis, a brief digression to the theory necessary for the formulation and analysis was explored. The framework of charged particle transport in electromagnetic fields was presented, and an application – the measurement of a magnetic field – of this charged particle behaviour was introduced. Additionally, the details of radiation transport, and the dominant interactions in matter, were also introduced. The Monte Carlo simulation of radiation within EM fields using the PENELOPE code system was then surveyed, using the frameworks of EM fields and radiation transport introduced prior. Finally, the mechanics of detection of the radiation using the various detectors of interest was clarified for the reader.

Ultimately the procedure for measurement and simulation of the dose response of radiation detectors postulated previously was outlined. The

geometries of each of the detectors in air – including the hypothetical PTW60003 and IBA PFD detectors under material changes – and those simulated within a tank of water were detailed. Additionally, a select few parameters affecting dose measurements, namely relative field sizes,  $P_{pol}$ , and  $P_{ion}$ , were investigated for possible influences on the relative dose responses of ionisation chambers. The dose response as a function of magnetic field strength for the various pertinent orientations was presented graphically for all detectors and detection geometries investigated (in air, in water). Additionally, results of the relative field size,  $P_{pol}$ , and  $P_{ion}$  measurements were tabulated as a function of magnetic field strength.

Generally, the mechanisms of dose response are well understood, and can be applied to the detectors investigated. For all detectors investigated, in all scenarios, a dose response as a function of magnetic field strength with strong dependence on the relative orientations of the magnetic field, radiation beam, and the detector was found for transverse magnetic fields. At the same time, longitudinal magnetic fields exhibited very little dose response, notably none below 1.0T, regardless of configuration.

## **5.2 Ionisation Chambers**

Ionisation chamber measurements within the magnetic field of a hybrid Linac-MR have been found to require a multiplicative correction factor akin to  $P_{pol}$ ,  $P_{ion}$  etc. to relate the chamber reading to a dose deposited. This correction factor is the reciprocal of the chamber response (i.e. 0.935 for a response of 1.07), and is functionally dependent on the exact ionisation chamber used, the magnetic field strength, and the relative orientations of the magnetic field, radiation beam, and the ionisation chamber itself. The experimentally measured values in both transverse and longitudinal magnetic fields for the relevant chambers matched the simulated values closely, aiding confidence of the accuracy of the simulation results. These

measurements and simulation results are similar from chamber to chamber owing to the similarities in physical design of the detectors. The relative field size,  $P_{pol}$ , and  $P_{ion}$  measurements all confirm that at the field strengths investigated, none of these factors have any appreciable effect on the dose response of the PR06C (and presumably the NE2571 and A12) ionisation chamber.

Transverse field orientations (Figure 3.1 I, 3.1 II) exhibit identical behaviour to the previous independent study<sup>1</sup>, that being a shallow “U” trend as a function of magnetic field strength, with concavity determined by the orientation. This behaviour is resultant from the electron path and electron number within the active volume of the ionisation chamber, and can result in significant (8%) dose responses. Longitudinal orientations (Figure 3.1 III, 3.1 IV) show very little response as a function of magnetic field. A correction factor was found to not be required for field strengths less than 1.0 T in the presence of a longitudinal magnetic field, regardless of ion chamber orientation. This is in contrast to the transverse field geometries, where a correction factor is required, and is dependent on magnetic field strength and chamber orientation.

### **5.3 Solid State Detectors**

In air simulations of the PTW60003 diamond detector and IBA PFD diode detector suggest that measurements made with these detectors also require a multiplicative correction factor when a magnetic field is introduced. This correction factor, like that postulated for ion chambers, is the reciprocal of the dose response (i.e. 0.935 for a response of 1.07). The correction factor itself has a strong dependence on the relative orientations of magnetic field, detector long axis, and incident photon beam, and is highly dependent on the type of detector used. It is evident that any detector used will have to be characterized independently for its individual magnetic field

dose response. Unsurprisingly, the air gap in the PTW60003 and the tungsten shield in the IBA PFD appear to be driving factors in the dose response of their respective detectors.

Measurements made with the PTW60003 and IBA PFD in low field transverse magnetic fields follow the same trends as simulation data, generally agree quite closely, and are within simulation uncertainty. Measurements made at low field longitudinal magnetic fields with the PTW60003, and IBA PFD all vary very little with magnetic field strength up to the maximum field strength obtainable of about 0.21 T. These measurements are in the near vicinity of the simulation results at these field strengths. This closeness of measurement and simulation would tend to confirm of the accuracy of the simulation results at higher field strengths.

As was the case for ionisation chambers, transverse magnetic field orientations have the largest dose responses, and the longitudinal magnetic field orientations show little, if any response as a function of field strength. In fact, in the presence of a longitudinal magnetic field, minimal correction is needed at 1.5 T, and no correction is required below a field strength of 1.0 T for both detectors investigated. This is in contrast to the cases with transverse magnetic fields, where complete characterization of detectors on an individual basis is required as a function of relative orientations and field strengths.

## **5.4 Water Tank Simulations**

The water tank simulations suggest that in air characterization of the solid state detectors investigated (PTW60003, IBA PFD) gives a general trend of dose response with magnetic field. The accuracy of the in-air results compared to the water tank results appears to differ between detectors, but is within simulation statistical uncertainties in both cases; however, the diode detector displays a closer match between the in air simulations and

water tank simulations. It is once again shown that each of these solid state detectors must be investigated individually in the field geometry of interest before use. In the penumbra region of the photon beam, both detectors failed to accurately measure the change in dose to water when in the presence of transverse magnetic fields. Thus, in the presence of transverse magnetic fields, beam scanning measurements made with the PTW60003 or IBA PFD must consequently be taken with care, so that the beam profile at the beam periphery is measured without artefacts introduced by the detector itself. Longitudinal magnetic field geometries appear not to suffer from this issue to the same degree, if at all; it is thus easier, and therefore more desirable, to scan the photon beams in the presence of longitudinal magnetic field with these detectors.

Contrastingly, the CC13 ionisation chamber exhibited ideal behaviour in all positions within the water tank, in all simulated orientations. The simulated response in all orientations when not at the periphery of the beam was indistinguishable from 1.0 within simulation uncertainty. While the peripheral regions exhibited dose responses that matched the actual change in dose to water at those locations. Resultantly, in magnetic fields of 0.5 T, it appears that the CC13 ionisation chamber can be used as is, without regard for exact positioning with respect to the magnetic field and photon beam directions, as no correction factor for the addition of a magnetic field is required. This ideal behaviour in a magnetic field is due to the small, nearly spherical design of the CC13 ionisation chamber; where alterations in charged particle trajectories do not significantly alter the average electron path length and electron number driving the dose response for the cylindrical ionisation chambers.

## **5.5 OSL Detectors**

The Landauer Nanodot OSL detectors exhibit a large standard deviation intrinsic to the detectors themselves; this intrinsic error is exacerbated when the ratio of two individual readings is taken. While an average of readings can be obtained for an estimate of dose received, exact radiation measure is best left to other detectors. Further, within the (large) error of the relative OSL measurements, there appears to be no significant magnetic field effect on dose in any orientation at the field strengths investigated; though this does not preclude the requirement for a dose correction factor at higher magnetic fields, as one would expect in the transverse magnetic field case without backscatter due to returning electrons. Again, it must be noted that even at higher field strengths, any dose response would likely be simply overwhelmed by the innate error in relative measurements with these detectors.

## **5.6 Future Work**

Overall this work represents significant progress towards the formulation of a correction factor to the TG-51 protocol for use in the newly developed Linac-MR prototypes worldwide, nevertheless work in this area of study persists. The mechanisms of dose response of various radiation detectors as a function of magnetic field strength have been studied in varying relative orientations of photon beam, magnetic field, and detector long axis. This information could be used to guide the design of an ideal detector for use in the Linac-MR. This ideal detector would have no magnetic field dose response, regardless of orientation of magnetic field strength in a given hybrid Linac-MR system.

Additional detectors could always be investigated varying the above parameters, though their responses should be easily predicted from the

information contained in the previous chapters. A more pertinent investigation would be that into dose response changes as a function of angular variations in the detector long axis with respect to the photon beam differing from 0 or 90 degrees. These oblique angles, could provide insight into possible positioning errors on a detector to detector basis. These positioning errors, especially on the order of a few degrees, are expected to be likely in measurements.

Further, dependencies of the dose response on photon beam energy could also be investigated. This will be of the utmost importance when the dominant mechanism of photon beam interaction is no longer Compton scattering. Finally, all the water tank simulations were done in a static environment, thus there was no induced current in the detector cable due to motion through a magnetic field. Faraday's law could be investigated in beam scanning situations as the detector and cable traverse the magnetic field at differing rates.

## 5.7 References

- <sup>1</sup> I. Meijsing, B.W. Raaymakers, A.J.E. Raaijmakers, J.G.M. Kok, L. Hogeweg, B. Liu, and J.J.W. Lagendijk, "Dosimetry for the MRI accelerator: the impact of a magnetic field on the response of a Farmer NE2571 ionization chamber.," *Phys. Med. Biol.* **54**(10), 2993–3002 (2009).

# Bibliography

1. Canadian Cancer Society, *Cancer Information*, [www.cancer.ca](http://www.cancer.ca) (2014).
2. R.A. Weinberg, *The Biology of Cancer*, 2 Edition (Garland Science, New York, NY, 2013).
3. W.M. Becker, L.J. Kleinsmith, and J. Hardin, *The World of the Cell*, 5 Edition (Benjamin Cummings, San Francisco, CA, 2003).
4. N.A. Campbell and J.B. Reece, *Biology*, 6 Edition (Benjamin Cummings, San Francisco, CA, 2002).
5. Canadian Cancer Society and Stats Canada, *Canadian Cancer Statistics 2013* (Toronto, ON, 2013).
6. H.E. Johns and J.R. Cunningham, *The Physics of Radiology* (Charles C Thomas, Springfield, Illinois, 1983).
7. J. Van Dyk, *The Modern Technology of Radiation Oncology* (Medical Physics Publishing, Wisconsin, 2005).
8. F. Attix, *Introduction to Radiological Physics and Radiation Dosimetry* (WILEY-VCH, Weinheim, 2004).
9. D. Sheikh-Bagheri and D.W.O. Rogers, "Monte Carlo calculation of nine megavoltage photon beam spectra using the BEAM code," *Med. Phys.* **29**(3), 391–402 (2002).

10. ICRU, *ICRU Report 50: Prescribing, Recording, and Reporting Photon Beam Therapy* (1993).
11. ICRU, *ICRU Report 62: Prescribing, Recording and Reporting Photon Beam Therapy (Supplement to ICRU Report 50)* (1999).
12. J. Bernier, E.J. Hall, and A. Giaccia, "Radiation oncology: a century of achievements.," *Nat. Rev. Cancer* **4**(9), 737–47 (2004).
13. C.X. Yu, C.J. Amies, and M. Svatos, "Planning and delivery of intensity-modulated radiation therapy," *Med. Phys.* **35**(12), 5233 (2008).
14. T.R. Mackie, "History of tomotherapy," *Phys. Med. Biol.* **51**(13), R427–53 (2006).
15. K.M. Langen and D.T. Jones, "Organ motion and its management.," *Int. J. Radiat. Oncol. Biol. Phys.* **50**(1), 265–78 (2001).
16. P. Giraud and R. Garcia, "Respiratory gating for radiotherapy: main technical aspects and clinical benefits," *Bull. Cancer* **97**(7), 847–56 (2010).
17. X.A. Li, *Adaptive radiation therapy* (CRC Press, Boca Raton, Fla, 2011).
18. D. Verellen, M. De Ridder, N. Linthout, K. Tournel, G. Soete, and G. Storme, "Innovations in image-guided radiotherapy.," *Nat. Rev. Cancer* **7**(12), 949–60 (2007).
19. L.A. Dawson and D.A. Jaffray, "Advances in image-guided radiation therapy," *J. Clin. Oncol.* **25**(8), 938–946 (2007).

20. D.A. Jaffray, "Image-guided radiotherapy: from current concept to future perspectives," *Nat. Rev. Clin. Oncol.* **9**(12), 688–699 (2012).
21. J. Stroom and B. Heijmen, "Geometrical uncertainties, radiotherapy planning margins, and the ICRU-62 report," *Radiother. Oncol.* **64**, 75–83 (2002).
22. H. Meertens, M. Van Herk, J. Bijhold, and H. Bartelink, "First clinical experience with a newly developed electronic portal imaging device," *Phys. Med. Biol.* **18**(November 1989), 1173–1181 (1990).
23. J. Leong, "Use of digital fluoroscopy as an on-line verification device in radiation therapy.," *Phys. Med. Biol.* **31**(9), 985–92 (1986).
24. V.N. Hansen, "The application of transit dosimetry to precision radiotherapy," *Med. Phys.* **23**(5), 713 (1996).
25. K.L. Pasma, B.J.M. Heijmen, M. Kroonwijk, and a. G. Visser, "Portal dose image (PDI) prediction for dosimetric treatment verification in radiotherapy. I. An algorithm for open beams," *Med. Phys.* **25**(6), 830 (1998).
26. J. Pouliot, A. Bani-Hashemi, M. Svatos, F. Ghelmansarai, M. Mitschke, M. Aubin, P. Xia, O. Morin, K. Bucci, M. Roach, P. Hernandez, Z. Zheng, D. Hristov, and L. Verhey, "Low-dose megavoltage cone-beam CT for radiation therapy," *Int. J. Radiat. Oncol. Biol. Phys.* **61**(2), 552–560 (2005).

27. O. Morin, A. Gillis, J. Chen, M. Aubin, M.K. Bucci, M. Roach, and J. Pouliot, "Megavoltage cone-beam CT: system description and clinical applications," *Med. Dosim.* **31**(1), 51–61 (2006).
28. D.A. Jaffray, J.H. Siewerdsen, J.W. Wong, and A.A. Martinez, "Flat-panel cone-beam computed tomography for image-guided radiation therapy," **53**(5), 1337–1349 (2002).
29. D.A. Jaffray, D.G. Drake, M. Moreau, A.A. Martinez, and J.W. Wong, "A radiographic and tomographic imaging system integrated into a medical linear accelerator for localization of bone and soft-tissue targets," **45**(3), 773–789 (1999).
30. L. Santanam, K. Malinowski, J. Hubenshmidt, S. Dimmer, M.L. Mayse, J. Bradley, A. Chaudhari, K. Lechleiter, S.K.M. Goddu, J. Esthappan, S. Mutic, D. a Low, and P. Parikh, "Fiducial-based translational localization accuracy of electromagnetic tracking system and on-board kilovoltage imaging system.," *Int. J. Radiat. Oncol. Biol. Phys.* **70**(3), 892–9 (2008).
31. J.M. Balter, J.N. Wright, L.J. Newell, B. Friemel, S. Dimmer, Y. Cheng, J. Wong, E. Vertatschitsch, and T.P. Mate, "Accuracy of a wireless localization system for radiotherapy.," *Int. J. Radiat. Oncol. Biol. Phys.* **61**(3), 933–7 (2005).
32. D.W. Litzenberg, I. Gallagher, K.J. Masi, C. Lee, J.I. Prisciandaro, D. a Hamstra, T. Ritter, and K.L. Lam, "A measurement technique to determine the calibration accuracy of an electromagnetic tracking system to radiation isocenter.," *Med. Phys.* **40**(8), 081711 (2013).

33. C.S. Price and L.A. Savitz, *Improving Measurement of Surgical Site Infection Risk Stratification / Outcome Detection. Final Report* (Rockville, MD, 2012).
34. J.F. Dempsey, D. Benoit, J.R. Fitzsimmons, A. Haghigat, J.G. Li, D.A. Low, S. Mutic, J.R. Palta, H.E. Romeijn, and G.E. Sjoden, "A device for real time 3D image-guided IMRT," *Int. J. Radiat. Oncol. Biol. Phys.* **63**, S202–S202 (2005).
35. J. Dempsey, B. Dionne, J. Fitzsimmons, A. Haghigat, J. Li, D. Low, S. Mutic, J. Palta, H. Romeijn, and G. Sjoden, "A real-time MRI guided external beam radiotherapy delivery system," *Med. Phys.* **33**(6), 2254 (2006).
36. B.G. Fallone, M. Carlone, B. Murray, S. Rathee, T. Stanescu, S. Steciw, K. Wachowicz, and C. Kirkby, "Development of a Linac-MRI system for real-time ART," *Med. Phys.* **34**, 2547–2547 (2007).
37. B.G. Fallone, B. Murray, S. Rathee, T. Stanescu, S. Steciw, S. Vidakovic, E. Blosser, and D. Tymofichuk, "First MR images obtained during megavoltage photon irradiation from a prototype integrated linac-MR system," *Med. Phys.* **36**(6), 2084–2088 (2009).
38. B.W. Raaymakers, J.J.W. Lagendijk, J. Overweg, J.G.M. Kok, a J.E. Raaijmakers, E.M. Kerkhof, R.W. van der Put, I. Meijnsing, S.P.M. Crijns, F. Benedosso, M. van Vulpen, C.H.W. de Graaff, J. Allen, and K.J. Brown, "Integrating a 1.5 T MRI scanner with a 6 MV accelerator: proof of concept.," *Phys. Med. Biol.* **54**(12), N229–37 (2009).

39. J.J.W. Lagendijk, B.W. Raaymakers, A.J.E. Raaijmakers, J. Overweg, K.J. Brown, E.M. Kerkhof, R.W. van der Put, B. Hårdemark, M. van Vulpen, and U.A. van der Heide, "MRI/linac integration," *Radiother. Oncol.* **86**(1), 25–29 (2008).
40. J. Yun, E. Yip, K. Wachowicz, S. Rathee, M. Mackenzie, D. Robinson, and B.G. Fallone, "Evaluation of a lung tumor autocontouring algorithm for intrafractional tumor tracking using low-field MRI: a phantom study.," *Med. Phys.* **39**(3), 1481–94 (2012).
41. C. Kirkby, T. Stanescu, S. Rathee, M. Carlone, B. Murray, and B.G. Fallone, "Patient dosimetry for hybrid MRI-radiotherapy systems," *Med. Phys.* **35**(3), 1019–1027 (2008).
42. C. Kirkby, B. Murray, S. Rathee, and B.G. Fallone, "Lung dosimetry in a linac-MRI radiotherapy unit with a longitudinal magnetic field," *Med. Phys.* **37**(9), 4722–4732 (2010).
43. A.J.E. Raaijmakers, B.W. Raaymakers, and J.J.W. Lagendijk, "Magnetic-field-induced dose effects in MR-guided radiotherapy systems: dependence on the magnetic field strength.," *Phys. Med. Biol.* **53**(4), 909–23 (2008).
44. A.J.E. Raaijmakers, B.W. Raaymakers, and J.J.W. Lagendijk, "Experimental verification of magnetic field dose effects for the MRI-accelerator.," *Phys. Med. Biol.* **52**(14), 4283–91 (2007).
45. A.J.E. Raaijmakers, B.W. Raaymakers, and J.J.W. Lagendijk, "Integrating a MRI scanner with a 6 MV radiotherapy accelerator: dose increase at tissue-air interfaces in a lateral magnetic field due to returning electrons.," *Phys. Med. Biol.* **50**(7), 1363–76 (2005).

46. B.W. Raaymakers, A.J.E. Raaijmakers, a N.T.J. Kotte, D. Jette, and J.J.W. Lagendijk, "Integrating a MRI scanner with a 6 MV radiotherapy accelerator: dose deposition in a transverse magnetic field," *Phys. Med. Biol.* **49**(17), 4109–4118 (2004).
47. A.J.E. Raaijmakers, MR-guided radiotherapy : magnetic field dose effects (Ph.D. Thesis, Utrecht University, 2008).
48. A.J.E. Raaijmakers, B.W. Raaymakers, S. van der Meer, and J.J.W. Lagendijk, "Integrating a MRI scanner with a 6 MV radiotherapy accelerator: impact of the surface orientation on the entrance and exit dose due to the transverse magnetic field.," *Phys. Med. Biol.* **52**(4), 929–39 (2007).
49. A.J.E. Raaijmakers, B. Hårdemark, B.W. Raaymakers, C.P.J. Raaijmakers, and J.J.W. Lagendijk, "Dose optimization for the MRI-accelerator: IMRT in the presence of a magnetic field.," *Phys. Med. Biol.* **52**(23), 7045–54 (2007).
50. A. Bielajew, "The effect of strong longitudinal magnetic fields on dose deposition from electron and photon beams," *Med. Phys.* **20**(4), 1171–1179 (1993).
51. Y. Chen, A.F. Bielajew, D.W. Litzenberg, J.M. Moran, and F.D. Becchetti, "Magnetic confinement of electron and photon radiotherapy dose: A Monte Carlo simulation with a nonuniform longitudinal magnetic field," *Med. Phys.* **32**(12), 3810 (2005).

52. S.N. Rustgi and D.M.D. Frye, "Dosimetric characterization of radiosurgical beams with a diamond detector," *Med. Phys.* **22**(12), 2117–2121 (1995).
53. M. Bucciolini, F. Banci Buonamici, S. Mazzocchi, C. De Angelis, S. Onori, and G. a. P. Cirrone, "Diamond detector versus silicon diode and ion chamber in photon beams of different energy and field size," *Med. Phys.* **30**(8), 2149–2154 (2003).
54. P.R. Almond, P.J. Biggs, B.M. Coursey, W.F. Hanson, M.S. Huq, R. Nath, and D.W. Rogers, "AAPM's TG-51 protocol for clinical reference dosimetry of high-energy photon and electron beams.," *Med. Phys.* **26**(9), 1847–70 (1999).
55. M. Reynolds, B. Fallone, and S. Rathee, "Dose response of selected ion chambers in applied homogeneous transverse and longitudinal magnetic fields," *Med. Phys.* **40**(4), 042102 (2013).
56. M. Reynolds, B.G. Fallone, and S. Rathee, "Dose response of selected solid state detectors in applied homogeneous transverse and longitudinal magnetic fields," *Med. Phys.* **41**(9), 092103 (2014).
57. I. Meijsing, B.W. Raaymakers, A.J.E. Raaijmakers, J.G.M. Kok, L. Hogeweg, B. Liu, and J.J.W. Lagendijk, "Dosimetry for the MRI accelerator: the impact of a magnetic field on the response of a Farmer NE2571 ionization chamber.," *Phys. Med. Biol.* **54**(10), 2993–3002 (2009).
58. K. Smit, B. Asselen, J.G.M. Kok, J.J.W. Lagendijk, and B. Raaymakers, "Reference Dosimetry for An MRI-Linac The Magnetic Field," *Med. Phys.* **39**(6), 4010–4011 (2012).

59. B. Raaymakers, K. Smit, G.H. Bol, M.R. Van den Bosch, S.P.M. Crijs, J.G.M. Kok, and J.J.W. Lagendijk, "Dosimetry in Strong Magnetic Fields; Issues and Opportunities," *Radiother. Oncol.* **103**, S170 (2012).
60. S. Goddu, O. Pechenaya Green, and S. Mutic, "TG-51 Calibration of First Commercial MRI-Guided IMRT System in the Presence of 0.35 Tesla Magnetic Field," *Med. Phys.* **39**, 3968 (2012).
61. M. McEwen, L. DeWerd, G. Ibbott, D. Followill, D.W.O. Rogers, S. Seltzer, and J. Seuntjens, "Addendum to the AAPM's TG-51 protocol for clinical reference dosimetry of high-energy photon beams.," *Med. Phys.* **41**(4), 041501 (2014).
62. J. Baro, J. Sempau, J.M. Fernández-Varea, and F. Salvat, "PENELOPE: an algorithm for Monte Carlo simulation of the penetration and energy loss of electrons and positrons in matter," *Nucl. Instruments Methods Phys. Res. (100)*, 31–46 (1995).
63. J. Sempau, J.M. Fernández-Varea, E. Acosta, and F. Salvat, "Experimental benchmarks of the Monte Carlo code penelope," *Nucl. Instruments Methods Phys. Res. Sect. B Beam Interact. with Mater. Atoms* **207**(2), 107–123 (2003).
64. F. Salvat, J.M. Fernandez-Varea, and J. Sempau, *PENELOPE: A code system for Monte Carlo simulation of electron and photon transport* (2006).
65. D.J. Griffiths, *Introduction to Electrodynamics*, 3 Edition (Prentice Hall, Upper Saddle River, NJ, 1999).

66. J.D. Jackson, *Classical Electrodynamics*, 3 Edition (Wiley, New York, NY, 1999).
67. E.H. Hall, "On a new action of the magnet on electric currents," *Am. J. Math.* **2**(3), 287–292 (1879).
68. C.M. Hurd, *The Hall Effect in Metals and Alloys* (Plenum Press, New York, NY, 1972).
69. P.A. Tipler and R.A. Llewellyn, *Modern Physics*, 4 Edition (W.H. Freeman and Company, New York, NY, 2003).
70. S.M. Ross, *Introduction to Probability Models*, 9 Edition (Elsevier, San Diego, CA, 2007).
71. K. Yosida, *Functional Analysis* (Springer-Verlag, 1968).
72. J. Baro, J. Sempau, J.M. Fernandez-Varea, and F. Salvat, "Simplified Monte Carlo simulation of elastic electron scattering in limited media," *Nucl. Instruments Methods Phys. Res. Sect. B Beam Interact. with Mater. Atoms* **84**, 465–483 (1994).
73. I. Kawrakow and A.F. Bielajew, "On the representation of electron multiple elastic-scattering distributions for Monte Carlo calculations," *Nucl. Instruments Methods Phys. Res. Sect. B Beam Interact. with Mater. Atoms* **134**(3-4), 325–336 (1998).
74. J.M. Fernández-Varea, R. Mayol, J. Baro, and F. Salvat, "On the theory and simulation of multiple elastic scattering of electrons," *Nucl. Instruments Methods Phys. Res. Sect. B Beam Interact. with Mater. Atoms* **73**, 447–473 (1993).

75. D.J. La Russa and D.W.O. Rogers, "Accuracy of Spencer-Attix cavity theory and calculations of fluence correction factors for the air kerma formalism," *Med. Phys.* **36**(9), 4173 (2009).
76. K. Smit, B. van Asselen, J.G.M. Kok, a H.L. Aalbers, J.J.W. Legendijk, and B.W. Raaymakers, "Towards reference dosimetry for the MR-linac: magnetic field correction of the ionization chamber reading.," *Phys. Med. Biol.* **58**(17), 5945–57 (2013).
77. E. Barnett, *Diamond Detector for IMRT Dosimetry* (University of Alberta, 2004).
78. G. Shani, *Radiation Dosimetry Instrumentation and Methods*, 2 Edition (CRC Press, 2000).
79. L. Bøtter-Jensen, S.W.S. McKeever, and A.G. Wintle, *Optically Stimulated Luminescence Dosimetry* (Elsevier, Amsterdam, 2003).
80. J. Sempau, E. Acosta, J. Baro, J.M. Fernández-Varea, and F. Salvat, "An algorithm for Monte Carlo simulation of coupled electron-photon transport," *Nucl. Instruments Methods Phys. Res. Sect. B Beam Interact. with Mater. Atoms* **132**(3), 377–390 (1997).
81. C. Kirkby, T. Stanescu, and B.G. Fallone, "Magnetic field effects on the energy deposition spectra of MV photon radiation.," *Phys. Med. Biol.* **54**(2), 243–57 (2009).
82. B.R. Muir and D.W.O. Rogers, "Monte Carlo calculations of  $k_{[sub Q]}$ , the beam quality conversion factor," *Med. Phys.* **37**(11), 5939–5950 (2010).

83. P.N. Mobit and G. a Sandison, "An EGS4 Monte Carlo examination of the response of a PTW-diamond radiation detector in megavoltage electron beams.," Med. Phys. **26**(5), 839–44 (1999).
84. K. Eklund and A. Ahnesjö, "Spectral perturbations from silicon diode detector encapsulation and shielding in photon fields," Med. Phys. **37**(11), 6055–6060 (2010).
85. L. Chen, R. Price, J. Li, L. Wang, L. Qin, and C. Ma, "Evaluation of MRI-based Treatment Planning for Prostate Cancer using the AcQPlan System," Med. Phys. **30**(6), 1507 (2003).
86. M.S. Weinhaus and J. a Meli, "Determining Pion, the correction factor for recombination losses in an ionization chamber", Med. Phys. **11**(6), 846–9 (1984).